1-1-2016

Novel Design And Synthesis Of Structured Iron Oxides For Battery Applications

Jian Zhu
Wayne State University,

NOVEL DESIGN AND SYNTHESIS OF STRUCTURED IRON OXIDES FOR BATTERY APPLICATIONS

by

JIAN ZHU

DISSERTATION

Submitted to the Graduate School

of Wayne State University,

Detroit, Michigan

in partial fulfillment of the requirements

for the degree of

DOCTOR OF PHILOSOPHY

2016

MAJOR: Chemical Engineering

Approved By:

Advisor	Date
Committee Member:	Date

DEDICATION

This dissertation is dedicated to my beloved parents Weiguo Zhu and Meixiang Zhu. Thank you for all of your love and support.

ACKNOWLEDGEMENTS

First and foremost, I sincerely thank my advisor, Dr. Da Deng, for his invaluable advice, constant guidance, timely support and continuous encouragement all these years. I have benefited enormously from his innovative research ideas across different disciplines and many in-depth discussions and brainstorms. He has not only shared with his scientific ideas and provided constructive and critical comments, but also he has taught me many soft skills including generating scientific ideas based on hypothesis, solving problems from different perspectives and writing papers logically. I would not have been able to finish this doctoral thesis without his close guidance. I appreciate the methodologies, stories and philosophies he has shared with me. His enthusiasm and dedication to research has partially inspired me to pursue a career in scientific research.

I would also like to acknowledge my committee members, Dr. Yong Xu, Dr. Guangzhao Mao, and Dr. Simon Ng for their insightful comments and suggestions on my dissertation. I gratefully appreciate their valuable time serving on my dissertation committee. I also appreciate the support I have received from the department, particularly Dr. Charles Manke, Dr. Guangzhao Mao and Dr. Simon Ng.

I would like to thank all my lab mates, particularly, Xinghua Meng, Sai Addu, Kevi Charles, Rakesh Probe and Minahi Aldossary for their help and friendship. I appreciate the supports from my colleagues in these years, namely: Dr. Zhi Mei at Lumigen Instrument Center; Christopher Mark Thrush, Sally Yurgelevic, Dr. Gregory Auner, Ehab Hamdy Abdelhamid, Dr. Gavin Lawes, Da Li, Dr. Stephanie Brock, Huali Wang, Lixin Wang, Rhet Guzman and Mahbuba Ara.

I would like to express my deepest gratitude to my parents and grandparents, for their endless and selfless love. I would not have a chance to pursue and complete my Ph.D without their support and encouragement.

Last but not least, I would like to thank all the nice persons who have helped me in one way or another during my Ph.D. candidacy.

TABLE OF CONTENTS

LIST OF TABLES

LIST OF FIGURES

CHAPTER 1. INTRODUCTION

1.1 Background

In the past two decades (1993-2013), the global energy consumption has been continuously increasing from 345 to 539 Quadrillion Btu. The total carbon dioxide emissions from the consumption for energy has increased from 21,438 to 33,010 Million Metric Tons. [US Energy Information Administration] In the U.S., 83% of the energy consumption is supplied by fossil fuels (petroleum (34%), natural gas (25%) and coal (20%)), only 8% and 10% are supplied by nuclear power and environmentally friendly renewable energy source (solar energy, wind power, biomass and biofuels, etc.), respectively in 2014. [http://www.eia.gov/countries/data.cfm, US Energy Information Administration] The energy consumption supplied by renewable energy has increased by 6.6% (0.6 quadrillion Btu) from 2011 to 2014, however this incensement of 0.6 quadrillion Btu is only 0.6% of the overall energy consumption. To meet the increasing demand for energy and to slow down the pace of CO_2 emission, it is very essential to further increase the proportion of energy supplied from environmentally friendly renewable energy sources such as solar energy, wind power, biomass and biofuels, etc. Energy storage is a critical component in the energy conversion-storage-delivery chain in sustainable energy. Therefore, the development of reliable energy storage systems with low-cost and environmentally benignity is in great needs. On the other hand, to alleviate the dependence on fossil fuels, and to reduce carbon dioxide emissions as well as toxic exhaust emissions from automobiles, electric drive vehicles including electric vehicles (EVs) and hybrid eclectic vehicles (HEVs) are viewed by the world with great promise in the 21st century, as transportation is the 2nd largest energy consumption sector. With the rapid progress in electric vehicles, there is a rapid increasing demand for high energy and power density of electrical energy storage devices. Therefore, it is very essential to the develop low-cost, stable and efficient

energy storage strategy (1) to balance the fluctuating energy generated from renewable resources (e.g., wind and solar), (2) to fulfill the demand for high energy/power density in electric drive vehicles, and (3) to reduce the reliance on conventional fossil fuels and make the future more sustainable.

1.2 Lithium ion batteries

Rechargeable electrochemical batteries are considered as one of the most successful technologies that can reversibly store electrical energy. Among various electrochemical energy storage technologies, lithium ion batteries (LIBs) have been considered as a promising technology for a wide variety of applications due to advantages of high voltage, long cycling life, low self-discharge, and high reliability.[1] It is now the dominant power source for portable electronic devices because of its high energy density, long lifespan and light weight and it is moving toward larger-scale applications such as electric vehicles or renewable energy storage. For example, Tesla has applied the lithium-ion battery technic in their electric vehicles like Model S or Model X, and also in their Powerwall product to sustainably store energy.

Table 1-1 Advantages and Disadvantages of Li-ion Batteries[2]

Advantages	**Disadvantages**
Sealed cells; no maintenance required Long cycle life Broad temperature range of operation Long shelf life Low self-discharge rate Rapid charge capability	Moderate initial cost Degrades at high temperature Need for protective circuitry Capacity loss and potential for thermal runaway when overcharged.

Advantages	**Disadvantages**
High-rate and high-power discharge capability High coulombic and energy efficiency High specific energy and energy density No memory effect Many possible chemistries offer design flexibility Can be made in aluminized plastic cases as "pouch" or polymer cells	Possible venting and possible thermal runaway when crushed May become unsafe if rapidly charged at low temperatures (< 0°C)

The major advantages and disadvantages of LIBs are listed in Table 1-1. The high specific energy (up to 240 Wh/kg) and energy density (up to 640 Wh/L) of commercial LIBs make them intriguing in marketplace mainly because the demand for high energy/power can be achieved with smaller and lighter batteries. Besides, LIBs have a very low self-discharge rate (2% to 8% per month), long cycle life (greater than 1000 cycles), and a broad temperature range of operation (commercially available cells may be charged at 0 to 45°C and discharged at −40 to 65°C), enabling their use in a wide variety of applications.

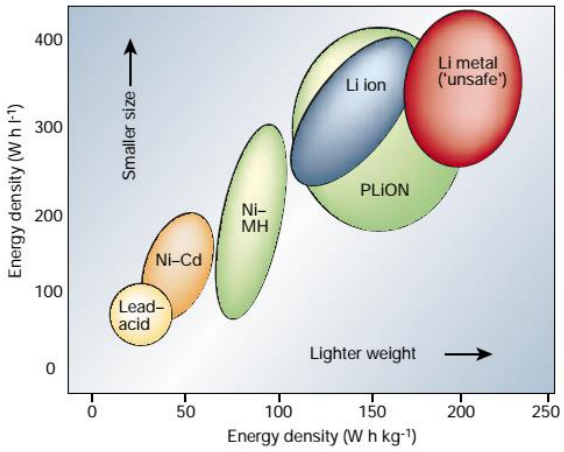

Fig. 1-1 Comparison of different battery technologies in terms of volumetric and gravimetric energy density. [3]

Table 1-2 General Secondary Battery Comparison for Consumer Application [2]

Characteristic	NiCd	NiMH	Lithium-Ion
Cell voltage	1.2	1.2	3.6-3.7
Cycle life at 80% DOD	1000+	500+	400-500
Temperature range	–40 to 70°C	–40 to 50°C	–20 to 60°C
Memory effect	Yes	Yes	No
High rate discharge	10C +	Up to 5C	Up to 2C (typical)
Fast charge time	<1 h	2 h	2 h
Capacity after 1 year storage @ 25°C	<30%	<20%	80%
Energy density @ 10 h discharge rate	60 Wh/kg	90 Wh/kg	230 Wh/kg

The comparison of different rechargeable battery technologies is shown in Fig. 1-1 and Table 1-2. As compared to lead-acid (Pb-acid) battery, nickel -cadmium (Ni-Cd) battery, and nickle-metal hydride (Ni-MH) battery, lithium ion battery shows much larger volumetric or gravimetric energy density (Fig. 1-1). The Pb–acid battery is the oldest type of rechargeable battery invented in 1859; Ni-Cd battery was invented in 1899 but was later superseded by NiMH batteries due to the toxicity of Cadmium. The share of worldwide sales for Ni–Cd, Ni–MeH and Li-ion portable batteries is 23%, 14% and 63%, respectively. The use of Pb–acid batteries is restricted mainly to SLI (starting, lighting, ignition) in automobiles or standby applications, whereas Ni–Cd batteries remain the most suitable technologies for high-power applications (for example, power tools).[3]

Also, in Table 1-2, LIB shows a much higher energy density than other batteries (~2 to 3 times higher than Ni-Cd or Ni-MH batteries). In addition, the high-voltage, the light weight and the design flexibility all make LIBs superior than other rechargeable battery systems in the market of portable devices.

1.3 Challenges

With rapid development in personal portable devices and electric vehicles, the demand of batteries with higher energy density, higher powder density and longer cycle life are also increasing rapidly. However, energy storage cannot keep pace with the rate of those progress. Taking electric vehicles as example, the status of lithium-ion battery technology in comparison to USABC minimum goals for commercialization for EV applications is presented by USABC in May 2009 (Fig. 1-2). As we can see from the figure, to meet the minimum goals for commercialization, the main challenges LIBs are facing to include the cost, safety, and energy density. There is urgent need to improve those properties in order to meet the minimum requirement to compete with conventional internal combustion engine vehicles. The power density and cyclic life only reached the minimum goals, the improvement of power density and cyclic life will still benefit the EV application.

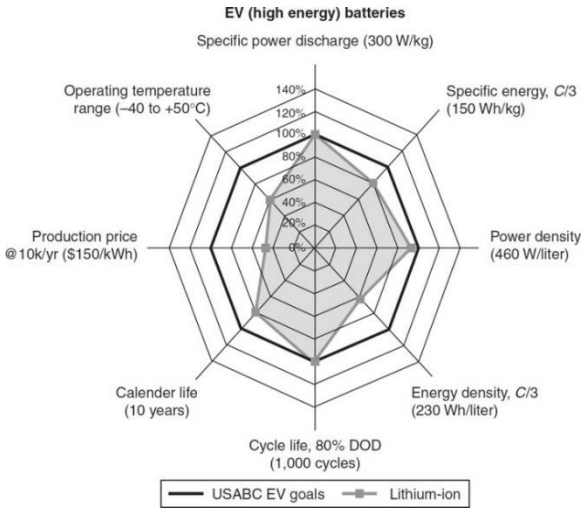

Fig.1-2 USABC goals for EVs application cannot fulfill by current state of the art battery technologies.[2]

1.4 Significance of the research

The improvement of LIBs is a multi-facetted problem, and can be achieved via the improvement of many key components in LIB system. Based on the electrochemical reaction and the battery structure, improvement can be achieved via three main components of the battery:

1. Two electrodes: Anode or cathode active materials, binder, electronic conducting additive on current collector

2. Electrolyte

3. Four interfaces: two solid/solid interfaces between electrode materials and current collector and two solid/liquid interfaces between electrode materials and liquid electrolyte

As an electrochemical energy storage system, the energy storage of LIB relies on the storage of electrons/ions in active materials (either cathode or anode). My research focuses on the study of anode active materials, aiming at improving LIB performance vis preparing nano-/micro-structured iron oxides based active materials. Nano- or Micro- structured iron oxides with various sizes/morphologies were prepared in order to study the effect of size/morphology on battery

performance, and to enhance the performance of LIBs by improving the performance of anode materials.

1.5 Outline of the thesis

In this thesis, the background, the concept, challenges of LIB and the key aspects from which we can further improve the electrochemical performance of LIB were introduced in Chapter 1.

The components and structure of Li-ion battery system, carbon alternative anode materials for Li-ion batteries, and the mechanism how active materials store Li-ion were introduced in Chapter 2. Convention-type 3d transitional metal oxides were compared and the literature for iron oxides materials with different sizes and morphologies were reviewed, which include 1-dimentional, 2-dimentional, 3-dimentional structures, microsized structure, and iron oxides/ carbon composites.

The detail of my research work begins from Chapter 3, the experimental section for materials preparation and characterization. Our work focuses on the micro-/nano-structured iron oxides materials as negative electrode materials for LIB applications. Both microstructured iron oxides materials and nanoparticle ensembles with unique morphologies have been prepared and their performance as anode materials for LIBs were reviewed. In detail, microstructures of iron oxide were discussed in Chapter 4, including (1) single crystalline α-Fe_2O_3 solid microparticles and (2) single crystalline α-Fe_2O_3 microframes; and nanoparticle ensembles were discussed in Chapter 5, including (3) hollow cocoon-like α-Fe_2O_3 nanoparticle ensembles, (4) α-Fe_2O_3 chevron microbeads with tunnel, and (5) olive-like porous nanosized α-Fe_2O_3/carbon materials and hollow Fe_3O_4/carbon composite. All as-prepared materials were fully characterized though various technics (FESEM, TEM, XRD, TGA, XPS, etc.); the experimental parameters were studied to control and to obtain the different sizes or morphologies of as-prepared materials; the formation mechanism of nano-/micro-structures were proposed based on a serious of experiments, and

electrochemical performance of those materials with various sizes/morphologies in LIBs have been studied.

CHAPTER 2. LITERATURE REVIEW

2.1 Li-ion battery system

LIBs were first commercialized by Sony Cooperation in June 1991 and are now the dominant power sources for portable electronic devices. This commercial LIB consists of three primary components: negative electrode (anode) based on graphitic carbon, positive electrode (cathode) based on layered oxide (e.g. $LiCoO_2$), polyanion (e.g. $LiFePO_4$) or spinel (e.g. $LiMn_2O_4$), and non-aqueous liquid electrolyte in between two electrodes, consists of lithium salts in a mixture of organic carbonates (e.g. $LiPF_6$ in the mixture of ethylene carbonate-diethylcabonate (EC-DEC)). LIBs have been referred to as rocking chair batteries because the lithium ions "rock" back and forth between the positive and negative electrodes as the cell is charged and discharged. As shown in Fig. 2-1,[4] during charging process, lithium ions in layered $LiCoO_2$ transfer to electrolyte, the lithium ions in electrolyte are intercalated into the anode materials. Meanwhile, the electrons flow from the positive electrode (cathode) to more negative potential (anode) from the external circuit. The processes are reversed in discharging process.

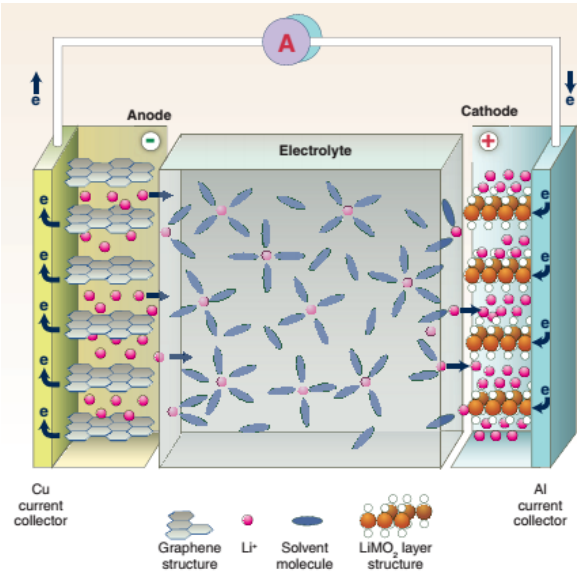

Fig. 2-1. Schematic of a LIB. The negative electrode is a graphitic carbon that holds Li in its layers, whereas the positive electrode is a Li-intercalation compound — usually an oxide because of its higher potential — that often is characterized by a layered structure. Both electrodes are able to reversibly insert and remove Li ions from their respective structures. On charging, Li ions are removed or de-intercalated from the layered oxide compound and intercalated into the graphite layers. The process is reversed on discharge. The electrodes are separated by a nonaqueous electrolyte that transports Li ions between the electrodes.[4]

LIBs are used in virtually all types of rechargeable portable electronic devices, such as laptops cellphones, and digital cameras. In recent decades, the application of LIBs was extended to electric drive vehicles (EVs , HEVs) and grid-energy storage, due to its good performance in terms of energy density, specific energy, specific power, cycle life, storage life.[2] However, the theoretical capacity is almost achieved using the current electrode materials. To overpass the bottleneck and achieve a higher capacity (or energy density) to meet the increasing demand for reliable energy storage devices, great effort has been made in recent years to improve the electrode materials to fulfill the growing demand on electrochemical energy storage, via the detail study on the chemistry, crystallography, size and morphology of the battery components.

2.2 Anode materials for LIBs and their challenges

To further improve the electrochemical performance for LIBs, the study of anode materials, cathode materials and electrolyte materials are of great importance. And our research focuses on anode materials. Fig. 2-2 shows various alternative materials for both graphite negative materials and $LiCoO_2$ positive materials. The theoretical capacity for commercial graphite negative material is 372 mA h g^{-1} only (corresponding to LiC_6). Composite alloys, carbon based materials, Sn-based materials and 3d-metal oxides materials have relatively higher specific capacities than graphite. Among those alternative negative materials, 3d-metal oxides have even higher theoretical capacities than others. 3d transition metal oxides materials have been considered as promising alternative anode materials for graphite anode materials because of their much higher theoretical

capacity based on different storage mechanism of either alloying/de-alloying reaction or conversion-type reaction. However, similar to Sn based materials, 3d- metal oxides materials suffer from severe volume expansion during the lithiation process, which will cause the fracture of original structure, the resulting bad electrical contact between particles, and poor cyclability. Those issues have to be addressed if those high-capacity anode materials are chosen to replace the graphite materials.

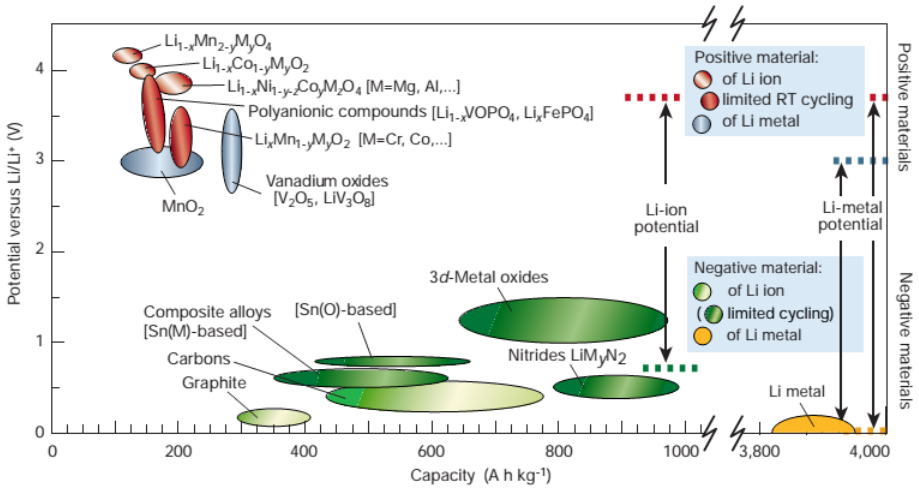

Fig. 2-2. Voltage versus capacity for positive- and negative-electrode materials presently used or under serious considerations for the next generation of rechargeable Li-based cells. The output voltage values for Li-ion cells or Li-metal cells are represented. Note the huge difference in capacity between Li metal and the other negative electrodes, which is the reason why there is still great interest in solving the problem of dendrite growth.[3]

The reaction mechanism of lithiation and de-lithiation on metal oxides materials can be classified into three main groups, (1) the insertion/extraction type, (2) the alloying type, and (3) the conversion type. The schematic illustration of three types of reaction is shown in Fig. 2-3.[5] The huge volume expansion during insertion of lithium ion was clearly shown in alloying-type and conversion- type materials. The electrochemical reactions of three types of reaction are listed.

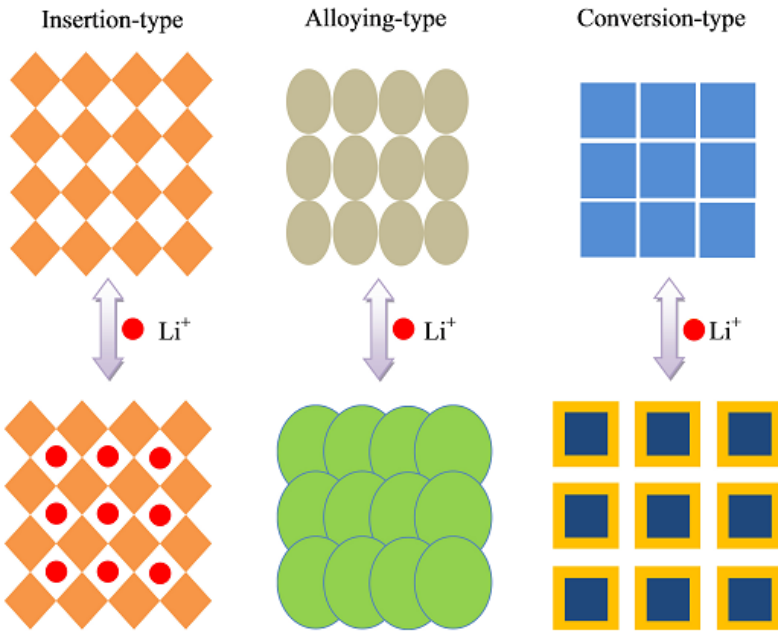

Fig. 2-3. Schematic illustration of different types of lithium-ion storage materials.[5]

(1) Insertion reaction mechanism:

$$MO_x + yLi^+ + ye^- \leftrightarrow Li_yMO_x \quad (1)$$

(2) Li-alloy reaction mechanism:

$$M_xO_y + 2yLi^+ + 2ye^- \rightarrow xM + yLi_2O \quad (2)$$

$$M + zLi^+ + ze^- \leftrightarrow Li_zM \quad (3)$$

(3) Conversion reaction mechanism:

$$M_xO_y + 2yLi^+ + 2ye^- \leftrightarrow xM + yLi_2O \quad (4)$$

Insertion reaction exists in most cathode materials and some anode materials, such as graphite V_2O_5 and TiO_2. All the materials in insertion type have limitations on their intrinsic capacities and the resulting energy densities.

Alloy reaction exists in some main-group elements, such as Si, Sn and Zn, which can alloy with lithium at a low potential. The volume changes of those materials are pretty huge during the lithiation/de-lithiation processes. Those huge volume changes can be accommodated through

alloying, protection by carbon coating layer or preparation of materials in nanoscale, which have more free space and can alleviate the stress between materials.

Most 3d-transition metal oxides (M_xO_y, M= Mn, Fe, Co, Ni, Cu) are in conversion type. Those materials have relatively high theoretical capacities for they can incorporate more than one Li per 3d metal. 0-valent metal and Li_2O will form through thorough lithiation process. However, this kind of materials also suffers from large volume expansion during the lithiation process, as well as poor conductivity caused by their intrinsic properties and the bad contacts caused by the volume change. (Table 2-1) Those issues can be addressed through preparation of (1) nanomaterials, (2) microstructures with unique morphology (such as hollow, core-shell, or porous structures, etc.), and (3) M_xO_y/carbon composites.

Table 2-1. Summarization of conversion reaction-based nanostructured transitional metal oxide anode[6]

Metal oxides		Theoretical capacities (mAh g^{-1})	Representive nanostructures	Common problems and possible solutions
Iron oxides	Fe_2O_3	1007[229,230]	Nanostructures and carbon-based nanocomposites[231–237]	Common problems: Low Coulombic efficiency at the first cycle, unstable SEI film formation, large potential hysteresis, and poor capacity retention.
	Fe_3O_4	926[231–238]		
Cobalt oxides	Co_3O_4	890[86]	Nanostructured Co_3O_4 or Co_3O_4/carbon nanocomposites[240–246]	
	CoO	715[239]	CoO composites[247–250]	
Manganese oxides	MnOx	700–1000[260,261]	Nanostructures[256,262,264] MnOx/carbon[266,267]	Possible solutions: 1. Metal oxide/carbon composites using carbon as buffer and electrode-active materials. 2. Nanostructured metal oxides to provide high surface area and quantum confinement effects.
Molybdenum oxides	MoO_3	1111[269,270]	Doped MoO_3[271–275]	
	MoO_2	830[269,270]	MoO_2 nanomaterials[276]	
Copper oxides	CuO	674[284,285]	Nanostructured CuO[278,279,283–291]	
	Cu_2O	375[293]	Cu_2O/Carbon composites[294–298]	
Chromium oxides	Cr_2O_3	1058[299]	Nanostructures, hetero-atom doping, and carbon-based nanocomposites[300–302]	
Nickel oxides	NiO	718[203]	NiO/carbon[303] Porous NiO[304]	
Ruthenium oxides	RuO_2	1130[305]	SnO_2/RuO_2[306,307]	

Due to the large theoretical specific capacity (1007 mA h g^{-1} for Fe_2O_3 and 926 mA h g^{-1} for Fe_3O_4), low cost, non-toxicity and environmental benignity, iron oxides have been considered as promising carbon alternative anode materials for high-capacity lithium ion batteries. Iron is the

fourth abundant element in the earth crust. It is abundant and has much lower cost than other 3d metal oxides such as Co and Ni. Thus, our attempt to improve the performance of LIBs focuses on the iron oxides based anode materials. Similar to most other 3d transition metal oxides, iron oxides materials suffer from severe volume variation during the insertion/extraction of Li ions and poor conductivity. To address those challenges, one strategy is to design and tailor the size and the (nano- or micro-) structure of materials to increase the contact area, enhance the stability of structure and facilitate the electrolyte/electron diffusion; the other is to prepare metal oxide/carbon composite to increase the conductivity and buffer the volume change of metal oxide materials during the insertion/extraction of Li ions.

2.3 Nano-/Micro-structured materials in LIBs application

Nanomaterials have been received a great amount of attention in the recent years for their unique properties as compared to bulk materials. Engineering materials at the nanoscale offers unique properties, results in higher performance electrodes and electrolytes and in various energy storage devices. Various nanomaterials with different morphologies have been synthesized to successfully improve the energy density, power density and stability/sustainability of the energy storage devices.

There are several advantages of applying nanotechnologies in LIBs application. First of all, the reduced size of materials can increase the rate of lithium insertion/extraction because of shorter diffusion length. Secondly, the higher surface to volume ratio of nanomaterials ensures a higher contact area between solid materials and electrolytes facilitates the ion exchange and electrochemical reactions at the interface. Thirdly, the strain associated with intercalation of lithium ions can be better accommodated by nanomaterials, leading to a better electrical contact between particles.

Although nanostructured active materials have aforementioned advantages and have been widely applied to improve the electrochemical performance of electrode, such as specific capacity (mA h g^{-1}) and specific energy (W h g^{-1}), there are still concerns about the side reactions due to the high activity and surface to volume ratio of nanoparticles and the volumetric energy density due to the small mass (or tapped) density of nanoparticles. The volumetric properties of nanoparticles such as energy density or volumetric capacity are not such outstanding as compared to their gravimetric properties like specific energy or specific capacity. Hence, besides preparing nanoparticles, optimization of microstructures of electrode materials provides another route to improve the volumetric energy density or volumetric capacity of batteries, which are crucial in space-limited area, such as wearable devices, electric vehicles, aerospace, etc. However, due to the difficulty of Li to diffuse into the microsized structure (as compared to that into nanostructures), the structure and size of the microparticle should be carefully designed in order to achieve good electrochemical performance.

For example, the particle size of Sony's Nexelion Li-ion anode materials (amorphous alloy) are in micron range.[7] And it is mentioned in their related patents that the sizes of primary and secondary particles are 0.1-25 μm and 10-70 μm, respectively. The size of the particles are of great importance: undesirable reaction is generated between the surfaces of the particles and electrolyte solution to deteriorate a capacity and efficiency if particle size is too small; and reaction between the particles and Li hardly advances in the inner parts of the particles to decrease the capacity when particle size is too large.[8,9]

Besides the control of size and morphology of nano-/micro-structures of active materials, active materials-carbon composites have also been widely studied since carbon can act as both soft buffer component and conductive enhancer to improve the performance of the materials. Recent

references about nano-/micro- structured iron oxides and iron oxides/carbon composites have been summarized here to show the recent progress in this area.

2.3.1 Nanostructured and microstructured iron oxide

Iron oxide has been considered as a promising candidate as alternative anode materials for LIBs because of its low cost, abundance, high stability and environmental benignity. However, similar to other 3d-transition metal oxides, iron oxide also suffers from poor conductivity and large volume change during the lithiation/de-lithiation process, which limits its practical application. A lot of efforts have been made to address those shortcomings. One strategy is to prepare iron oxide materials in nanoscale or to engineer and tailor iron oxide materials in specific morphologies. The other is to prepare iron oxide/carbon composite materials to accommodate the volume expansion as well as increase the conductivity.

Various α-Fe_2O_3 with different dimensional structures have been synthesized, including 0-dimentional nanoparticles,[10] 1-dimentional wires,[11-13] belts,[12,14] rods,[15-17] tubes,[18,19] 2-dimentional flakes[20], disks[21] and rings,[22] 3-dimensional cubes,[23-25] spheres,[26-29] spindles,[26,30] urchins[31] and flowers[32] with solid, porous or hollow structures,[21,26,29,33-37] via different synthetic procedures, such as soft/hard template-assisted route, hydrothermal method, and sol-gel method. Particularly, hollow structures are of great interests as the hollow space can accommodate the large volume expansion during Li insertion.[26,32-36] Furthermore, it is always interesting and challenging to explore facile methods to prepare Fe_2O_3 with unique hollow structures.[38-41]

Those materials with controlled morphologies and sizes have been demonstrated to have superior performance in various fields, such as water treatment, photo-catalyst, gas sensor, as well as energy storage such as Li-ion batteries, etc. Depending on the size and morphology, the literature was classified into several groups: 1D- structure, 2D- structure, 3D- structure, porous

structure, and microstructure to reveal the importance of tailoring the size or morphology of materials in improving the performance of as-obtained materials.

1D structure

Xiaogang Wen et. al. reported the preparation of vertically aligned iron oxide nanobelt and nanowire arrays by direct thermal oxidation of iron substrates under the flow of O_2. Nanobelts (width, tens of nanometers; thickness, a few nanometers) were produced in the low-temperature region (~700°C) and cylindrical nanowires tens of nanometers thick were formed at relatively higher temperatures (~800°C). Both nanobelts and nanowires are mostly bicrystallites with a length of tens of micrometers which grow uniquely along the [110] direction.[12]

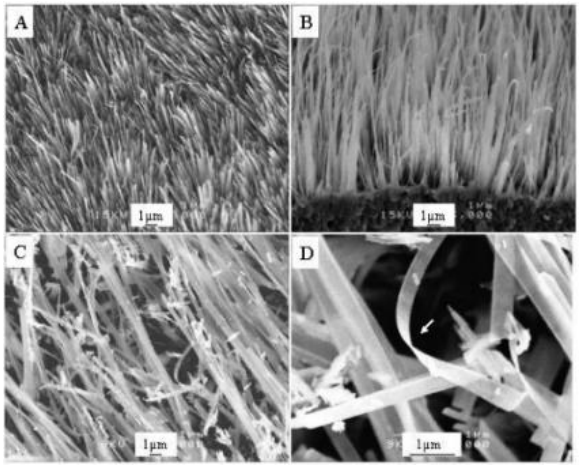

Fig. 2-4. Typical SEM images of the α-Fe_2O_3 nanobelt array: (A) top view; (B) side view; (C, D) low- and high-magnification images of the nanobelts lying down on the substrate. The nanobelt growth conditions are 700°C, 5 sccm of O_2, and 20 sccm of N_2. The reactor pressure was kept at ~1 atm.[12]

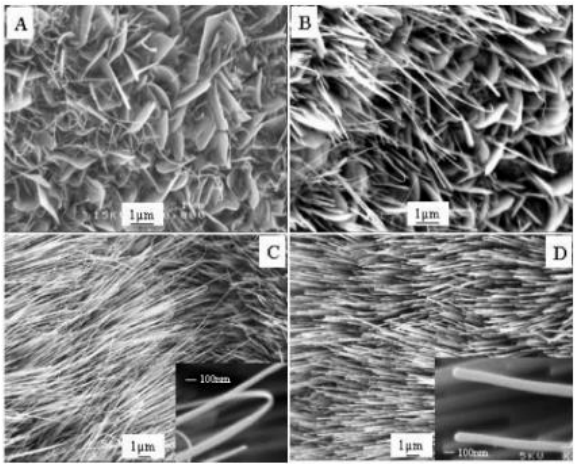

Fig. 2-5. SEM images of the α-Fe_2O_3 nanostructures synthesized at different temperatures: (A) 400°C; (B) 600°C; (C) 700°C; (D) 800°C. Gas flows: 5 sccm of O_2 and 20 sccm of N_2.[12]

α-Fe_2O_3 nanotubes have been prepared via hydrothermal synthesis and following calcination process, with the assistance of KCl, Na_2SO_4 or NH_4Cl.[42] The preliminary LIB test (only 1st cycle performance was exhibited) demonstrated that the nanotubes with higher surface area or porosity structures have higher initial discharge capacity (981, 1088, and 1151 mA h g^{-1} at current density of 0.2mA cm^{-2}, respectively, for a, b, and c in TEM images)

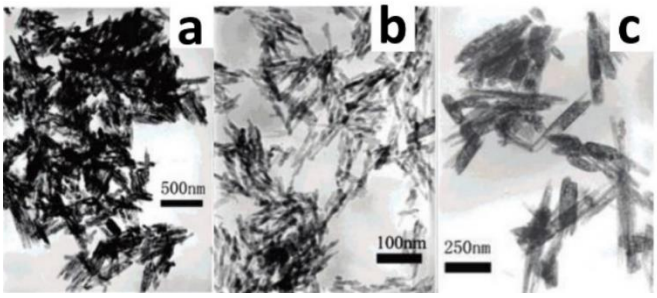

Fig. 2-6. TEM images of the as-obtained α -Fe_2O_3 nanotubes with different diameter sizes prepared with assistance of (a) KCl, (b) Na_2SO_4 or (c) NH_4Cl.[42]

2D structure

Jun Song Chen et. al. reported a top-down approach to fabricate uniform single-crystal α-Fe_2O_3 nanodiscs and also melon-like α-Fe_2O_3 microparticles through selective oxalic acid etching, using phosphate ions as capping agent to control the etching along [001] direction. The discharge

capacities of 662 and 341 mA h g^{-1} were retained [1] at 200 mA g^{-1} after 100 charge-discharges cycles, for porous and solid melon-like α-Fe_2O_3 microparticles, respectively.[21]

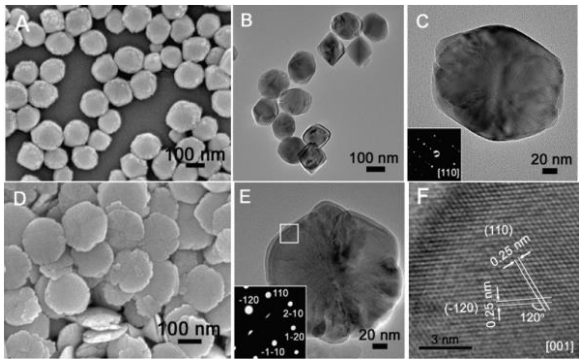

Fig. 2-7. FESEM image (A) and TEM images (B, C) of the α-Fe_2O_3 nanocrystals before etching. FESEM image (D) and TEM image (E) of the α-Fe_2O_3 nanodiscs obtained after etching. (F) High resolution TEM image of the region marked by white square in (E). The insets in (C) and (E) are SAED patterns of the corresponding sample.

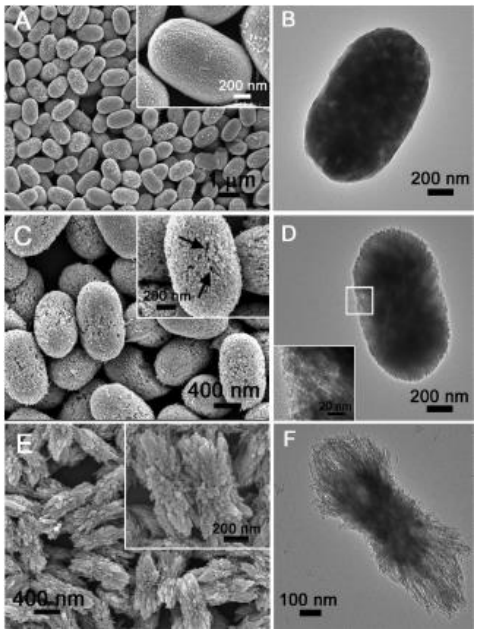

Fig. 2-8. FESEM images of samples I (A), II (C), and III (E) and TEM images of samples I (B), II (D), and III (F). The insets in (A), (C), and (E) are the magnified images of the corresponding sample, and that in (D) shows the magnified image of the region marked by the white square.

Besides, 2D Fe_2O_3 plates have also been prepared via hydrolysis of $Fe(acac)_3$ in ethanol solutions with a small amount of water using solvothermal method[43], or via the electrochemically

induced morphological transformation[44], which shows enhanced visible-light photocatalytic activity towards rhodamine B and remarkable capacitance, respectively.

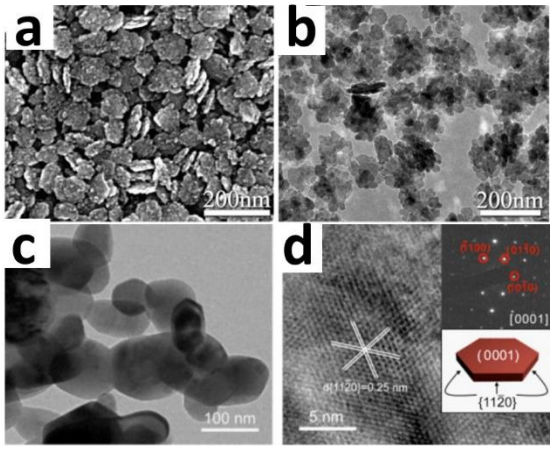

Fig. 2-9. (a) FESEM and (b) TEM images of hematite nanoflakes prepared via hydrolysis of $Fe(acac)_3$.[43] and (c-d) TEM and HRTEM of hematite nanoflakes prepared via electrochemically method.[44] Inset of (d) shows the SAED pattern collected from a nanoflake along the [0001] zone axis and a schematic illustration of a nanoflake with facets labeled.

Reddy et. al. reported the preparation of nanoflakes of α-Fe_2O_3 on Cu foil by using a thermal treatment method. The as prepared α-Fe_2O_3 nanoflakes exhibited a stable capacity of (680±20) mA h g^{-1}, corresponding to (4.05±0.05) moles of Li per mole of Fe_2O_3 with no noticeable capacity fading up to 80 cycles when cycled in the voltage range 0.005–3.0 V at 65 mA g^{-1} (0.1 C rate), and with a coulombic efficiency of > 98 % during cycling (after the 15th cycle).[20]

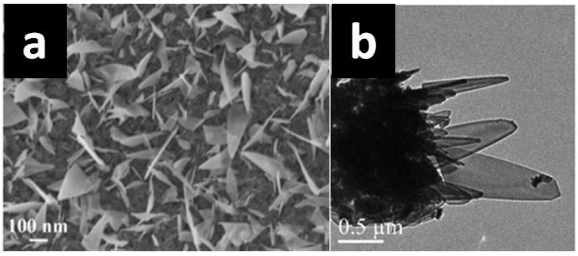

Fig. 2-10. (a) FESEM image and (b) high-resolution TEM image of α-Fe_2O_3 nanoflakes grown on a Cu substrate.

3D Structures

Xiaodong Xu et. al. reported the preparation of spindle-like porous α-Fe_2O_3 from an iron-based metal organic framework (MOF) template, MIL-88-Fe with the formula of $Fe_3O(H_2O)_2Cl(BDC)_3 \cdot nH_2O$. MIL-88-Fe was prepared by a modified solovthermal method based on earlier works, using $FeCl_3 \cdot 6H_2O$ and 1,4-benzenedicarboxylate (BDC) as starting materials. The as prepared spindle-like porous α-Fe_2O_3 exhibited very high charge capacity of 911 mA h g^{-1} after 50 cycles at current rate of 0.2C (1C =1000 mA g^{-1}). Meanwhile, the capacity of bulk Fe_2O_3 (<5μm, Sigma-Aldrich) quickly faded to less than 630 mA h g^{-1}. The spindle-like porous α-Fe_2O_3 also show a superior rate performance than bulk Fe_2O_3. [30]

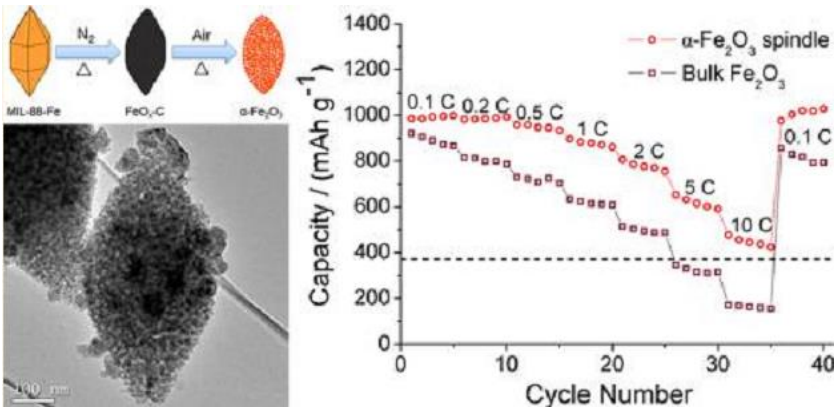

Fig. 2-11. Schematic illustration of the formation, TEM image and rate performance of spindle-like porous α-Fe_2O_3. [30]

Hollow Structure

Bao Wang et. al. reported the preparation of hollow α-Fe_2O_3 sphere with sheet-like subunits with quasiemulsion-templated methods. Glycerol was dispersed in water to form oil-in-water quasiemulsion microdroplets. The capacity of as prepared hollow spheres around 1μm faded very slowly from ~900 to 710 mA h g^{-1} after being charge/discharged from 2nd to 100th cycle, at current rate of 200 mA g^{-1}. Meanwhile, the capacity of α-Fe_2O_3 micropaticles faded from ~900 to 340 mA h g^{-1}, which was less than one half of the capacity retained of hollow spheres. [29]

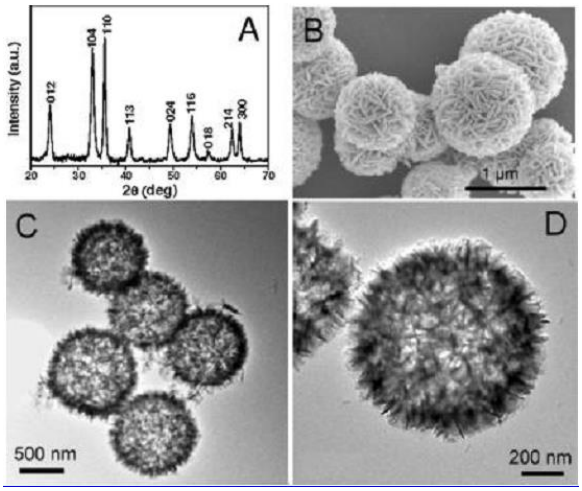

Fig. 2-12. (A) XRD, (B) SEM, and (C,D) TEM images of the α-Fe_2O_3 hierarchical hollow spheres prepared at 145ºC.

Microstructure

Iron oxides microparticles have also been studied to address the side reaction, and not-so-outstanding volumetric electrochemical property of nanoparticles. Hierarchical Fe_2O_3 microspheres ~1.75 μm with improved electrochemical performance (705 mA h g^{-1} at 100 mA g^{-1}) as compared to random nanoparticles has been prepared via hydrothermal process to address the issue of low volumetric energy density of Fe_2O_3 nanoparticles.[45]

Template method has been used to prepare multi-shelled hollow microspheres.[46] The number of shells can be controlled by Fe^{3+} concentration and thickness of the shell can be controlled by water:ethanol ratio. All thin shell samples exhibited higher capacity of >1500 mA h g^{-1} at 50 mA g^{-1}, which is much better than the capacity of ~500 mA h g^{-1} of all thick shell samples. The increased capacity can be attributed to reversible SEI formation and additional interfacial Li storage mechanism.

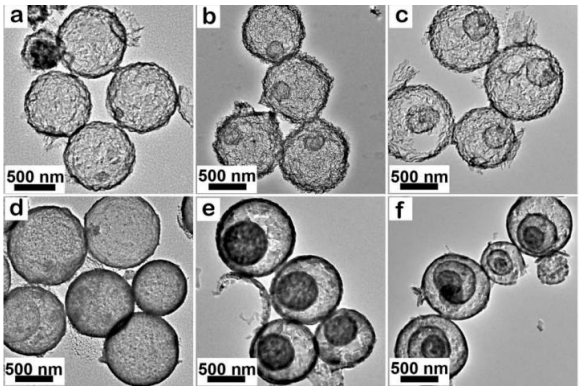

Fig. 2-13. TEM images of α-Fe_2O_3 multi-shelled hollow microspheres produced at 500°C; (a) thin single-shell, (b) thin double-shell, (c) thin triple-shell, (d) thick single-shell, (e) thick double-shell and (f) thick triple-shell.[46]

Another widely reported method to prepare microstructured iron oxides is the two step synthesis which include (1) the preparation of precursor such as $FeCO_3$ or iron alkoxide, and (2) calcination process to obtain iron oxides. The calcination process will not break the structure and the morphology can be maintained. $FeCO_3$ microsphere [47,48] or micropeanut[49] have been obtained via hydrothermal route and have been converted to Fe_2O_3 or Fe_3O_4 via calcination. (No electrochemical study was carried out in those references.) And iron alkoxide precursor such as $Fe(OH)_2(HOCH_2CH_2OH)$,[50] $HO–Fe(II)–C_2H_5O_2$,[51] $C_4H_4O_6Fe(II)$,[52] $C_2H4O_2Fe(II)$,[53] $FeOC_2H_5O_2$,[54] or iron alkoxide without detail chemical composition[55] with microsphere, micro-flower or micro-urchin structures have been prepared via solvothermal method. 450 mA h g^{-1} for Fe_3O_4 microspheres and 697 mA h g^{-1} for γ-Fe_2O_3 microspheres have been demonstrated.[52]

2.3.2 Iron oxides/Carbon composites

The electrochemical performance for iron oxides materials and also other materials who have huge volume variation or poor conductivities can be improved by decorating carbon nanoparticles or protective carbon layer/shell on the bare materials, because of the very important role the carbon coating particles or layers play in the following aspects:

1. Conductivity

The carbon coatings can enhance the conductivity of each single units as well as improve the better electric contact between each single units due to its soft nature. It helps to achieve a better performance under higher current rate.

2. Buffer the volume expansion

The soft carbon coatings can also act as a buffer layer to alleviate the stress caused by huge volume expansion of M_xO_y (M= Mn, Fe, Co, Ni, Cu, etc.), prevent the nano-/micro- sized structure from collapsing. It makes the structure of the materials more stable, resulting in a better cyclability.

3. Protect the electrolyte from unwanted oxidation and reduction by the electrode materials.

The nanosized materials are more active than bulk materials, the high contact area between electrode and electrolyte may lead to more significant side reactions. The carbon coated layer can act as a protective layer to prevent the direct contact between the highly-reactive nanomaterials and the electrolyte to increase the sustainability of the LIB system.

One of the most commonly used way to coat the carbon on materials is the chemical vapor deposition method (CVD), which is carried out under the protection of inert gas at a high temperature of more than 500^oC. Under such condition, Fe_2O_3 will be reduced by carbon to Fe_3O_4. Thus, Fe_3O_4 / carbon is a more common and stable existence of iron oxides/ carbon composites. The coating of carbon on Fe_2O_3 or Fe_3O_4 is proved to be an effective way to enhance the electrochemical performance for as prepared materials, as compared to bare materials without carbon coating.

Zhiyu Wang et. al. [56] reported a novel hierarchical nanostructure composed of carbon coated α- Fe_2O_3 hollow nanohorns grafted on CNT backbones (denoted as CNT@Fe_2O_3) by bottom-up assembly of β-FeOOH nanospindles on CNTs and subsequent *in-situ* phase and structure transformation and further modification with carbon nanocoating. The specific capacity of carbon-

coated CNT@ Fe_2O_3 hollow nanohorns gradually rose from 660 to 820 mA h g^{-1} from 2nd to 100th cycle at current density of 500mA g^{-1}, while the capacity of uncoated CNT@ Fe_2O_3 slowly faded from 1200 to around 500mA h g^{-1}, from 1st to 100th cycle. Both materials show superior performance compared to α- Fe_2O_3 nanoparticles, which had a capacity of 300mA h g^{-1} after 100 cycles.

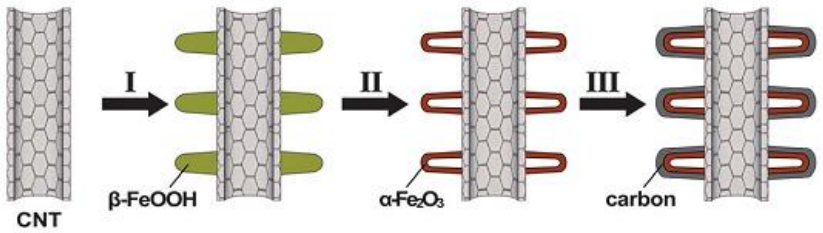

Fig. 2-14. Schematic illustration of the formation of carbon coated α- Fe_2O_3 hollow nanohorns on the CNT backbone: (I) heterogeneous growth of β -FeOOH nanospindles on CNTs by force hydrolysis of Fe^{3+} ions; (II) thermal transformation of β -FeOOH nanospindles to α- Fe_2O_3 hollow nanohorns on CNTs by annealing CNT@FeOOH structures in air and (III) carbon nanocoating of CNT@ Fe_2O_3 hierarchical structures by hydrothermal carbonization of glucose.

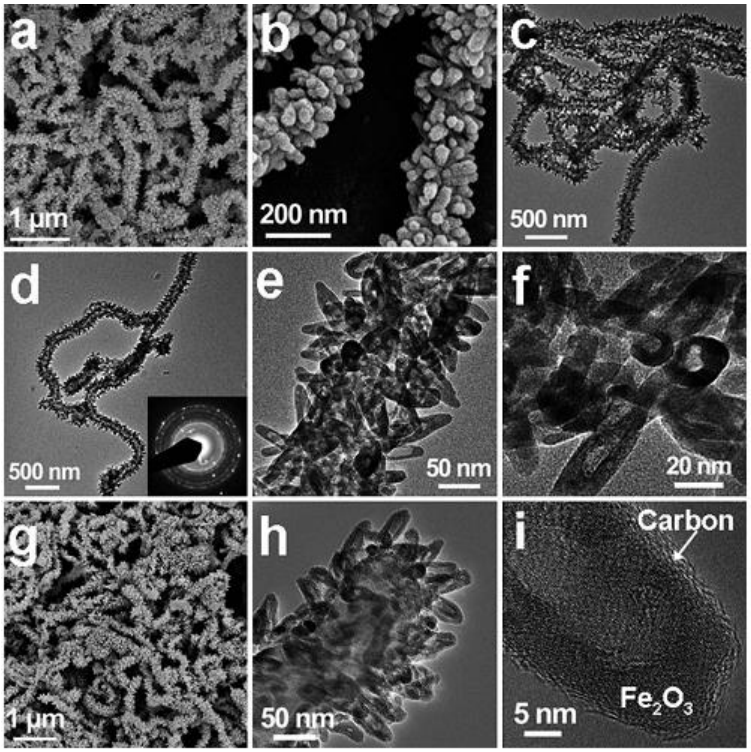

Fig. 2-15. (a, b) FESEM images and (c, d) TEM images of CNT@ Fe_2O_3 hierarchical structures; (e, f) TEM images revealing the formation of hollow nanohorns on CNT backbones; (g) FESEM image and (h) TEM image of carbon-coated CNT@ Fe_2O_3 hierarchical structures; (i) HRTEM image of uniform carbon nanocoating on α- Fe_2O_3 hollow nanohorns.

Hematite nanospindles with carbon coatings were prepared by two-step hydrothermal method, and the carbon coated magnetite nanospindles were prepared by in situ partial reduction of hematite spindles with carbon coatings, reported by Wei-Ming Zhang et. al..[57] The specific capacity of Fe_3O_4 spindle/carbon composites remained 530 mA h g^{-1} even after another 5 discharge/charge cycles at C/5 and 75 discharge/charge cycles at C/2 in series (1C = 805 mA g^{-1}), while the specific capacities of the bare α-Fe_2O_3 spindles and the commercial Fe_3O_4 particles (Alfa Aesar,300 nm in diameter) faded to 105 and around 152 mA h g^{-1}, respectively.

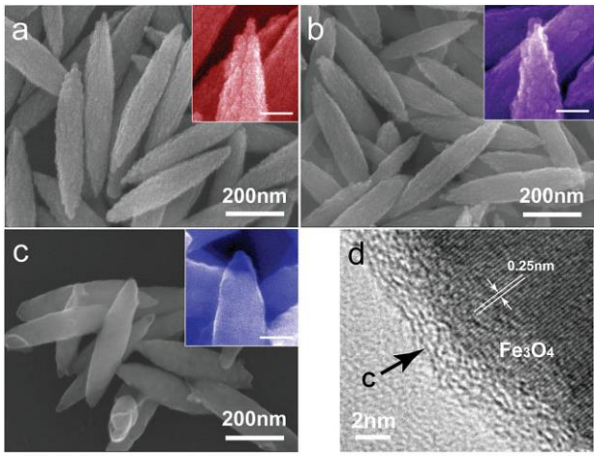

Fig. 2-16. a) SEM image of the as-synthesized hematite spindles. b) SEM image of the carbon precursor coated hematite spindles. c) SEM image of the carbon coated Fe3O4spindles (Fe_3O_4–C composites). d) High-resolution TEM image of the Fe_3O_4–C composites. The insets are close views of corresponding samples. All unmarked scale bars are 50 nm. [57]

Yang, Z. et. al. reported a facile, scalable emulsion polymerization technique for synthesizing Fe_3O_4 nanoparticles around 20nm embedded in a porous carbon matrix.[58] The as prepared materials had specific capacities around 600 and 450 mA h g^{-1} with little fading after being discharged/charged at current rates of 1C and 0.2C, respectively.

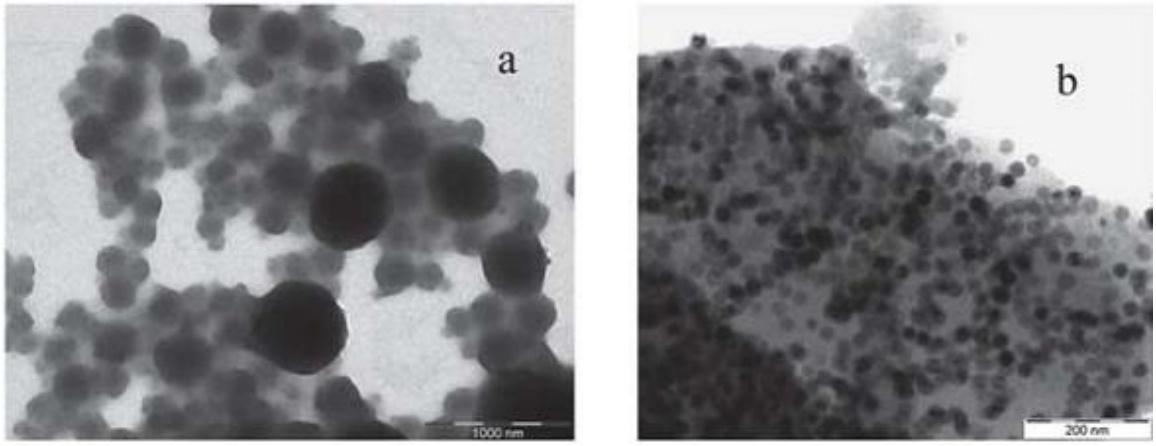

Fig. 2-17. (a) Morphology of polymer–iron complex; (b) morphology of Fe_3O_4 -C composite.

Lili Wang et. al. successfully synthesized Fe_3O_4@C core–shell nanorings (R- Fe_3O_4@C) via a synchronous reduction and carbon deposition process from the reduction of the Fe_2O_3 nanoring precursor with the assistance of acetylene. Erythrocyte-like nanoparticles (E-Fe_3O_4@C) was prepared as a comparison without the presence of Na_2SO_4.[59] The specific capacity of R- Fe_3O_4@C stabilized at around 900 mA h g^{-1} after recharged for 160 cycles at current rate of 200mA g^{-1}, while the capacity of E- Fe_3O_4@C dropped to around 470 mA h g^{-1} after 160 cycles. The shorter pathway for lithium-ion diffusion, empty space in the structures, more exposed active sites, and conductive carbon shells all contribute to the superior electrochemical performance.

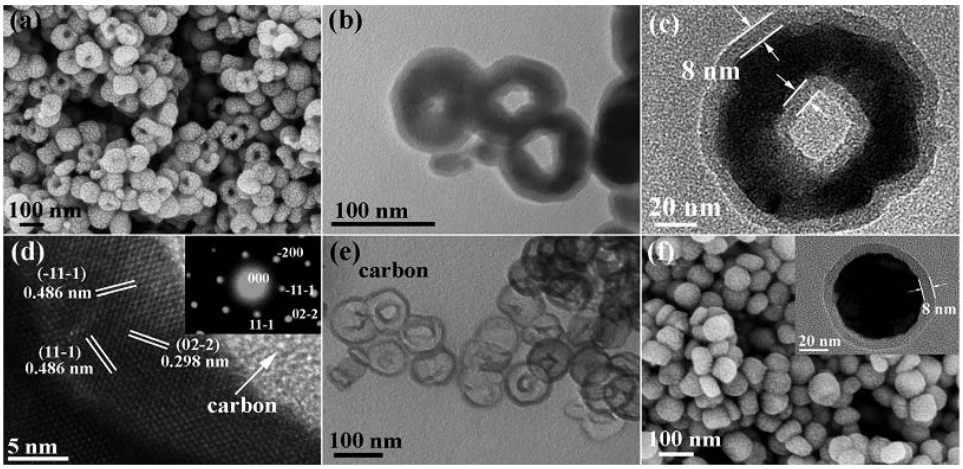

Fig. 2-18. (a, b) SEM and TEM images of R- Fe_3O_4@C; (c) high magnification TEM image and (d)HRTEM image and (inset) SAED patterns of R- Fe_3O_4@C; (e) TEM image of the carbon shell; (f) SEM and (inset) TEM images of E-Fe_3O_4@C.[59]

Y. G. Zhu et. al. reported a facile self-templating route to synthesize core-shell structured of C/ Fe_3O_4/C nanotubes using Fe_2O_3 as the self-templates which was prepared using hydrothermal method, by a chemical vapor deposition (CVD) method. After 120 charge/discharge cycles at 100mA g^{-1}, C/ Fe_3O_4/C retained a discharge capacity of over 700 mAh g^{-1}, while the discharge capacities of α- Fe_2O_3 and bare Fe_2O_3 nanotubes rapidly dropped to about 100 mAh g^{-1} after 30 cycles. The improvement in cycling stability could be attributed to the introduction of carbon film which acts as both a buffer to alleviate the volume changes and a fixer to confine Fe_3O_4 nanotube core in between two carbon shells.[60]

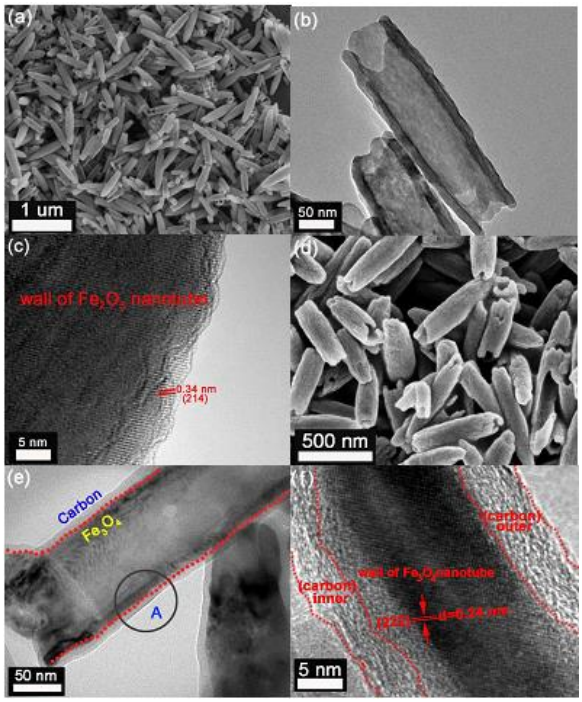

Fig. 2-19. (a) SEM image (b) TEM image and (c) HRTEM image of Fe_2O_3 nanotubes; (d) SEM image, (e) TEM image and (f) HRTEM image of C/Fe_3O_4/C nanotubes.

Shuangling Jin et. al. reported the preparation of flower-like Fe_2O_3 and Fe_3O_4/carbon nanocomposite with nano/micro hierarchical structure by controlled thermal decomposition of the

iron alkoxide precursor, which was obtained via an ethylene glycol-mediated solvothermal reaction of $FeCl_3$ and hexamethylenetetramine (HMT) in the absence of any surfactant. The Fe_3O_4/carbon prepared by calcinating the iron alkoxide precursor at 450^oC in nitrogen gas (N450, Fe_3O_4/carbon) and air (A450, α-Fe_2O_3) had their specific capacities retained at 1030 and 1150 mA h g^{-1} after 150 charge-discharge cycles at current rate of 0.2C. (1C = 924 and 1007 mA g^{-1} for Fe_3O_4 and Fe_2O_3, respectively) [61]

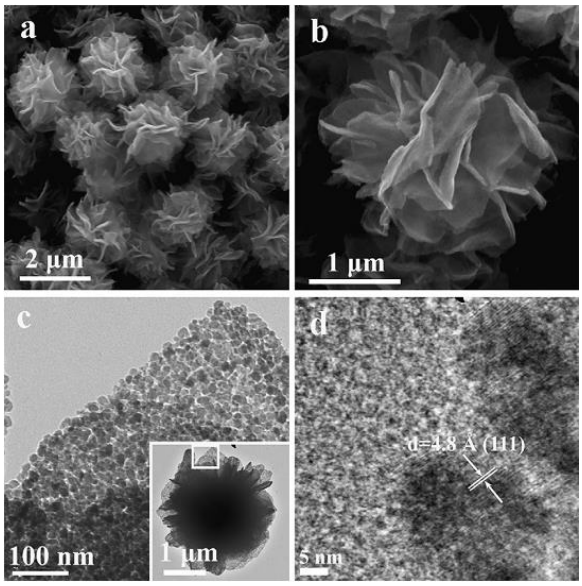

Fig. 2-20. (a) Low-magnification and (b) high-magnification SEM images of N450, (c) high-magnification TEM image of the flake of the flowerlike structure of N450 (inset) and (d) high-resolution TEM image taken from the Fe_3O_4 nanoparticles.

2.4 Summary of the literature review

Table 2-2 Summary of iron oxides based anode materials for Li-ion batteries.[62]

Table 1. Summary of the representative iron oxide-based anode materials for lithium-ion batteries.

Strategies	Typical examples	Electrochemical properties	Ref.
Nanostructuring	Porous α-Fe_2O_3 microparticles	662 mA h g^{-1} after 100 cycles at a current density of 200 mA g^{-1}	[21]
	α-Fe_2O_3 nanowires	456 mA h g^{-1} after 100 cycles at 0.1 C	[24]
	Microflower-like α-Fe_2O_3 constructed by sheet-like subunits	929 mA h g^{-1} after 10 cycles at a current density of 100 mA g^{-1}	[26]
	Single crystalline α-Fe_2O_3 nanosheets grown directly on Ni foam	518 mA h g^{-1} after 50 cycles at 0.1 C	[28]
	Single-crystalline α-Fe_2O_3 nanosheets on conductive substrates	700 mA h g^{-1} after 80 cycles at a current density of 65 mA g^{-1}	[29]
Hollow structures	Hierarchical α-Fe_2O_3 hollow spheres with sheet-like subunits	710 mA h g^{-1} after 100 cycles at a current density of 200 mA g^{-1}	[32]
	Hierarchical hollow Fe_3O_4 microspheres	580 mA h g^{-1} after 100 cycles at a current density of 200 mA g^{-1}	[33]
	Polycrystalline α-Fe_2O_3 nanotubes	1000 mA h g^{-1} after 50 cycles at 0.5 C, 500–800 mA h g^{-1} at 1–2 C	[35]
	Hierarchical Fe_2O_3 microboxes	945 mA h g^{-1} after 30 cycles at a current density of 200 mA g^{-1}	[36]
Carbon nanocoating	Carbon-coated Fe_3O_4 nanospindles	530 mA h g^{-1} after 80 cycles at 0.5 C	[61]
	Carbon-coated Fe_3O_4 nanorods	808 mA h g^{-1} after 100 cycles at a current density of 924 mA g^{-1}	[62]
	Fe_3O_4 nanospheres within carbon matrix support	712 mA h g^{-1} after 60 cycles at a current density of 200 mA g^{-1}	[63]
Embedding into carbon matrix	Carbon-Fe_3O_4 composite nanofibers	1000 mA h g^{-1} after 80 cycles at a current density of 200 mA g^{-1}	[64]
	2D ferrite/carbon hybrid nanosheets	600 mA h g^{-1} after 50 cycles at a current density of 100 mA g^{-1}	[65]
Hybridization with carbon nanotubes	Fe_3O_4 nanoparticles embedded in an interconnected SWNTs network	1000 mA h g^{-1} after 50 cycles at 0.5 C	[69]
	Carbon-coated α-Fe_2O_3 hollow nanohorns grafted on CNT backbones	800 mA h g^{-1} after 100 cycles at a current density of 500 mA g^{-1}	[70]
Hybridization with graphene	Interleaved composite of graphene nanosheets and decorated Fe_3O_4 particles	1000 mA h g^{-1} after 30 cycles at a current density of 35 mA g^{-1}	[72]
	3D graphene foams cross-linked with Fe_3O_4 nanospheres encapsulated with graphene	1059 mA h g^{-1} after 150 cycles at a current density of 93 mA g^{-1}	[78]

Besides aforementioned literatures, there are many other reports about iron oxides anode materials for Li-ion battery applications, which is summarized in Table 2-2.[62] Based on the review of iron oxides anode materials, it is clear that the size (either in nano- or in micro-scale) and the shape of both primary and secondary structures, and the hierarchical structure or the composites of iron oxides-carbon are all proved to be effective to enhance the performance (electrochemical performance or other application performances) of active materials. Our research on tuning the size, shape and hierarchical structures of iron-oxides anode materials and the effort to improve the battery performance via those tuned structures will be discussed in detail starting from the next chapter.

CHAPTER 3. EXPERIMENTAL SECTION

3.1 Preparation of microsized solid α-Fe_2O_3 rhombohedra

In a typical procedure, 0.4mmol of $FeCl_3 \cdot 6H_2O$ was dissolved in 16ml of deionized water. The fresh $FeCl_3$ aqueous solution was dropwise added into 16ml of 1-propanol under stirring. The mixture was then transferred to a 45ml Teflon-lined autoclave and heated at 150 °C or 200°C for 75 min. The dark red precipitates were collected by centrifugation, washed repeatedly with deionized water and ethanol, and dried in vacuum oven. The as prepared samples were named with S150 and S200, respectively.

3.2 Preparation of hollow α-Fe_2O_3 microframes

In a typical procedure, as-prepared α-Fe_2O_3 microparticle with tunnels (Section 4.2) as precursor were placed in an alumina crucible, heated in quartz tube furnace in Ar flow at 600^oC for 2 h with ramping rate of 6 ^oC/min, and then cooled down to room temperature in Ar flow. The flow rate of Ar flow was 100sccm.

3.3 Preparation of hollow α-Fe_2O_3 nanococoons

In a typical procedure, a solution of 0.4mmol $FeCl_3 \cdot 6H_2O$ dissolved in 16ml water was added into an another solution of 0.4mmol of dimethyl oxalate dissolved in 16ml 1-propanol drop-wise under stirring. The mixture was then transferred to a 45ml Teflon-lined autoclave and heated at 200 °C for 3 h. The solid products were collected by centrifugation, washed repeatedly with water and ethanol, and dried in vacuum oven.

3.4 Preparation of α-Fe_2O_3 chevron microbeads

In a typical procedure, 0.4 mmol of $FeCl_3 \cdot 6H_2O$ and 0.1 mmol of D-glucose were dissolved in 16 ml of DI-water (solution A), and 0.25 mmol of dimethyl oxalate (DMO) was dissolved in 16 ml of 1-propanol (solution B). Solution A was added drop-wise into solution B under stirring, and

the mixture was stirred for 15 min. The mixture was then transferred to a 50 ml Teflon-lined autoclave (notice that the volume of the reactor is 5ml larger than other experiments due to different design of the new reactors, the cap of old reactor occupies 5ml so the old reactors have different volume of 45ml) and heated at 200 °C for 3 h. The solid product of α-Fe_2O_3 microscale chevron beads in red color was washed repeatedly with water and ethanol, collected by centrifugation and dried in vacuum oven overnight.

3.5 Preparation porous olive-like α-Fe_2O_3/carbon and hollow Fe_3O_4/carbon composites

In a typical procedure, 0.4mmol of $FeCl_3 \cdot 6H_2O$ and 0.4mmol of D-(+)-glucose were dissolved in 16ml of deionized water. The mixture was dropwise added into 16ml of 1-propanol under stirring. The mixture was then transferred to a 45ml Teflon-lined autoclave and heated at 200 °C for 75min. The dark red precipitates were collected by centrifugation, washed repeatedly with deionized water and ethanol, and dried in vacuum oven. To prepared Fe_3O_4/C composite, the dried sample was placed into a crucible in tube furnace, heated at 600^{o}C for 2h with heating rate of 20^{o}C/ min, protected by argon gas with flow rate of 100sccm.

3.6 Centrifugation-assisted preparation of additive-free electrode

For α-Fe_2O_3 microframes (Section 4.3) and Fe_3O_4/C composites (Section 4.5) which were prepared via Ar-protected calcination process, additive free electrodes were prepared from precursor-coated electrode under the same annealing condition as mentioned in Section 4.3 and Section 4.5. The precursor-coated electrodes were prepared by centrifugation-assisted deposition. Typically, the solvothermally obtained precursors were dispersed into 5ml of pure ethanol in a 50ml centrifuge tube after wash. A piece of Cu disc (0.4x0.4 cm^2) was put into the centrifuge tube. The dispersion was centrifuged at 6000 rmp for 5 min. The Cu discs uniformly covered by α-

precursor were collected and dried in vacuum oven at 50 ^{o}C overnight. The precursor coated Cu discs were placed in a crucible and were annealed following the same calcination conditions aforementioned. The centrifugation-annealing process to prepare additive-free electrode was named centrifugation-assisted preparation (CAP) to facilitate the discussion in this thesis.

3.7 Materials characterization

Powder X-ray diffraction (XRD) was carried out with Rigaku Smartlab X-ray diffractometer using Cu K_α radiation (λ=0.15418 nm). Scherrer equation was used to estimate the crystalline size**:**

$$\tau = \frac{K\lambda}{\beta cos\theta}$$

where τ is the mean size of the ordered (crystalline) domains, K is a dimensionless shape factor, a typical value of 0.89 for K was used . λ is the X-ray wavelength, and 0.154nm for Cu K_α radiation was used here. β is the line broadening at half the maximum intensity (in radians). θ is the Bragg angle. Energy dispersive X-ray spectroscopy (EDS) and morphology characterization were carried out on a field emission scanning electron microscope (FESEM, JSM-7600, equipped with Pegasus Apex 2 integrated EDS) with an accelerating voltage of 15 kV, and transmission electron microscopy (TEM, JEOL 2010) with accelerating voltage of 200 kV. Thermal gravimetric analysis (TGA) was carried out with SDT Q600 (TA Instruments). Measurements of Brunauer–Emmett–Teller (BET) surface areas and pore size distribution were carried out using N2 adsorption/desorption isotherm surface area analyzers (Tristar II 3020).

Electrochemical Measurements: The electrochemical measurements were carried out in 2032-type coin cells. Homogeneous slurry was prepared by well mixing the as prepared iron oxides materials, conductivity enhancer (Super-P carbon black, Timcal), and polyvinylidene fluoride (PVDF) binder in weigh ration of 80:10:10 in N-methylpyrrolidone (NMP). The slurry was then applied to a copper disc current collector and dried in vacuum oven at 100^{o}C for 24h.

Electrochemical test cells were assembled in an argon-filled glove box using the coated copper disc as the working electrode, metallic lithium foil as the counter and reference electrode, 1 M solution of $LiPF_6$ in a mixture of ethylene carbonate (EC) and diethyl carbonate (DEC) (1: 1, v/v) as the electrolyte, and PP/PE/PP trilayer membranes (Celgard 2320) as the separator. The cells were charged and discharged galvanostatically at room temperature on a MTI BST8-WA battery tester. Faraday's law was used to calculate theoretical capacity:

$$C = \frac{nF}{t\ M_w}$$

where C is the theoretical capacity (mA h g^{-1}). F is Faraday's constant with value of 9.65 x 10^4 C mol^{-1}(1C = 1A·s). n is the valence charge, t is the time, and M_w is the atomic mass of active materials.

CHAPTER 4. α-Fe_2O_3 MICROSTRUCTURES

The improvement battery performance achieved through structure of electrode materials can generally achieved through (1) optimization of microstructures; (2) preparing nanoparticles; or (3) preparing nanocomposite materials or hierarchical structures. And the work in this chapter is about the optimization of microstructures of α-Fe_2O_3.

Due to the concern of low tap density of nanoparticles, though nanomaterials exhibits excellent gravimetric energy density or gravimetric capacity, their volumetric energy density or volumetric capacity are not such outstanding as compared to their gravimetric properties. Hence, besides preparing nanoparticles, optimization of microstructures of electrode materials provides another route to improve the volumetric energy density or volumetric capacity, which are crucial in space-limited area, such as wearable devices, electric vehicles, etc.

There are two general routes to optimize the microstructure, either through preparing structure with highly reactive surface or high-index facets; or through the control of the morphology of microstructures. Both strategies to optimize the microstructure can effectively improve the performance of active materials or batteries.

4.1 Microsized solid α-Fe_2O_3 rhombohedra

The controlled synthesis of inorganic single crystals with a large percentage of exposed high-index facets has attracted much research attention, owing to their scientific importance associated with highly reactive surfaces.[63] However, high-index facets usually disappear during the early stage of growth of crystals due to the minimization of surface energy, leading to most of the single crystals enclosed with high-index facets reported in literature existing in the nanoscale and typically facet-controlling agents are employed.[64,65] Han, et al. reported the preparation of SnO_2 octahedral nanoparticles with exposed high-index {221} facets by hydrothermal methods with the

assistance of HCl and PVP. The nanocrystals are in the size about 200 nm showing excellent gas-sensing performance.[64] Zhou, et al reported the preparation of α-Fe_2O_3 nanocubes with dominant {012} facets at size of 22 nm, which shown improved photocatalytic properties over nanoplates with dominant {001}facets.[65] Microscale monodisperse single crystals with exposed high-index facets are rarely reported. Yang, et al. prepared microscale TiO_2 single crystals enclosed by 47% {001} facets using fluoride ions as a facet-controlling agent.[63] This report rekindled another waves of interest in exploring inorganic materials with large exposed high-energy surfaces.[66-70] Due to the aforementioned energy minimization, it is still challenging and intellectually interesting to prepare single crystal enclosed by high-index facets at microscale.

Among inorganic materials, hematite α- Fe_2O_3 has been attracting much attention for its environmental benignity, abundance, and low cost. Hematite α-Fe_2O_3 can find wide applications in environmental remediation, catalysis, sensors, and energy storage. Monodisperse single crystals of α- Fe_2O_3 in microscale with high-index facets would be a good model to reveal many fundamentals of facet-related properties and applications. Although different hematite structures in nanoscale have been synthesized, such as zero-dimensional (0D) nanoparticles,[10] 1-D nanowires,[11,13,62] nanobelts,[12,14] nanorods[15,62] and nanotubes,[18,19,71] 2-D nanoflakes,[20] nanodisks, and nanorings,[21,22] 3-D nanocubes,[23,72] nanospheres,[26,73] nanospindles,[26,30] nanourchins,[31] nanoflowers[32] and microbox,[74] there are few reports on practical facile preparation of microscale hematite single crystals with exposed high-index facets with good size distribution. Microcrystals of α-Fe_2O_3 plates prepared with the assistance of NaOH and oleic acid have a broad size distribution.[75] The surface energies of hematite calculated based on density function for {001}, {101}, {104} facets are 1.146, 1.308, 1.453 J/m^2 respectively.[76] Given the higher surface energy of {104} facet than that of {001} and {101} facets, it is harder to fabricate single microcrystal

hematite with exposed {104} facets than that of {001} or {101}. It is also very challenging to achieve good size distribution for microsize α-Fe_2O_3 with exposed high-index facets.

In this work, we report a facile fast one-pot hydrothermal method to prepare monodisperse single microcrystal rhombohedral α-Fe_2O_3 enclosed with {104} facets in a very short reaction time of 75min, which is much shorter than typical hydrothermal reaction time of 24h or even longer. The evolution of morphology was studied by ex situ characterization based on time of reaction. The effects of reaction temperature and solvents on the morphology were extensively explored. The formation mechanism was revealed based on a set of time-dependent experiments and ex situ characterization. Its potential application as carbon-alternative anode materials for lithium ion batteries was demonstrated by high capacity, improved cyclability, and good rate performance. The specific capacity could be maintained at above 550 mA h g^{-1} after 120 cycles at rate of 200 mA g^{-1}, and the specific capacity could be resumed back to 617 mA h g^{-1} after the rate changed to 100 mA g^{-1} from a high rate of 1500 mA g^{-1} at the 100th cycle.

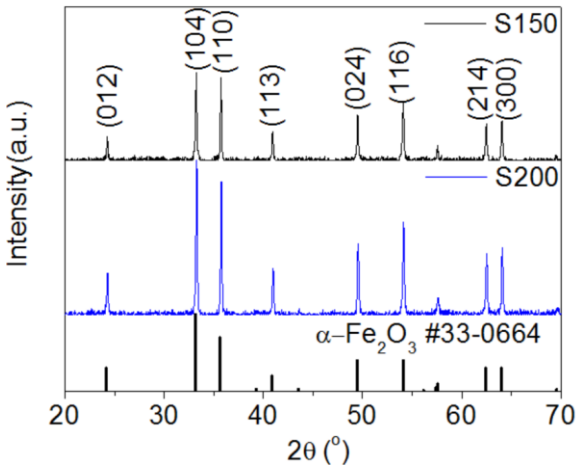

Fig.4-1-1. XRD pattern of α-Fe_2O_3 rhombohedra samples S150 (black) and S200 (blue)

XRD patterns of samples S150 and S200 (obtained at 150 and 200 °C hydrothermally, respectively, as described in Experimental Section) are shown in Figure 4-1-1. All the identified

diffraction peaks can be assigned to α-Fe_2O_3 (JCPDS card no. 33-0664). No other phase was observed, indicating a high phase purity of the as-prepared materials. The sharp diffraction peaks and lack of broadness suggests good crystallinity of the samples obtained with a very short period of reaction time of 75 min. Better crystallinity of the sample obtained at 200 °C than that of 150 °C was demonstrated by the even stronger intensity of its diffraction peaks (S200 vs S150 in Figure 4-1-1), which suggest that higher temperature could further improve their crystallinity. The TGA results of the as-prepared S150 and S200 samples are shown in Figure 4-1-2. The weight loss of S150 before 200 °C is 0.2%, which could be attributed to the loss of physically absorbed water. The weight loss between 200 and 500 °C is 1.9%, which could be ascribed to the loss of hydroxyl groups on the surface.[77] No distinguishable loss of weight was observed for S200 before 200 °C, indicating a minimum amount of physically absorbed water. The weight loss between 200 and 500 °C is 1.6%, which is less than that of S150.

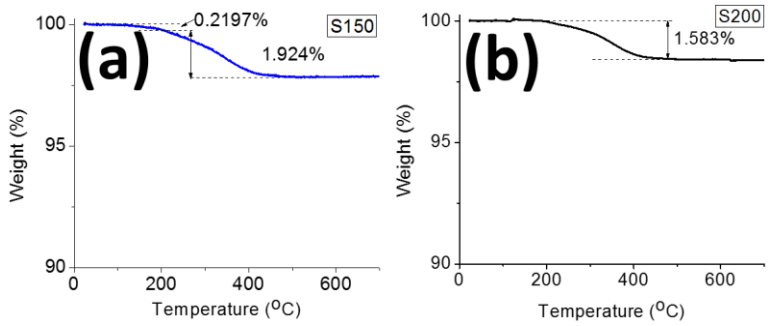

Fig.4-1-2. TGA of α-Fe_2O_3 rhombohedra samples (a) S150 and (b) S200.

The morphology of the monodisperse α-Fe_2O_3 rhombohedra was characterized by FESEM images (Figure 4-1-3). Low magnification FESEM images (Figure 4-1-3, a and c), demonstrate a very good size distribution for both samples S150 and S200. Relatively good size distribution was achieved: for sample S150, the mean size was estimated to be 763 nm averaged from 123 particles; for S200, the mean size was 920 nm averaged from 100 particles (Figure 4-1-4). Details of the

typical rhombohedral microparticles are revealed by high-magnification FESEM images (Figure 4-1-3, b and d). The microscale rhombohedra of S150 have clear edges and shape outline. There are still small amount of smaller nanoparticles visible on the surface of the rhombohedra (Figure 4-1-3b). The surface of S200 is smoother, and the size of the microparticles is also larger as compared to S150. Further analysis shows that the edges of the rhombohedra were slightly etched, and cracks appeared on the edges as revealed by the zoom-in view (Figure 4-1-3d).

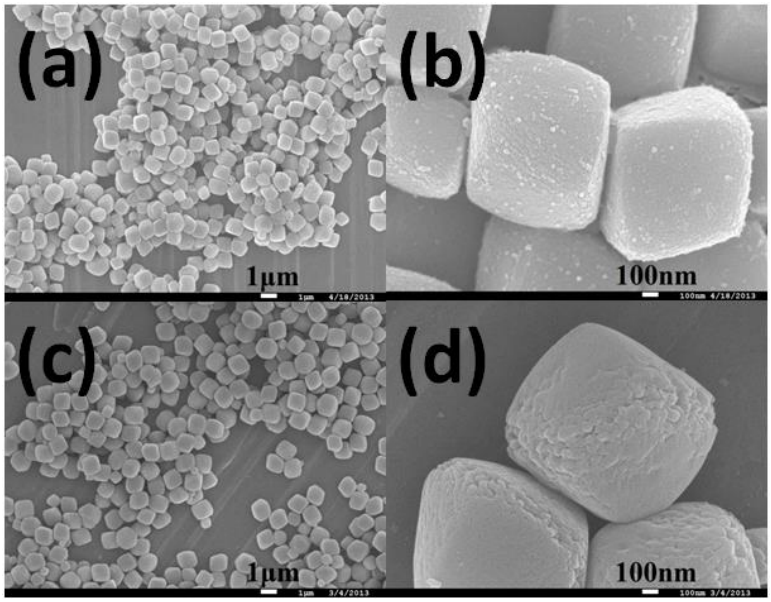

Fig. 4-1-3. FESEM images of (a,b)S150 (c,d)S200.

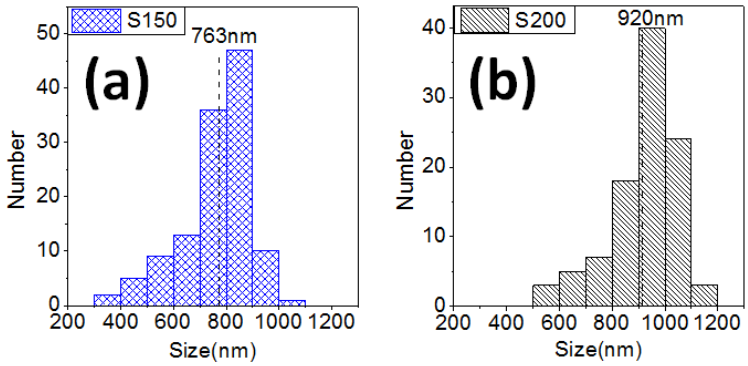

Fig. 4-1-4. Size distribution of (a) S150 (blue) and (b) S200 (Black). Note: The size of each rhombohedron was measured between two parallel edges in the same face, instead of diagonal line or corner-to-corner measurement which could be significantly larger than distance of two parallel

edges. The faces selected for measurement are those more or less parallel to viewing screen. More than 100 particles were measured in low magnification FESEM images.

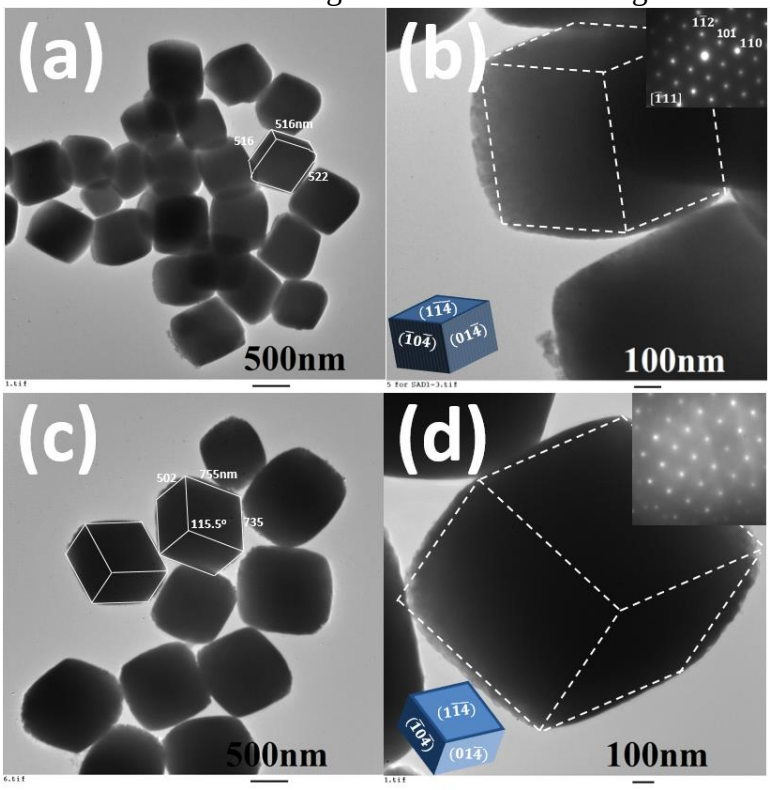

Fig. 4-1-5. TEM images of (a and b) S150 and (c and d) S200. The insets are the SAED pattern and the schematic illustration of the rhombohedra structure.

The morphology and crystallinity of the typical rhombohedral structures of S150 and S200 were further revealed by TEM and SAED (Figure 4-1-5). In accordance with the aforementioned FESEM observation, monodispersity and rhombohedral shape are further confirmed (Figure 4-1-5, a and c). The lengths of edges are about 520 and 760 nm for S150 and S200, respectively, for the selected particles. The different projected images in TEM observation are due to difference in orientation of those rhombohedra sitting on the TEM grid or tilted rhombohedral structures. White outlines were used to highlight the edges of few typical rhombohedra. The TEM images at higher magnification (Figure3, panels b and d) show the zoom-in view of typical rhombohedra. The single crystalline nature of rhombohedra was confirmed by the SAED pattern with all the sharp diffraction spots assigned to α-Fe_2O_3 for S150 (Figure 4-1-5b).[78-80] The diffraction spots can be

attributed to $(1\bar{1}2)$, (101) , (110) planes and/or their equivalent planes under the incident electron beam along the $[\bar{1}10]$ direction. The corresponding illustration for this rhombohedron and its orientation were shown as inset in Figure 4-1-5b. The single crystalline nature for S200 was also confirmed by perfect diffraction spots (inset of Figure 4-1-5d). Two hexagons in Figure 4-1-5c highlighted by white lines to illustrate their 3D rhombohedral structure were further analyzed. The angle of 115.5° measured for the rhombohedra sketched in Figure 4-1-5c is close to the angle of 115.2° between (104) and $(0\bar{1}4)$ crystal planes.[80] Combining the TEM observation and the SAED patterns, it is concluded that the α-Fe_2O_3 rhombohedral particles were nearly 100% enclosed by six {104} facets.

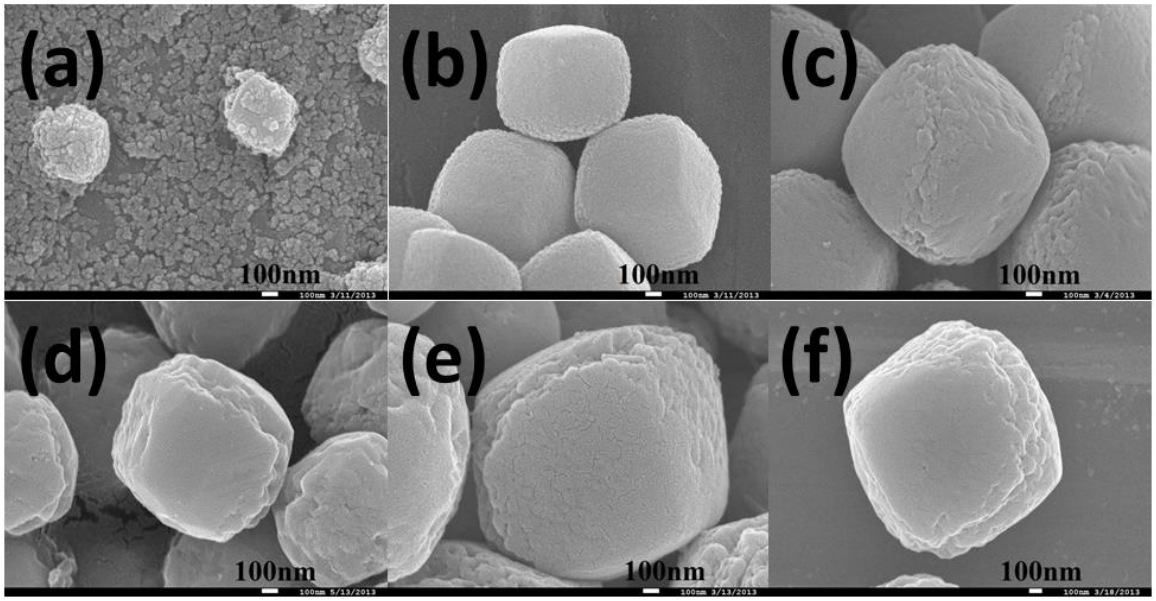

Fig. 4-1-6. Effect of reaction time: FESEM images of α-Fe_2O_3 rhombohedra prepared with reaction time of a) 20min, b) 40min, c) 75min, d) 3h, e) 24h and f) 48h at 200°C.

To investigate the formation mechanism, a set of experiments with different reaction times were carried out. The asprepared samples were studied by ex situ FESEM characterization, as shown in Figure 4-1-6. FESEM images of the materials obtained at different reaction times clearly reveal the growth and evolution from nanoparticles to solid rhombohedra (Figure 4-1-6, a and b).

Nanoparticles around 40 nm and rhombohedra around 250 nm in size with surfaces covered by nanoparticles were observed after 20 min of reaction (Figure 4-1-6a), indicating the initial stage of nucleation, aggregation and formation of small rhombohedra. When the reaction time was prolonged to 40 min, the rhombohedra grew larger to around 800 nm (Figure 4-1-6b). The rhombohedra also grow larger with further increase of time, from 75 min to 2 days (Figure 4-1-6, b−f). It is interesting to note that the edges of rhombohedra were etched and cracks started to form on those edges with a 75 min or longer reaction time. The crack became deeper with prolonged reaction time (Figure 4-1-6, c−e). When the reaction time increased to 48 h, the crack did not become deeper but broader. The formation of the cracks/valley on the edge can be ascribed to different etching rates between surfaces and the edges of the rhombohedral structure.[81] During the formation of α-Fe_2O_3 through hydrolysis of $FeCl_3$ under hydrothermal conditions, both H^+ and Cl^- ions could be generated as a byproduct. The etching process preferred to take place on the edges. This is due to the fact that higher surface energy at the edges makes it is more vulnerable to ion-assisted etching attack as compared to the smooth surface with relatively less surface energy. It is interesting to highlight that the etching process has preferred edges along the diagonal axis of the rhombohedra. The idea of etching by self-generated ions could be expanded to further tailor the structure of α-Fe_2O_3, as well as other transition metal oxides. Further study is still ongoing to gain better understanding.

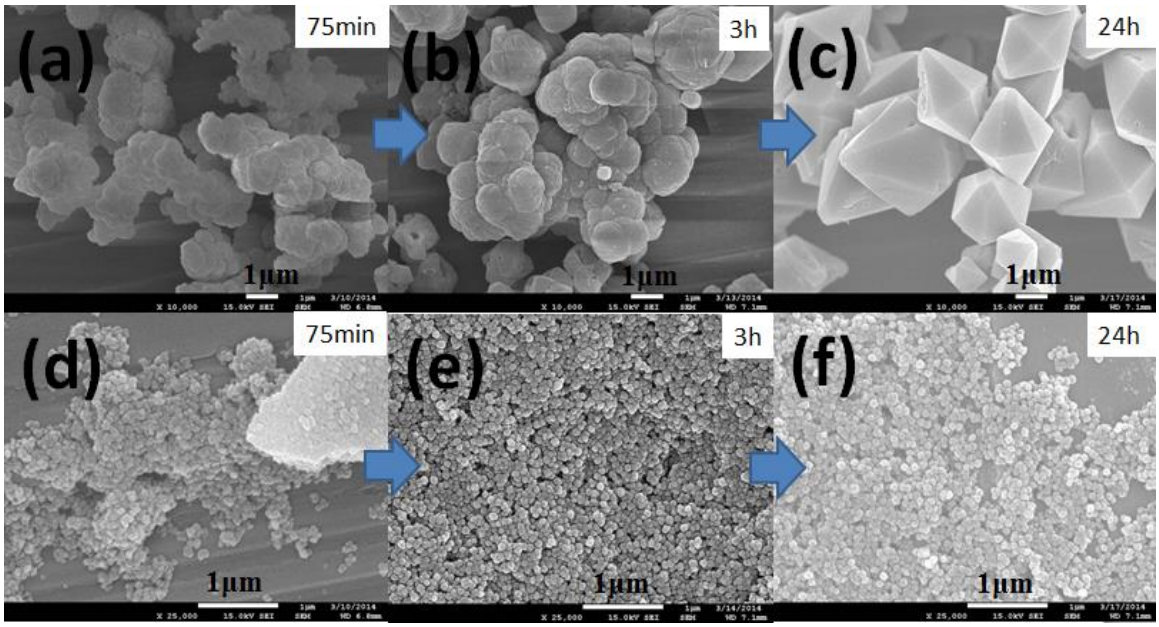

Fig. 4-1-7. FESEM images of samples prepared at 200°C using $FeF_3 \cdot 3H_2O$ with different reaction times: (a) 75min, (b) 3h, (c) 24h, nanoparticle samples prepared at 200°C using $FeBr_3$ with different reaction times: (d) 75min, (e) 3h, (f) 24h.

To demonstrate the crucial role of Cl^- played for the formation of the rhombohedral structure, $FeCl_3$ was substituted by FeF_3 and $FeBr_3$ with all other experimental conditions unchanged (Figure 4-1-7). With regard to the morphology and size of particles obtained using FeF_3 or $FeBr_3$, no rhombohedra could be obtained, which suggests the critical important role of Cl^- anions in shaping the morphology of hydrolyzed rhombohedral Fe_2O_3 particles. For samples prepared from FeF_3, aggregated nanospheres with unevenly distributed sizes were obtained after 75 min and 3 h and interesting polyhedrons in size of few micrometers were obtained after 24 h of reaction. In contrast, starting from $FeBr_3$, only nanoparticles with size around 80 nm were obtained for all three experiments with different reaction times (1.25, 3, and 24 h). The observed different morphologies could be explained by the different surface energies on different facets with terminated atoms of Cl, Br, and F under the presence of different anions.

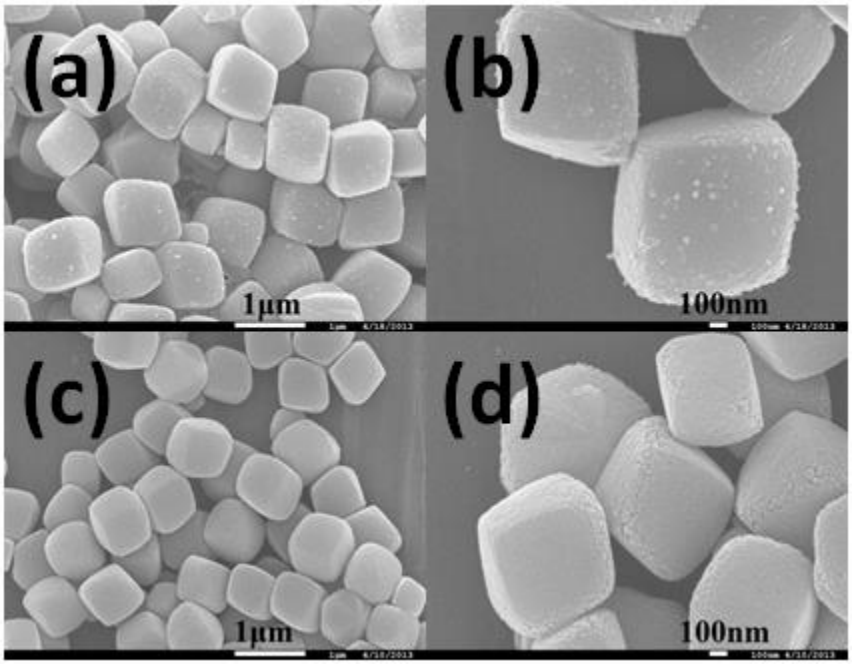

Fig. 4-1-8. Effect of reaction time: FESEM images of α-Fe_2O_3 rhombohedra prepared with reaction time of (a, b)75min and (c, d)3h at 150°C

The time-dependent experiments at 150 °C instead of 200 °C were also carried out, as shown in Figure 4-1-8. The tendency of the change in morphology was the same as those at 200 °C but at a slower rate. The nanoparticles on the surface were consumed after long reaction time (1.25 to 3 h), and the size of the monodisperse rhombohedra was maintained. The surface became smoother and a slight etching effect on the edges can be observed (Figure 4-1-8d). It was noticed that the degree of ion etching on the edges is much slower at 150 °C as compared to those at 200 °C. For example, after 75 min of reaction, no etching on the edges was observed at 150 °C (Figure 4-1-3b) versus those with significant etching on the edges along the diagonal axis of the rhombohedra at 200 °C (Figure 4-1-3d); similarly, after 3 h of reaction, minimum etching on the edges were observed at 150 °C (Figure 4-1-8) vs those large cracks caused by etching on the edges observed at 200 °C (Figure 4-1-3d). The observation agrees that a higher corrosion rate happens at a higher temperature governed by the Arrhenius equation.

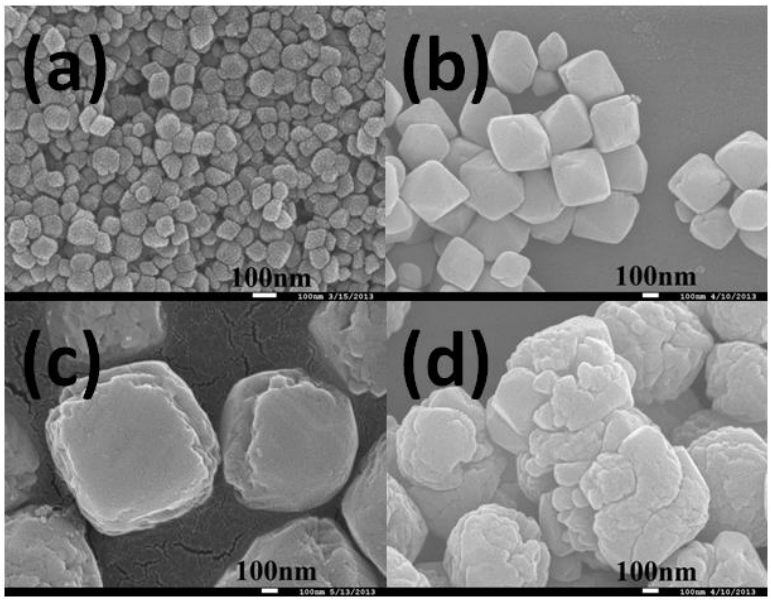

Fig. 4-1-9. Effect of solvents: FESEM images of α-Fe_2O_3 rhombohedra prepared at 200ºC with 3hrs reaction time using different volume ratio of water/1-propanol: (a) pure water, (b) 3:1, (c) 1:1, (d) 1:3. The total volume was 32ml.

The influence of the ratio of water and 1-propanol on the morphology of α-Fe_2O_3 was also investigated systematically. The morphology changes of the materials prepared with decreasing volume ratio of water to 1-propanol are shown in Figure 4-1-9 (a−d). The results show that the morphology and size of the as-prepared materials can be tuned by the ratio of solvents. The size became larger when the amount of 1-propanol increased. In Figure 4-1-9 (a, b), polyhedral structures can be observed. With 1:1 ratio of water:1-propanol, a rhombohedral structure with a valley on the edge formed, as seen in Figure 4-1-9c. When the ratio of water to 1-propanol changed to 1:3, products with irregular spherical shape are formed. We also noticed that when pure 1-propanol was used under the same conditions, no solid precipitate/product could be obtained, indicating the important role of water in hydrolysis, as expected. The results suggested that the polarity of solvent can dramatically change the morphology of those microcrystals. 1-Propanol may play a significant role at the surface of Fe^{3+} and subsequently affect the facets formed. Additional to solvent polarity, under the hydrothermal conditions, 1-propanol may also supply

alkoxy group $CH_3(CH_2)_2O^-$, which could bound coordinatively unsaturated Fe^{3+} cations on certain facets to control the morphology evolution. On the other hand, we did not observe any volume drop after each reaction inside the reactor, indicating that the amount of 1-propanol involved in the reaction is minimum, mainly at the surfaces of the solids.

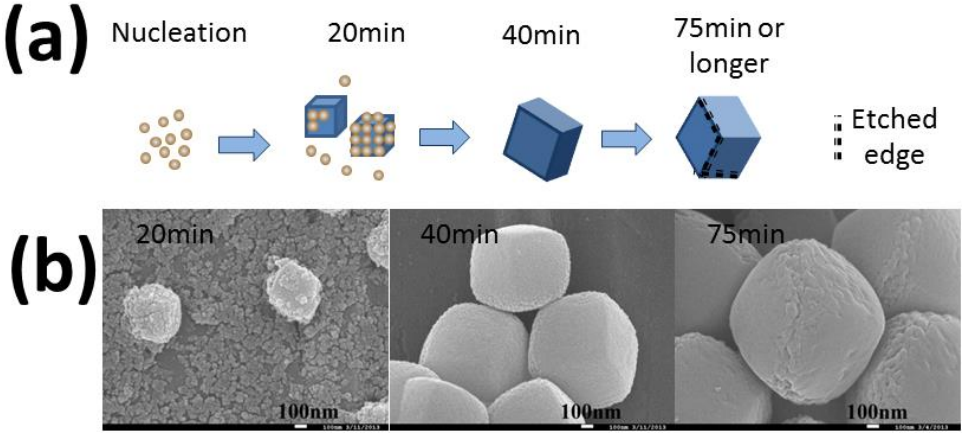

Fig. 4-1-10. (a) Illustration of the formation mechanism of solid α-Fe2O3 rhombohedra (b) corresponding FESEM images of samples at different stages.

On the basis of experimental observations, the formation mechanism was proposed, as illustrated in Figure 4-1-10a. In the early stage of the reaction, the nanoparticles are generated through the hydrolysis of Fe^{3+} in the presence of water. At the same time, the hydrolysis is controlled by the presence of 1-propanol, which can significantly affect the polarity of the formulated solvent and supply the alkoxy group $CH_3(CH_2)_2O^-$, which could bind coordinatively unsaturated Fe^{3+} cations on certain facets to guide the crystal growth. With an increase in reaction time (20 min), the small rhombohedra start to form through the aggregation of the nanoparticles. This is supported by observation of smaller rhombohedra with surfaces covered by nanoparticles (Figure 4-1-10b). The small rhombohedra grow to a larger size by the Ostwald ripening mechanism, where the attached smaller nanoparticles are dissolved and deposited on the surfaces of the bigger rhombohedra (40 min in Figure 4-1-10b). With 75 min or even longer reaction time, the

crack/valley on the edge forms due to ion etching effects on the edges (75 min, Figure 4-1-10b). The detailed formation mechanism, especially the preferred etching edges along the diagonal axis of the rhombohedra, is still under investigation by our group.

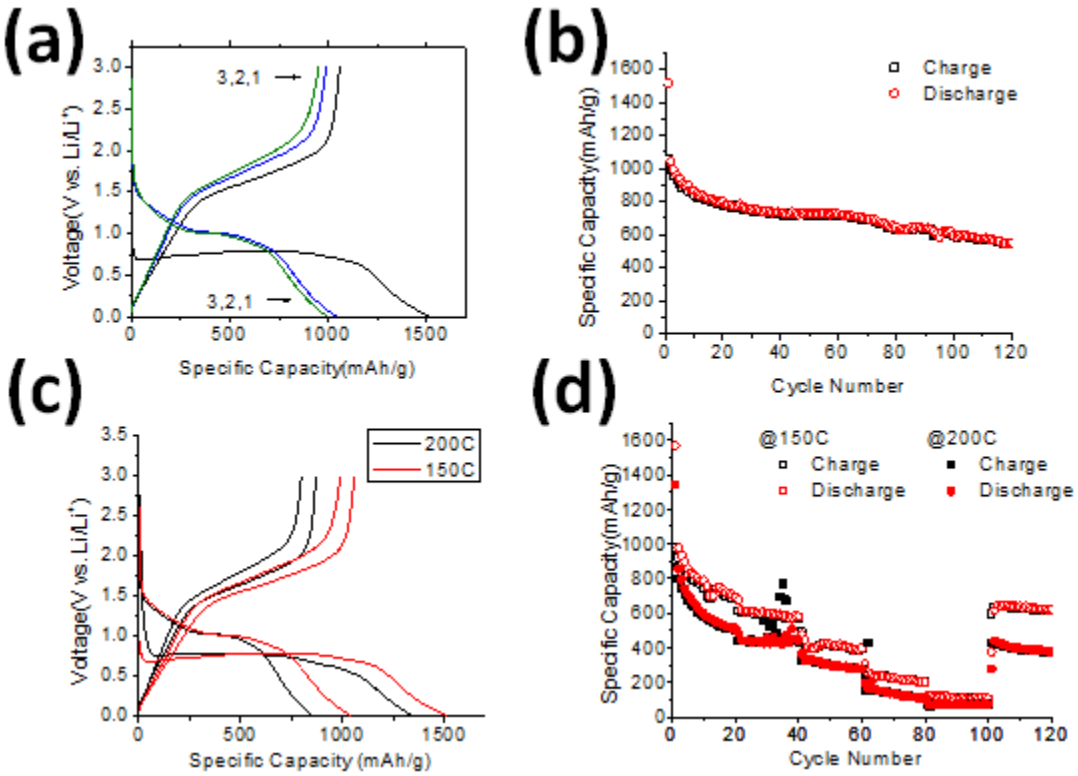

Fig. 4-1-11. (a) First 3 cycles of charge-discharge profiles; (b) Capacity vs. cycle number plots for S150 at C/5 rate; (c) Charge-discharge profiles at C/10 for S150(red) and S200(black). (d) Rate performance for S150 and S200.

Hematite α-Fe_2O_3 has been considered as a promising candidate for carbon-alternative anode materials for lithium ion batteries due to the higher theoretical capacity of 1007 mAh/g than that of graphite at 372 mAh/g. Conversion-based lithium storage in hematite is different from intercalation-based lithium storage in graphite. The electrochemical performance of asprepared materials as anode materials for LIBs was evaluated in Swagelok-type cells, and the results are shown in Figure 4-1-11. Figure 4-1-11a shows the representative charge−discharge voltage profile of the S150 at a rate of C/5 (1C = 1000 mA g^{-1}) for the first three cycles. The initial discharge

(lithiation) and charge (delithiation) capacities are 1514 and 1057 mAh/g, respectively. The irreversible capacity loss of 457 mA h g^{-1} (30.1%) of the first cycle can be attributed to the electrochemical reduction of Fe_2O_3 and decomposition of the electrolyte and formation of the solid electrolyte interphase (SEI). The typical electrochemical reactions involved were proposed in previous works:[18,29]

$$Fe_2O_3 + 2Li^+ + 2e^- \Rightarrow Li_2(Fe_2O_3) \quad (1)$$

$$Li_2(Fe_2O_3) + 4Li^+ + 4e^- \Rightarrow 2Fe^0 + 3Li_2O \quad (2)$$

$$2Fe^0 + 2Li_2O \leftrightharpoons 2Fe^{II}O + 4Li^+ + 4e^- \quad (3)$$

The first voltage plateau around 1.2 V attributing to the reaction in eq 1 represents the intercalation of Li^+ into nanostructured α-Fe_2O_3 and the formation of $Li_2(Fe_2O_3)$ is very weak here (Figure 4-1-11a), which was also observed in earlier studies.[19,81] On the other hand, the second voltage plateau at ~0.75 V is dominant, contributing a capacity of 1250 mAh/g, which can be assigned to the reduction of Fe ions to nanoscale Fe^0 metal and the formation of Li_2O, represented by eq 2. The voltage drop from below 0.75 to 0.01 V could be attributed to the formation of a SEI and decomposition of the solvent in the electrolyte.[20] The similar charge−discharge curves for subsequent cycles suggest that electrochemical reactions involved are the same from second cycle onward and the electrochemical reactions are highly reversible. The improved cyclability was demonstrated at a rate of 200 mA g^{-1} over 120 cycles (Figure 4-1-11b). The discharge capacity was maintained at 550.5 mAh g^{-1} after 120 cycles, with average Coulombic efficiency of 99% from the 2nd cycle to the 120th cycle. The as-prepared α-Fe_2O_3 rhombohedra demonstrated significantly improved cycling performance and specific capacity, as compared to micrometric α-Fe_2O_3, which faded to negligible capacity within 10 cycles,[20] α- Fe_2O_3 microcubes which faded to below 200 mA h g^{-1} after 10 cycles,[23] solid microparticles which had 340 mA h g^{-1} specific

capacity after 100 cycles,[29] or even hollow microcubes which had 460 mA h g^{-1} Fe_2O_3 specific capacity after 100 cycles.[81] The capacity of 550.5 mA h g^{-1} Fe_2O_3 after the 120-cycle test was still 50% higher than the theoretical capacity of the commercial graphite-based anode.

The rate performances of both S150 and S200 were evaluated by charge−discharge of the battery cells at different current density from C/10, C/5, C/2, C, 1.5C, and then back to C/10 for a 20 cycle interval each (Figure 4-1-11d). The specific capacity of S150 is higher at all rates as compared to that of S200. After testing for 120 cycles, specific capacity for S150 and S200 are around 600 and 400 mAh/g, respectively. The superior performance of S150 as compared to S200 could be attributed to smaller size and higher utility of the active materials in reversible lithium-ion storage. The charge-discharge profiles of S150 at the 2nd, 22nd, 42nd, 62nd, 82nd, and 102nd cycles (at rates of C/10, C/5, C/2, C, 1.5C, and C/10, respectively) are plotted in Figure 4-1-11c. Specific capacity of 978, 618, 444, 256, 127, and 617 mA h/g are achieved at the corresponding cycle. It is interesting to note that the specific capacity returns back to a value of 617 from 127 mA h/g when the rate is resumed to C/10 from 1.5C (Figure 4-1-11c, profile in dotted lines). The results suggest that the electrode materials can sustain the extensive cycling at high rates, which is highly desirable.

In summary, a facile fast hydrothermal method for the preparation of microsized α-Fe_2O_3 rhombohedra with nearly 100% exposed {104} facets was developed. The hydrothermal reaction time could be as short as 75 min, in contrast to typical hydrothermal reactions over a few days. It was observed that the polarity of the as-formulated solvents of water and propanol and reaction temperature have significant impact on the morphology of the products. The preferred etching edges along the diagonal axis of the microsize rhombohedra by the self-generated ions was observed, which could further tailor the structure and be potentially extended to other transition

metal oxides. The formation mechanism was revealed by ex situ FESEM observations of the samples prepared at different reaction times. Electrochemical performance has been tested by galvanostatic discharge−charge cycling. Improved electrochemical performances in terms of cyclability and specific capacity were achieved. The specific capacity was maintained at 550 mAh/g after 120 cycles at a rate of 200 mA/g under the cyclic test and at 617 mAh/g after the rate was reassumed from 1500 to 100 mA/g under the rate performance test. Experimental evidence clearly shows that the as-designed solid microsized α-Fe_2O_3 can effectively and reversibly store lithium ions with performances comparable to nanosized α-Fe_2O_3.

4.2 α-Fe_2O_3 void@frame microframes

Engineering microparticles into unique hollow structures to tune morphology-dependent physiochemical properties has been attracting much attention recently. Engineered hollow microstructures can find many important applications, including energy storage,[82] drug delivery,[83] catalysts,[84,85] photovoltaic and environmental remediation.[86,87] Various synthetic strategies have been developed to prepare hollow structures. For example, chemical etching,[88-90] the Ostwald ripening process,[91,92]Kirkendall effect,[93,94] galvanic replacement,[95] template-assisted methods, etc.[82,96] are frequently employed to make hollow structures with different chemical compositions, including metals, metal oxides and chalcogenides. Most of the hollow structures obtained have interior cavities completely enclosed by shells or as void@shell closed structures.[82-92] Different from the void@shell closed structures, the frame-like structures or void@frame are relatively less studied.[97-99] Void@frame structures have more open space and exposed surface as compared to the void@shell or solid structures. The void@frame structures may offer advantages as compared to void@shell and solid structures in certain applications. For example, the extra space and open structure may be beneficial for reversible storage of lithium and sodium ions in

rechargeable batteries.[100,101] The schematic in Fig. 4-2-1 illustrates the advantages of void@frame structures in ion storage, as compared to solid and hollow particles. The open frames offer micro-channels for electrolyte migration and shorten the length of ion diffusion. The open frames could offer more active ion accessible sites for fast charging. The void@frame structure can also accommodate the strains and stress upon repeated ion cycling. It is still very challenging to facilely prepare void@frame structures, in contrast to that there are a large number of reports on void@shell structures. [82,92,102] There are increasing efforts to prepare void@frame structures, but only a limited number of materials have been explored. For example, multimetallic Pt_3Ni nanoframes with 3-D electrocatalytic surfaces have been prepared by interior erosion of polyhedral precursors to enhance catalytic properties;[99] octahedral Au–Ag nanoframes have been prepared by the galvanic replacement reaction to improve catalytic properties as compared to Au–Ag nanoparticles;[98] hollow Fe^0 nanoframes have been prepared by Na based molten salt corrosion of Fe nanoparticles; [103] Cu_2O–Au nanoframes have been prepared by hydrolysis deposition to coat a cupric hydroxide layer (precursor of Cu_2O) on Au nanoframes followed by reduction of cupric hydroxide by hydrazine hydrate and heat treatment to tune the photocatalytic properties;[104] Cu_2O nanoframes have been prepared by selective oxidative etching of Cu_2O truncated octahedra;[105] Cu_2O truncated rhombic dodecahedral nanoframes have been prepared by particle aggregation and acid etching.[97] It is always intellectually interesting and technically rewarding to develop new methods to prepare single crystalline void@frame structures, particularly, those highly functional materials that have rarely been explored, such as iron oxides.

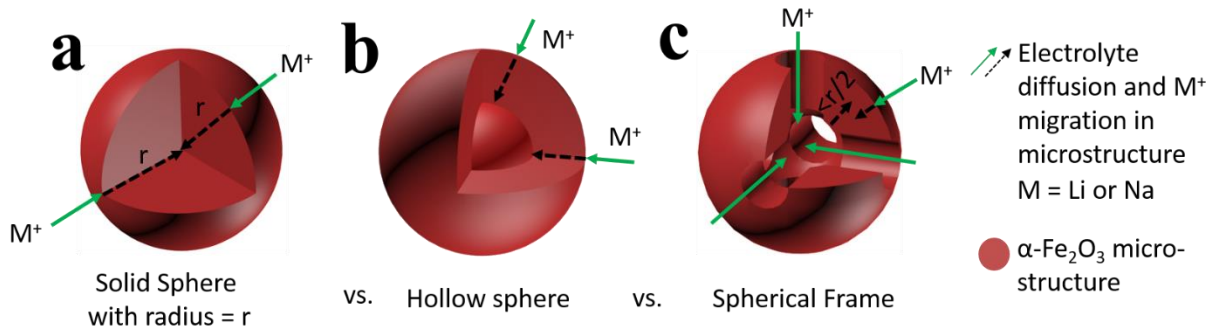

Fig. 4-2-1. Schematics (cutaway-view) illustrating the advantages and difference of (c) void@frame particles as compared to (a) solid particles and (b) void@shell hollow particles in facilitating the electrolyte penetration and ion diffusion and migrations.

Iron oxides are abundant, cheap, environmentally benign, and non-toxic. Iron oxides can find many applications.[106-109] For example, Fe_2O_3 materials are promising negative electrode materials for reversible energy storage with a theoretical capacity of 1007 mA h g^{-1} for both lithium-ion and sodium-ion batteries, assuming the formation of Fe^0 according to equation: $Fe_2O_3 + 6\ M^+ \rightarrow 2Fe^0 + 3M_2O$, where M =Li or Na.[110,111] Although closed void@shell structures of iron oxides, such as hollow spheres, [29,112,113]cubes, [81,114]and cocoons, [115] as well as cage-like open structures, have been reported.[116,117] single crystalline α-Fe_2O_3 void@frame open microframes have not been reported yet, based on the best of our knowledge.

Herein, we report the design and synthesis of single-crystalline α-Fe_2O_3 void@frame microframes with multiple pores on the frames encapsulating the voids by annealing induced discontinuous grain growth and crystallization. There are two steps. First, porous α-Fe_2O_3 chevron microbeads with tunnels and aggregated nanoparticle building units were synthesized by a solvothermal method as precursors.[118] Followed by annealing, the precursors were transformed into single-crystalline α-Fe_2O_3 void@frame microframes via a discontinuous grain growth mechanism. The structures of the as-synthesized single-crystalline α-Fe_2O_3 microframes were thoroughly characterized. The single-crystalline α-Fe_2O_3 microframes were demonstrated to be

potential negative electrode materials for both lithium-ion batteries (LIBs) and sodium-ion batteries (SIBs). An excellent specific capacity of 700 mA h g^{-1} for 550 cycles was achieved for LIBs. The electrode of pure α-Fe_2O_3 microframes without any additives (no binder or conductivity enhancer) also demonstrated reasonable performances in SIBs without optimization.

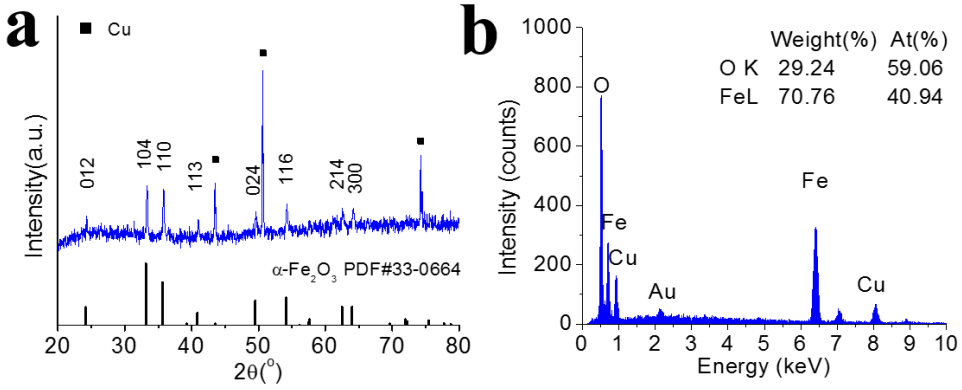

Fig. 4-2-2. The as-prepared single-crystalline α-Fe2O3 microframes characterized by: (a) XRD with all the peaks assigned to crystalline α-Fe2O3. Peaks of Cu were from the Cu foil. (b) EDS with an Fe: O ratio close to 2 : 3. Peaks of Cu and Au were from the Cu background and Au sputter coating.

The crystallographic structure and phase purity of the asprepared single-crystalline α-Fe_2O_3 microframes were revealed by XRD (Fig. 4-2-2a). All the diffraction peaks can be assigned to crystalline α-Fe_2O_3 (JCPDS card no. 33-0664). The crystallite size based on (104) diffraction was estimated to be about 68 nm using the Scherrer equation. As compared to the precursor,[118] the crystallite size was dramatically increased from 19 nm to 68 nm. The increase in the crystallite size by annealing is well documented.[119-121] The annealing induced particle growth and crystallization could be attributed to the interfacial reaction during calcination leading to growth of crystalline grains.[116,120,122] The EDS analysis clearly demonstrated the dominant presence of both elements of Fe and O with an atomic ratio of Fe to O at around 2 : 3 agreeing with the molecular formula of Fe_2O_3 (Fig. 4-2-2b). Therefore, based on XRD and EDS results, crystalline α-Fe_2O_3 was successfully obtained.

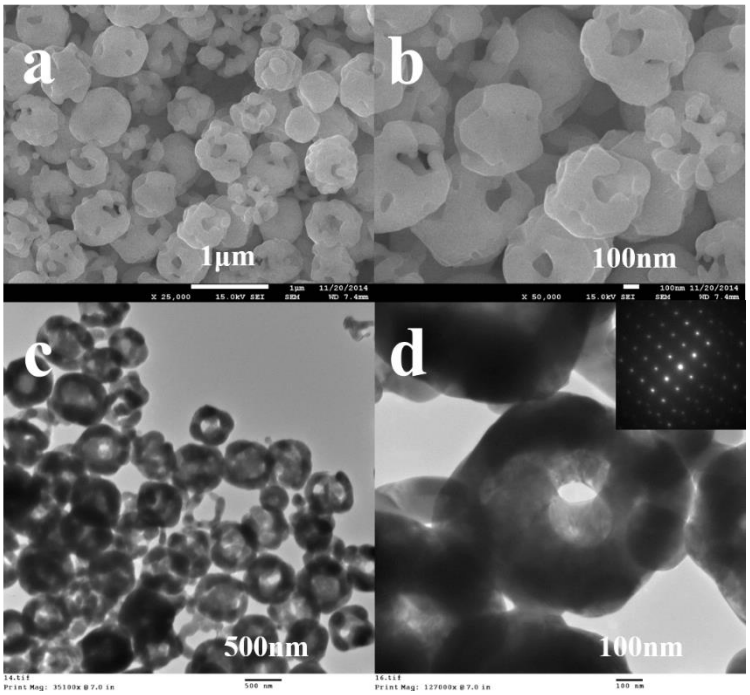

Fig. 4-2-3. Single-crystalline α-Fe2O3 microframes characterized by: FESEM images of (a) low-magnification overall view and (b) magnified view of a few representative microframes showing the details of perforated hollow structures; TEM images of (c) low-magnification overall view showing a void@frame structure in each particle and (d) zoom-in view of a typical microframe clearly showing the perforated shell and the enclosed cavity. Inset of (d) is the SAED pattern indicating that it is single crystalline.

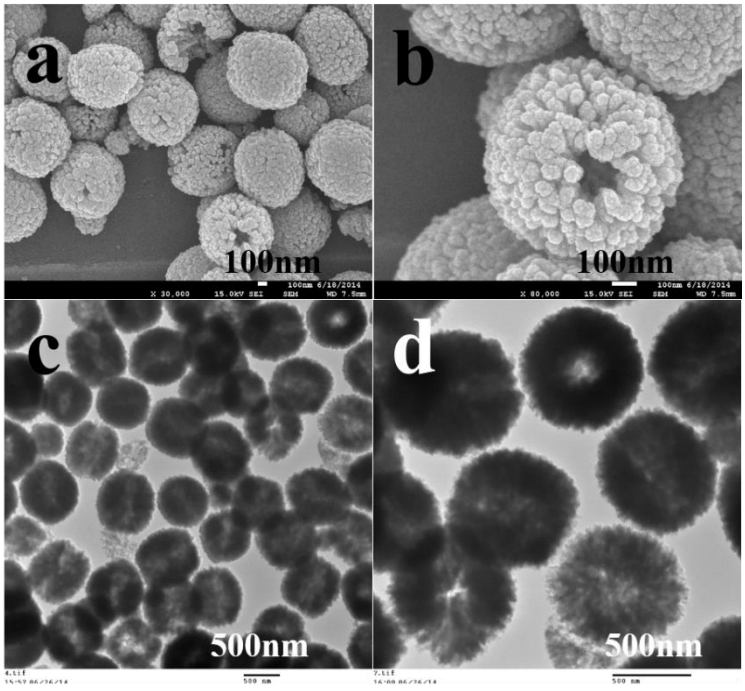

Fig. 4-2-4. The α-Fe_2O_3 precursor used in this work: (a) Low-magnification FESEM image shows dozens of α-Fe_2O_3 microbeads with pore; (b) magnified FESEM image of a typical α-Fe_2O_3 microbead showing the detailed structure and texture; (c) Low-magnification TEM image shows dozens of α-Fe_2O_3 microbeads, and (d) magnified TEM image of a few representative α-Fe_2O_3 microbeads.

The morphology of the as-prepared single-crystalline α-Fe_2O_3 microframes was thoroughly characterized by FESEM and TEM (Fig. 4-2-3). The low-magnification FESEM image shows that all the particles are in the microscale with a size of around 400–700 nm and each particle has open frame-like structures or with perforated shells (Fig. 4-2-3a). There are multiple holes on the shells forming frame-like structures. A magnified FESEM image shows the smooth texture of the surface of the microframes, in sharp contrast to the rough texture observed in the precursor formed by nanoparticle aggregates (Fig. 4-2-4). The smooth texture suggests their single-crystalline nature (Fig.4-2-3b). More details about the structure of the microframes were further revealed by TEM. The low-magnification TEM image shows that all the particles have a ring-like TEM projection with nonuniform contrast distribution along the rings. The observation reveals that in each particle there is an interior void and multiple holes on the shell, forming the void@frame structures (Fig. 4-2-3c). The magnified TEM image of a typical microframe clearly shows the unique void@frame open structure and perforated shell (Fig. 4-2-3d). The SAED patterns with sharp diffraction spots assigned to α-Fe_2O_3 suggest that the microframes are single-crystalline (inset of Fig. 4-2-3d).

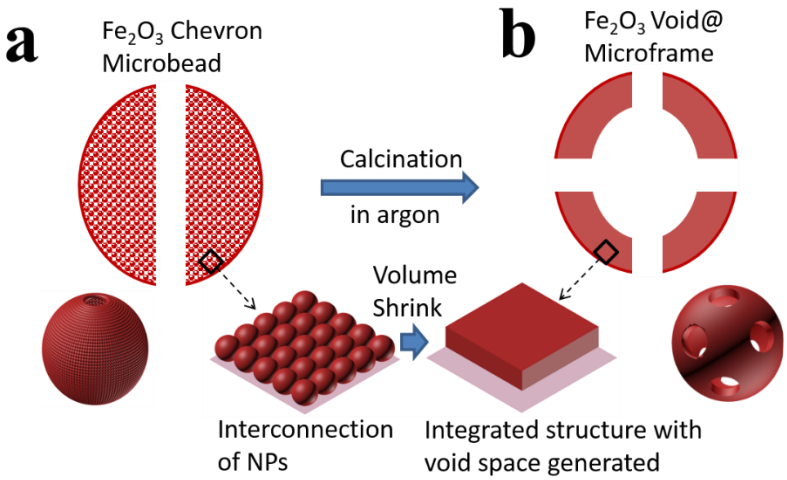

Fig. 4-2-5. Schematic of the plausible mechanism in the formation of (b) single-crystalline α-Fe_2O_3 microframes from (a) chevron microbeads of aggregated nanoparticles as building units with a tunnel.

The plausible formation mechanism of the single-crystalline α-Fe_2O_3 void@frame microparticles is illustrated in Fig. 4-2-5. The porous chevron microbeads with tunnel-like holes as the precursor were formed with aggregated nanoparticles as the building units (Fig. 4-2-4 in the ESI†). Therefore, during the high temperature annealing process, the aggregated nanoparticles in the precursor (Fig. 4-2-5a) tend to grow larger and form an integrated crystalline structure (Fig. 4-2-5b). The annealing induced particle growth could be attributed to the grain boundary diffusion mechanism, leading to the conversion from polycrystalline to single crystalline particles.[117,119,120] At the same time, the surface –OH groups or defects may also contribute to the reconstruction of crystallites via discontinuous grain growth.[116,123,124] As a result, both voids and perforated shells were generated, forming a void@frame microframe (Fig. 4-2-5b). Additional studies, such as in situ TEM, are still required to better understand the formation mechanism.

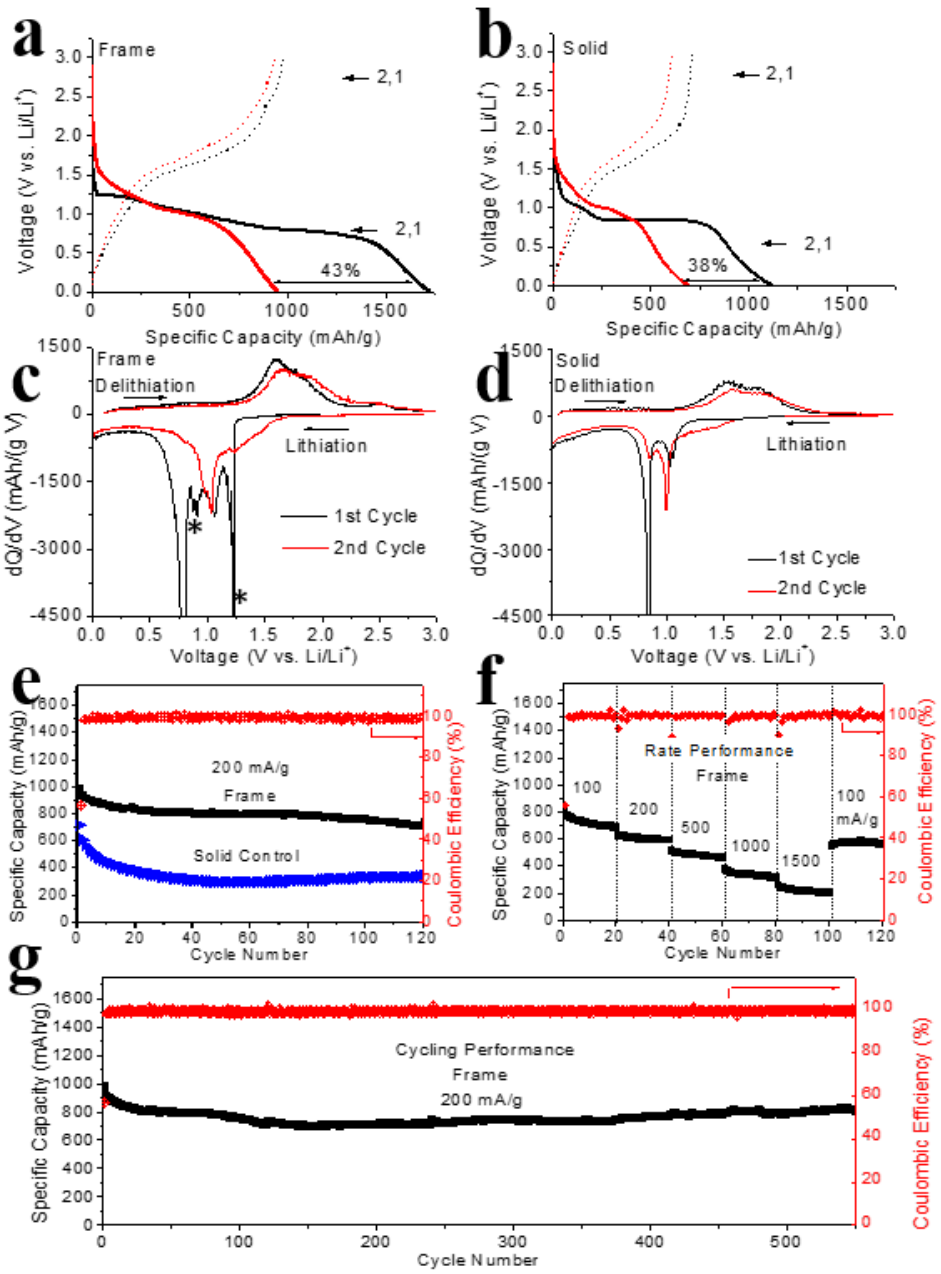

Fig. 4-2-6. Electrochemical performances of single-crystalline α-Fe_2O_3 microframes and solid microparticles: first two-cycle charge–discharge profiles of (a) microframes and (b) solid microparticles; dQ/dV vs. V plots of (c) microframes and (d) solid microparticles; (e) comparison of cycling performance between microframes and solid microparticles at a current of 200 mA g^{-1}; (f) rate performance at various testing currents from 100 to 1500 mA g^{-1}; (g) long cycle life of the additive-free electrode based on single-crystalline α-Fe_2O_3 microframes.

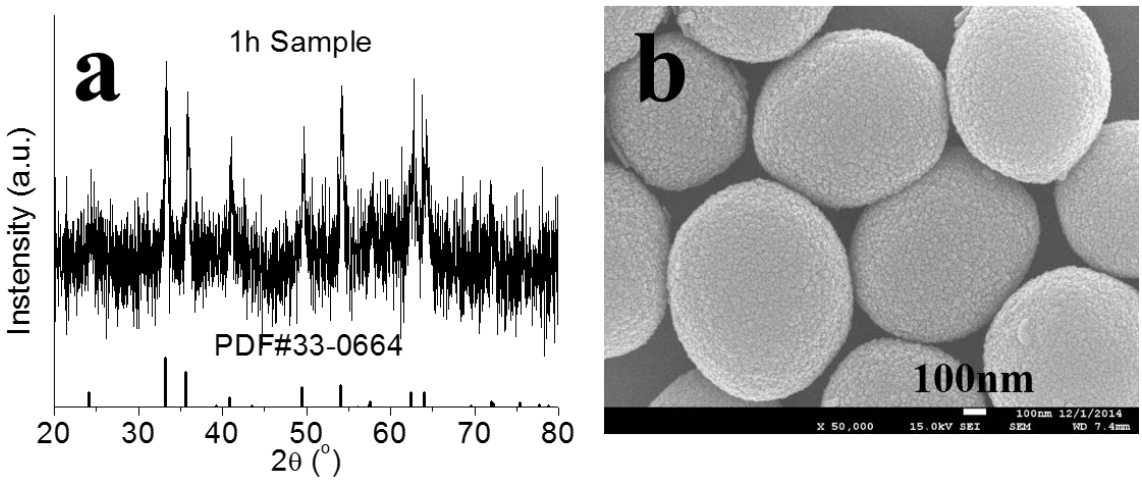

Fig. 4-2-7. (a) XRD and (b) FESEM image of α-Fe_2O_3 microstructure solid control for LIB cycling test for comparison.

Lithium-ion batteries have been attracting much attention recently.[125-127] Electrochemical tests are carried out to evaluate the potential application of the as-prepared single-crystalline α-Fe_2O_3 microframes in lithium-ion batteries (Fig. 4-2-6). The first two cycles of charge–discharge profiles are consistent with those of α-Fe_2O_3 materials reported.[20,30] The initial discharge (lithiation) and charge (de-lithiation) capacities are 1719 and 975 mA h g^{-1}, respectively. The low initial coulombic efficiency of 57% can be attributed to the irreversible reactions that take place in the first cycle, including the formation of a solid-electrolyte interphase (SEI) associated with the decomposition of the electrolyte and ion trapping.[30] The differential capacity vs. voltage (dQ/dV vs. V) plots of the first two cycles are shown in Fig. 4-2-6c. Two cathodic peaks at around 1.1 V and 0.8 V in the first discharge process can be assigned to the formation of $Li_{0.6}(Fe_2O_3)$ and $Li_{1.8}(Fe_2O_3)$, respectively.[20,30,128] Compared to solid Fe_2O_3 microspheres (Fig. 4-2-6d), there are two additional peaks at around 0.9 and 1.25 V observed for the microframes (Fig. 4-2-6c). The two additional peaks could be assigned to the insertion of Li into CuO.[129] A trace amount of CuO could be formed on the surface of the Cu current collector at high temperature. The trace amount of CuO could also

contribute to the large first cycle irreversible capacity loss. The broad anodic peak at 1.7 V in the charging process, which is observed for both samples (Fig. 4-2-6c and d), can be assigned to the de-intercalation of Li and the oxidation of Fe^0.[130,131]

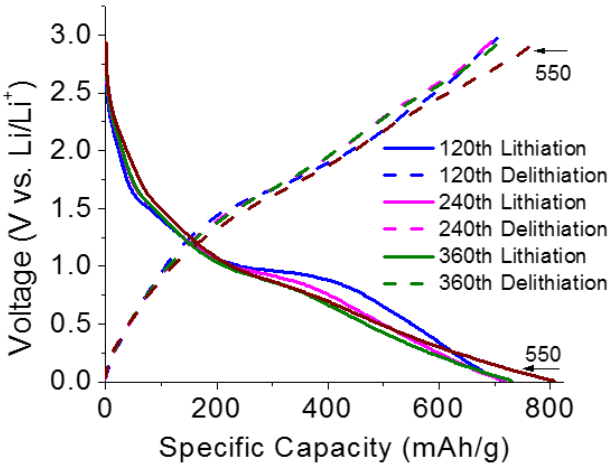

Fig. 4-2-8. Charge-discharge profiles of the 120th , 240th , 360th and 550th cycles under cycling test at 200 mA/g, indicating the same electrochemical reactions involved and high reversibility.

The plot of capacity vs. number of cycles of α-Fe_2O_3 solid microspheres (characterization shown in Fig. 4-2-7) as the negative electrode is shown in Fig. 4-2-6e (blue triangle). In comparison, the single-crystalline α-Fe_2O_3 microframes show significant improvement in both capacity retention and high reversible specific capacity (Fig. 4-2-6e). The improvement might be attributed to the easy accessibility of electrolyte/ions to open microframes and the structural stability of the void@frame structure during the discharge/charge process. The rate performance of the micro-frames was also evaluated (Fig. 4-2-6f). The specific capacities of 718, 601, 485, 335, 214, and 574 mA h g^{-1} were achieved at testing currents of 100, 200, 500, 1000, 1500, and 100 mA g^{-1} with 20 cycle intervals, respectively. The capacity was relatively stable at high currents with excellent coulombic efficiency. It should be noted that the loading density of the electrode (Fig. 4-2-6e) was 1.9 mg cm^{-2} and the loading density of the electrode (Fig. 4-2-6f) was 3.8 mg cm^{-2}. In

other words, the thickness of the two electrodes has a two-time difference. In other words, the thickness of electrodes could significantly affect the lithium storage capacity, which could be attributed to the poor conductivity of the α-Fe_2O_3-only electrodes. The long cycle life of the as-prepared single-crystalline α-Fe_2O_3 microframe negative electrode was evaluated over 550 cycles (Fig. 4-2-6g). The charge–discharge profiles of the 120th, 240th, 360th and 550th cycle are almost identical, indicating the same reversible reactions involved and good electrode stability (Fig. 4-2-8). The coulombic efficiency was maintained at 99% from the 2nd cycle. These results indicate excellent cycling performance of single-crystalline α-Fe_2O_3 microframes. In contrast, commercial microscale Fe_2O_3 particles suffer significant capacity fading within the first 10 cycles.[132]

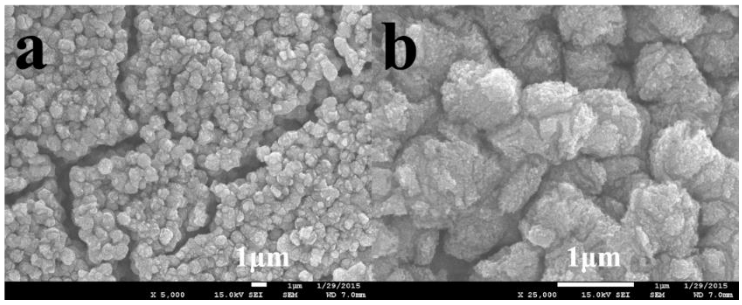

Fig. 4-2-9. (a) Low magnification and (b) magnified FESEM images for α-Fe_2O_3 microframes anode after 120-cycle rate test in LIB. The outline of the microstructures was maintained after repeated charge-discharge processes.

The structure of the materials after 120 cycles and tested under various rates was revealed by the FESEM images (Fig. 4-2-9). A large amount of microstructures with a size of around 600 nm was observed as shown in the low-magnification FESEM image (Fig. 4-2-9a) and magnified FESEM image (Fig. 4-2-9b). Although the void@frame structures were generally destroyed under electrochemical pulverization, the outline of the microparticles can still be observed which is similar to the microframes before cycling. The observation suggests that the unique structure of the single crystalline void@frame microframes could accommodate the volume expansion inside the outline of the microframes, leading to stable electrodes. However, we believe that the

performance could be further optimized by introducing additives into the electrode and electrolyte, including carbon coating, decorating with carbon or metallic nanoparticles, and adding fluoroethylene carbonate to the electrolyte.

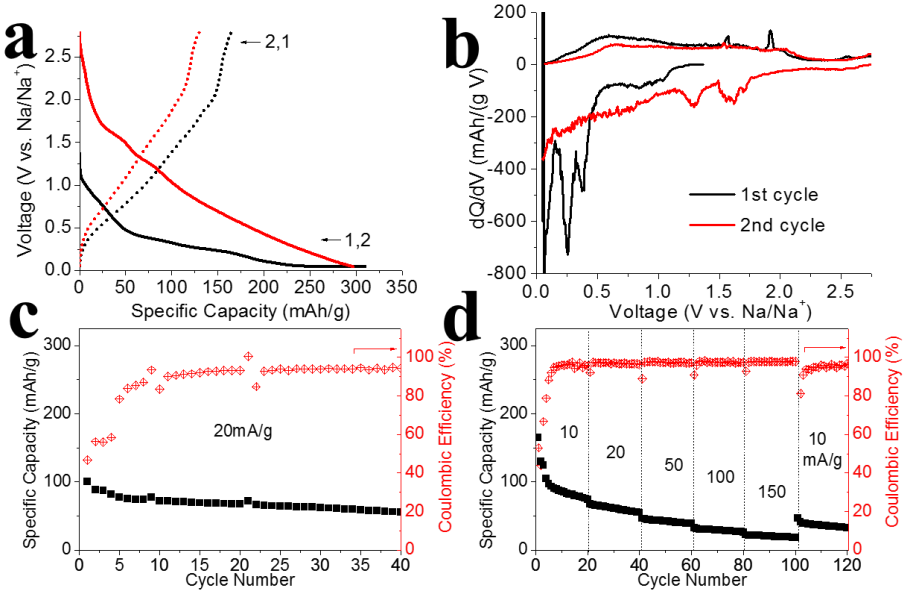

Fig. 4-2-10. Electrochemical performances of additive-free electrodes prepared by the CAP method based on the as-synthesized single-crystalline α-Fe_2O_3 microframes in SIBs: (a) charge-discharge profiles of the first two cycles and (b) dQ/dV plots of the first two cycles at a current of 10 mA g^{-1}; (c) cycling performance at a current of 20 mA g^{-1} and (d) rate performance at currents from 10 to 150 mA g^{-1}.

Additionally, the single-crystalline α-Fe_2O_3 microframes were also evaluated as negative electrode materials for SIBs (Fig. 4-2-10). The reversible sodium storage in α-Fe_2O_3 has been attracting much attention in recent years.[110,111,133-137] The first reversible storage of sodium in α-Fe_2O_3 nanoparticles was reported by Komaba et al. in 2009.[133] Another study of reversible sodium storage in a mixture of g- and α-Fe_2O_3 as negative electrode materials was reported by M. Valvo et al.[111] Typically, additives, including binders and conductivity enhancers (like carbon black which is active for Na storage[138]), or other carbonbased active materials (e.g. reduced graphene oxide[134] or graphene nanosheet[137]), were used in the preparation of iron oxide based electrodes for SIBs.

However, in our case, the electrodes were prepared by the CAP method,[119] without the use of any binder or conductivity enhancer. In the first sodiation process, a slope in the charge–discharge curve starts at 0.5 V (Fig. 4-2-10a) which could be attributed to the SEI formation and insertion of Na into Fe_2O_3, forming $Na_xFe_2O_3$. The broad cathodic peak at 1.0 V may be attributed to the early stage of Fe_2O_3 reduction and related structural changes.[64] The reversible specific capacity was 55 mA h g^{-1}, with the coulombic efficiency gradually increasing from 46% to 94%, probably due to the stabilization of the SEI layer on the surface of microframes.[62] As microscale materials, the electrodes of Fe_2O_3 microframes also demonstrated reasonably good rate performance (Fig. 4-2-10d). Generally, α-Fe_2O_3-based electrodes, even with carbon as the conductivity enhancer, have low reversible capacity.[134,137] It should be noted that the electrochemical performances have not been optimized yet. Therefore, we believe our single-crystalline α-Fe_2O_3 should be worthy for further investigation for SIBs

In summary, we have successfully prepared single-crystalline α-Fe_2O_3 microframes by the annealing process. The possible formation mechanism of the microframes was proposed. The potential applications of the single-crystalline α-Fe_2O_3 microframes in reversible energy storage, including both LIBs and SIBs, have been demonstrated. The α-Fe_2O_3 microframe and its additive-free electrodes demonstrated significantly better performance as compared to solid microparticles, showing an excellent cyclability with a reversible capacity of 700 mA h g^{-1} for at least 550 cycles. The improved electrochemical performances could be attributed to the high accessibility of the open microframe structure and the structural stability of the void@frame structure. Additionally, the reversible storage of sodium ions by the additive-free negative electrode of pure α-Fe_2O_3 microframes was preliminarily demonstrated. The void@frame structures may find many other

important applications, including tissue regeneration and catalysis,[139,140] and provide a unique model system for fundamental studies, which are our main focus in the next-stage of investigation.

CHAPTER 5. NANOPARTICLE ENSEMBLE

5.1 Hollow α-Fe_2O_3 nanococoons

Rechargeable lithium-ion batteries (LIBs) are currently the dominant power sources for portable electronic devices. The market of LIBs is expanding into electric vehicles and green energy grids. After 20 years of development since the first commercialization of LIBs by Sony in 1991, carbon is still exclusively used as anode materials in LIBs. However, the theoretical capacity of graphite (372 mA h g^{-1} based on LiC_6) is almost achieved, and it becomes one of the bottlenecks to further increase energy density of LIBs based on carbon. Therefore, there is an urgent need to develop carbon alternative materials with higher capacity to meet the increasing demand for energy storage. Transition metal oxides receive increasing attention as carbon-alternatives because of their much higher theoretical capacity based on a different storage mechanism of conversion and alloying.[130,141-144] In particular, α-Fe_2O_3 with a theoretical capacity of 1007 mA h g^{-1} has been attracting much attention as a promising candidate to replace carbon.[42,73,145-149]

Compared to other transition metal oxide candidates (such as NiO, CoO),[130] α-Fe_2O_3 is outstanding in terms of low cost, abundance, and environmental benignity. However, poor cyclability, a common problem among transition metal oxides, caused by a volume change during the insertion/extraction of Li ions and poor conductivity, is the main challenge. One strategy is to design and tailor α-Fe_2O_3 nanostructures to address the challenge. For example, nanostructured Fe_2O_3 in the form of nanotubes,[19] rods,[15-17] spheres,[27-29] cubes,[24,25] spindles, [26,150,151] flakes,[20] hollow structures, [21,26,33-37] and composites[109] has been synthesized for LIBs and achieved a certain degree of success. Particularly, hollow nanostructures are of great interest as the hollow space can accommodate the large volume expansion during Li insertion. [33-37] It is always practically

interesting and intellectually challenging to develop facile methods to prepare Fe_2O_3 with unique hollow nanostructures.[38,39,41,152]

In this work, a facile one-pot preparation of hollow α-Fe_2O_3 with unique cocoon-like structure was reported. The size of the hollow nanococoons are about 800 nm in length and 500 nm in diameter. Furthermore, the nanococoons are constructed by aggregation of subunits of nanoparticles about 35 nm in size. Electrochemical evaluation demonstrates that the hollow nanococoons have superior performances in lithium ion storage in terms of capacity, cyclability, and high rate. Results show that hollow nanococoons perform better than non-hollow nanococoons.

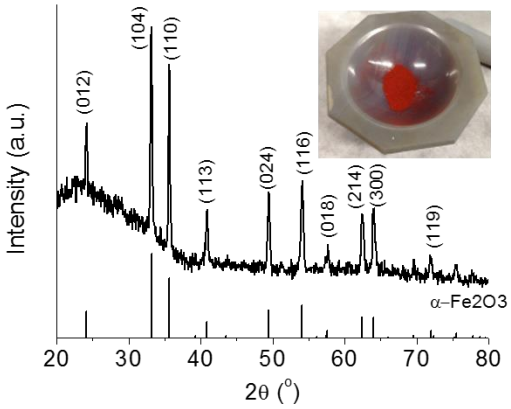

Fig. 5-1-1. XRD pattern of as-prepared hollow α-Fe_2O_3 nanococoons with building units of nanoparticles; the inset shows the optical image of the red colored α-Fe_2O_3 in a mortar.

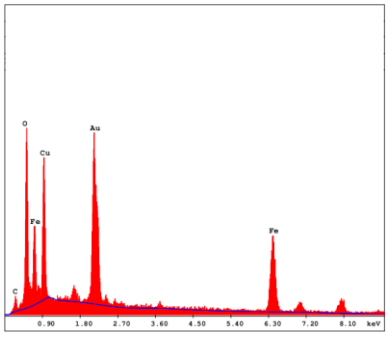

Fig.5-1-2. EDS results confirmed the chemical composition of the product is iron oxide. Au and Cu peaks are from sample coating and sample holder respectively.

The chemical composition and phase purity of the hollow nanococoons of α-Fe_2O_3 from the one-pot synthesis were confirmed by XRD (Figure 5-1-1). All the diffraction peaks can be assigned to α-Fe_2O_3 (JCPDS card no. 33-0664). No other impurities are observed. The diffraction peak (110) is used to estimate the crystalline size calculated from the Scherrer equation and it is about 34 nm. The optical color of the as-prepared powder of hollow nanococoons in a mortar (the inset of Figure 5-1-1) is the typical red color of α-Fe_2O_3.[153] The successful preparation of α-Fe_2O_3 is also confirmed by EDS (Figure 5-1-2), and the atomic ratio of Fe/O is comparable to commercial α-Fe_2O_3.

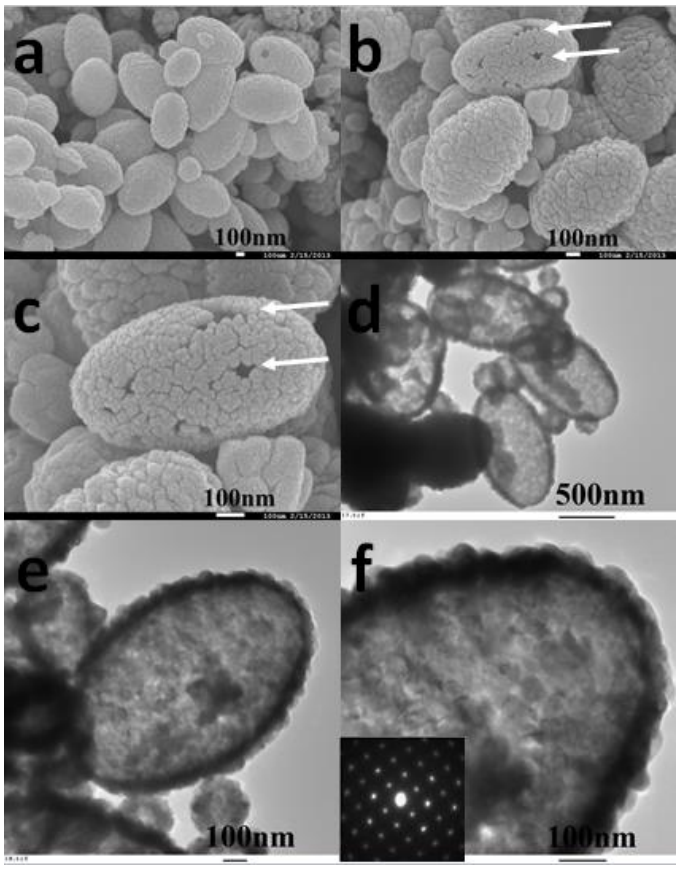

Fig. 5-1-3. FESEM images of the hollow cocoon-like nanostructures: (a) low-magnification overall view; (b) high-magnification view of a few typical nanococoons; (c) zoom-in view of a typical nanococoon with holes on the broken shell revealing its hollow structure. TEM mages of nanococoons: (d) low-magnification overall view; (e) high-magnification view of a typical nanococoon; (f) zoom-in view of a section of the nanococoon revealing the building units of nanoparticles; inset of (f) is the SAED pattern.

The morphology of the unique hollow cocoon-like nanostructures was characterized by both FESEM and TEM images (Figure 5-1-3). The low-magnification FESEM image (Figure 5-1-3a) shows that the as prepared nanoparticles are in the shape of cocoons about 800 nm in length and about 500 nm in diameter. The high-magnification FESEM image (Figure 5-1-3b) shows several typical nanococoons. The surface of the nanococoons is rough, indicating the nanococoons are formed by aggregation of subunits of α-Fe_2O_3 nanoparticles. Close examination shows that there are a few holes with size about 50 nm as highlighted by white arrows on the surface of the nanococoons (Figure 5-1-3b,c). The presence of holes indicates that the nanococoon is hollow and the shell is formed by assembly of nanoparticles at a size of about 35 nm as building subunits, close to the crystalline size estimated by XRD. The hollow structure generally observed was further confirmed by TEM (Figure 2d). The high-magnification TEM image (Figure 5-1-3e) of a typical nanococoon shows clear contrast between the shell and the interior, indicating hollow structure was formed. Furthermore, the zoom-in cross-section view of the shell (Figure 5-1-3f) reveals that the shell is not smooth and is about 75 nm in thickness, and it once again confirms the rough shell is constructed by assembled nanocrystals. The subunits are single crystalline rhombohedral phase of hematite α-Fe_2O_3 as confirmed by selected area electron diffraction (SAED) with sharp diffraction spots (inset of Figure 5-1-3f).

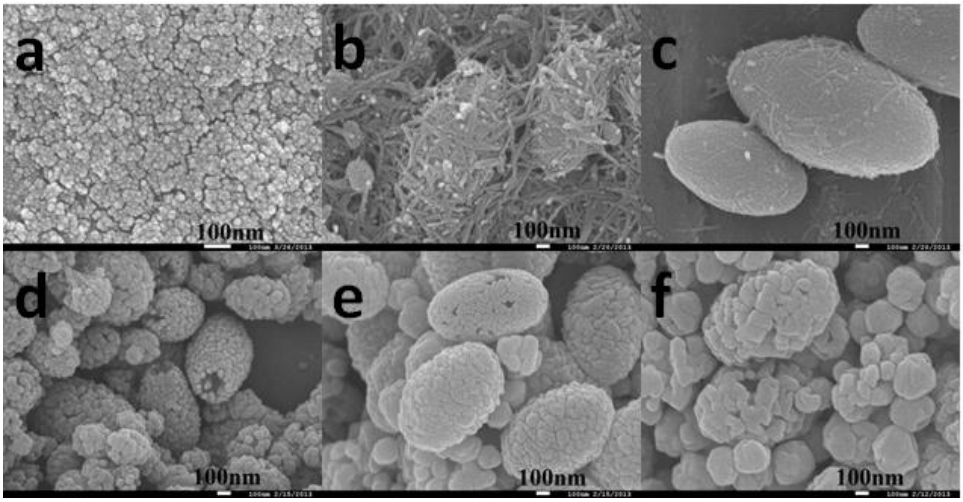

Fig. 5-1-4. Effect of reaction time: FESEM images of the products obtained after different time of reaction at (a)15 min,(b) 30 min,(c) 60 min, (d) 75 min,(e)3 h, (f)6 h.

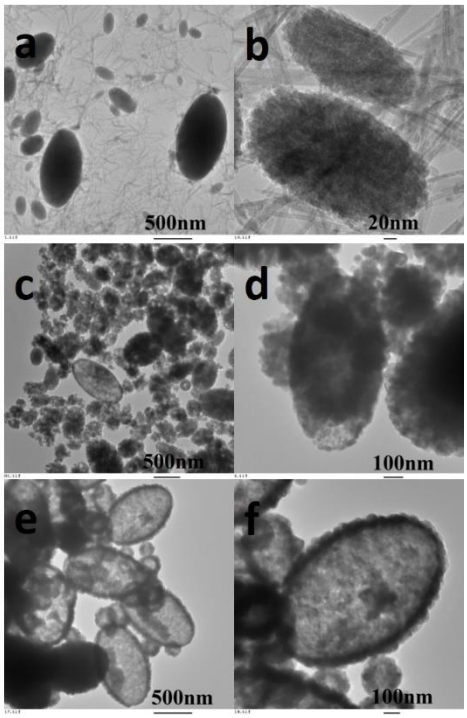

Fig.5-1-5. Ex-situ TEM characterization of α-Fe_2O_3 prepared with different time (a,b) 30min, (c,d) 75min and (e,f) 3h at low and high magnification.

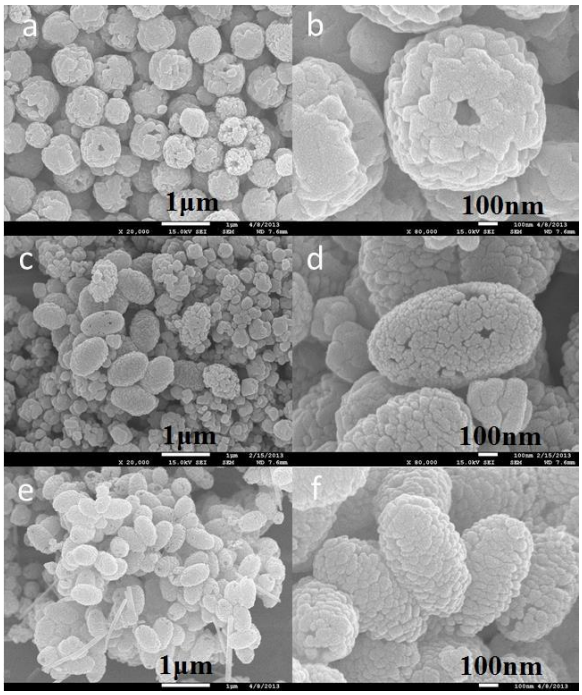

Fig.5-1-6. Effect of DMO concentration: FESEM images of α-Fe_2O_3 obtained with DMO at amount of (a,b) 0.2 mmol, (c,d) 0.4 mmol, (e,f) 0.8 mmol. (a,c,e) are low-magnification images, and their corresponding high-magnification images are (b,d,f).

To gain a fundamental understanding of the possible mechanism of formation for the unique hollow cocoon-like nanostructures, products obtained under different experimental conditions were thoroughly characterized by FESEM and TEM. Due to limitation of the hydrothermal reaction system with a sealed reactor under high pressure and high temperature, it is hard to monitor the formation of the nanostructures in situ. Therefore, ex situ analysis was carried out for a set of experiments with different reaction time. FESEM images of the particles obtained from different reaction times clearly reveal the growth and evolution from tiny nanoparticles to hollow nanococoons (Figure 5-1-4 a-f). Nanoparticles about 10 nm in size without any high-order structure were observed after 15 min (Figure 5-1-4a), indicating the initial stage of nucleation. When the reaction time was prolonged to 30 min, both nanorods and the sprouts of nanococoons covered with nanorods were observed (Figure 5-1-4b). TEM analysis shows that the sprouts of nanococoons were formed by nanorods assembly and were solid (Figure 5-1-5 a,b). When the

reaction time was increased to 60 min, nanococoons were more mature and no nanorods were left (Figure 5-1-4c). When the reaction time was further increased to 75 min, the nanococoons started to form porous structures (Figures 5-1-4d and 5-1-5 c,d). When the reaction time was 3 h, the nanococoons turned hollow as evidenced by broken holes on the surface of nanococoons (Figure 5-1-4e) and TEM (Figure 5-1-5 e,f). It is interesting to observe the transition from solid to hollow structure as direct evidence for the possible Ostwald Ripening mechanism. Furthermore, the subunits which aggregate to form nanococoons grew larger when reaction time was increased from 3 to 6 h. The effect of dimethyl oxalate on the morphology was explored as well (Figure 5-1-6). With a smaller amount of dimethyl oxalate at 0.2 mmol, hollow nanospheres with a diameter of ~800 nm formed rather than nanococoons (Figure 5-1-6 a,b). Only when the amount was increased to 0.4−0.8 mmol were hollow nanococoons observed (Figure 5-1-6 c−f). This indicates the important role of oxalate ions released from decomposition of dimethyl oxalate in guiding the formation of the nanococoons.

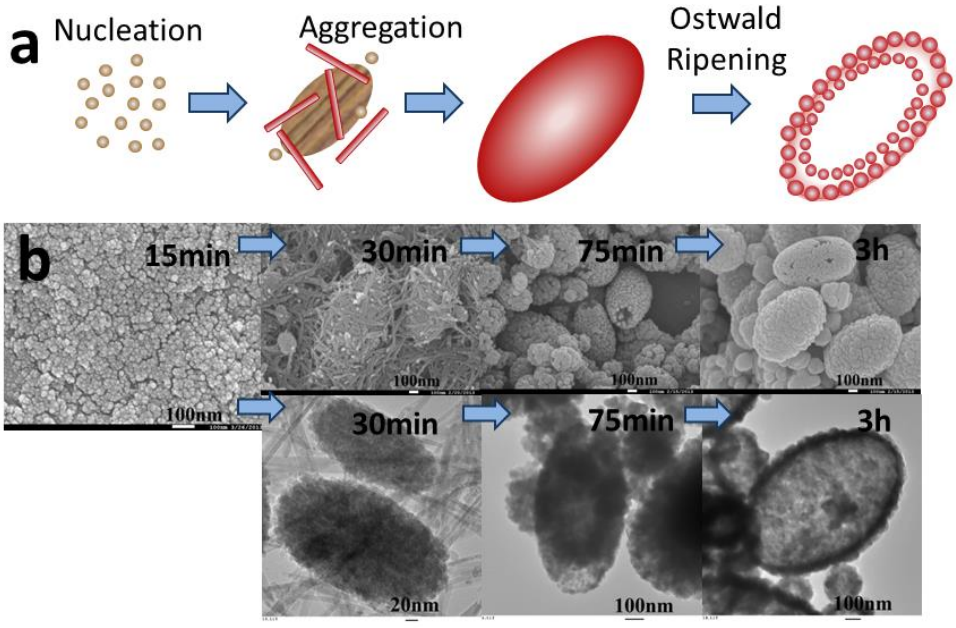

Fig.5-1-7. (a) Illustration of the proposed formation mechanism for hollow nanococoons; (b) ex-situ electron microscope images for samples prepared from 15, 30, 75 min, and 3h of reaction and the reaction time is labeled in each corresponding FESEM (top) and TEM (bottom) images.

On the basis of the experimental observation, a plausible formation mechanism is proposed and illustrated in Figure 5-1-7a. Once precipitation occurs, tiny colloids form first by nucleation generating tiny nanoparticles (Step 1). With the linear guiding property of oxalate ions released from dimethyl oxalate toward cations, nanorods are formed. During this stage, the newly produced nanorods possess high surface energy and tend to aggregate to form nanococoons to minimize surface energy of the system (Step 2 and 3). The formation of voids in the nanococoons is likely due to the Ostwald ripening mechanism as evidenced experimentally. The inner core area has higher surface energy due to aggregation of smaller primary units at an early stage and is easily dissolved as compared to the external shells. Ostwald ripening is strongly dependent on interfacial energy, crystal growth rate, and equilibrium solubility.[154] During the ripening process, the low-density cores are dissolved and are redistributed to surfaces to minimize energy. Therefore, hollow structures are formed. Figure 5-1-7b summarized the electron microscope characterization of the particles at the corresponding stage of formation, matching well with the illustration. However, further work is underway to obtain more details on the mechanism of formation.

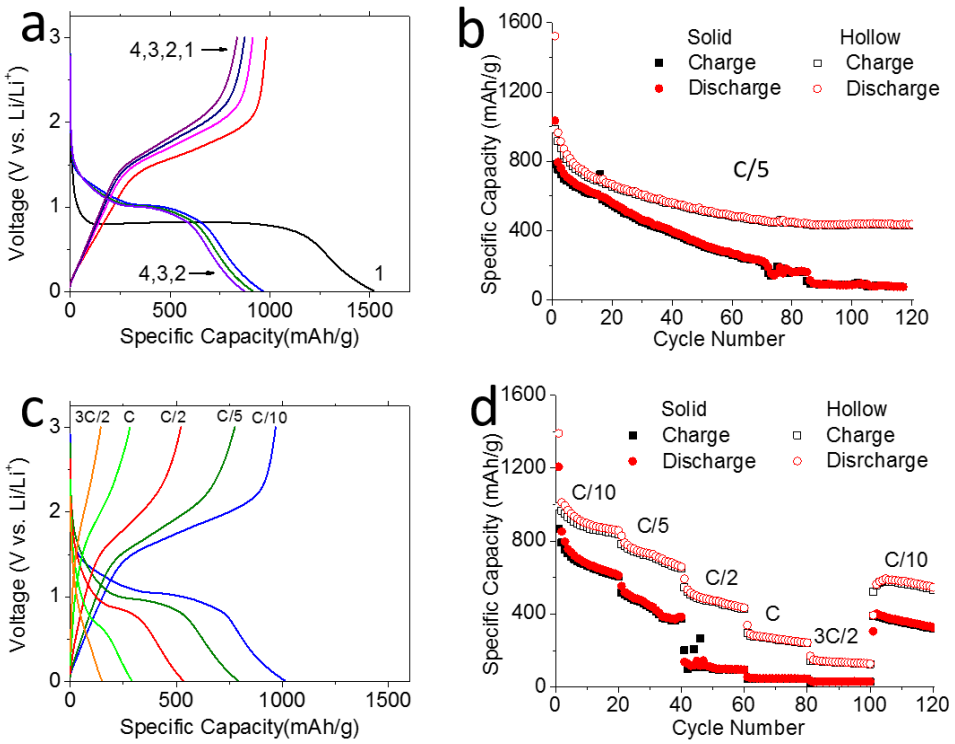

Fig. 5-1-8. (a) First 4 cycles of charge−discharge profiles of hollow nanococoons; (b) capacity vs cycle number plots of hollow and solid nanococoons at C/5 rate; (c) charge−discharge profiles at different current rates of C/10, C/5, C/2, C, and 3C/2 for one cell. (d) Rate performance of hollow vs solid nanococoons.

To demonstrate their potential application as anode materials for LIBs, hollow nanococoons of α-Fe_2O_3 were electrochemically evaluated in Swagelok testing cells. The first four cycles of charge−discharge profiles obtained at C/5 rate (1C = 1000 mA g^{-1}) are plotted in Figure 5-1-8a. The charge and discharge voltage plateaus are typical for α-Fe_2O_3 as reported in the literature.[29] The first cycle discharge (lithiation) and charge (delithiation) capacities are 1521 and 983 mA h g^{-1}, respectively. The 35% first cycle capacity loss can be attributed to the electrochemical reduction of Fe_2O_3 and decomposition of the electrolyte and formation of solid electrolyte interphase (SEI). The hollow structure formed by aggregation of subunits with large surface area would lead to nearly complete reduction reaction from Fe^{3+} to Fe^0 in the first cycle.[18] It is interesting to note that the plateau at around 1.2 V contributing 300 mA h g^{-1} observed by Reddy

et al.[148] and 1.58 V by Zhou et al. [73] is weak here. On the other hand, the plateau at ~0.75 V is dominant contributing 1200 mA h g^{-1} which may be assigned to the reduction of Fe ions to nanoscale Fe^0 metal and the formation of Li_2O. The slight difference observed in first cycle discharge profiles among α-Fe_2O_3 nanoflakes,[148] nanotubes,[18] multishelled hollow spheres,[73] and hollow nanococoons reported here suggests that the morphology of the nanoscale α-Fe_2O_3 may play a significant role in determining the discharge characteristics, which requires further studies. The voltage drop from below 0.75 to 0.01 V may be attributed to the formation of a solid electrolyte interphase (SEI) and decomposition of the solvent in the electrolyte.[148]The first cycle charge profile is similar to the second onward cycle charge profiles suggesting the same electrochemical reaction involved. The reaction could involve the decomposition of Li_2O with assistance of nanostructured metallic iron (Fe^0).[148] The similarity in second cycle discharge profile and those subsequent cycles suggests the electrochemical reaction is highly reversible.

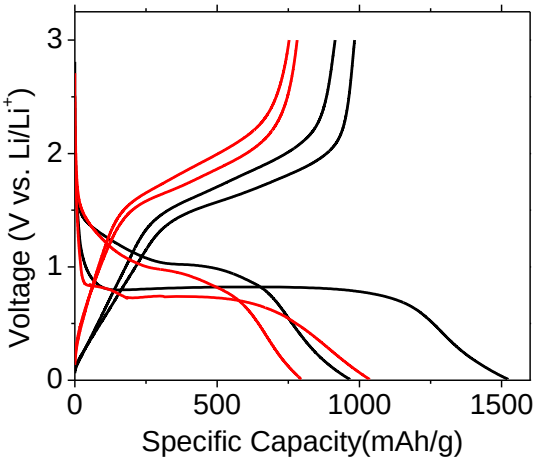

Fig.5-1-9. First two cycles of charge-discharge profiles of hollow (black) and solid (red) nanococoons.

The electrochemical reactions involved could be the following:[18,148,155]

$$Fe_2O_3 + 2Li^+ + 2e^- \Rightarrow Li_2(Fe_2O_3) \qquad (1)$$

$$Li_2(Fe_2O_3) + 4Li^+ + 4e^- \Rightarrow 2Fe^0 + 3Li_2O \quad (2)$$

$$2Fe^0 + 2Li_2O \leftrightharpoons 2Fe^{II}O + 4Li^+ + 4e^- \quad (3)$$

The cyclability was evaluated with prolong cycling test over 120 cycles at current rate of 200 mA g^{-1} (Figure 5-1-8b, hollow). The capacity of 437 mA h g^{-1} at 120th cycle is still 25% higher than that of commercial graphite with useful capacity of 350 mA h g^{-1}. Compared to micro α-Fe_2O_3 which faded to negligible capacity within 10 cycles,[132] the hollow nanococoons demonstrated significantly improved cycling performance over 120 cycles. Furthermore, rate performance of hollow nanococoons is also superior over those solid nanococoons (Figure 5-1-8d, hollow vs solid). The hollow nanococoons show comparable electrochemical performance to hollow spindles and hollow spheres reported.[26] On the other hand, the voltage plateaus and changes in the charge−discharge profiles are the same in both hollow and solid α-Fe_2O_3 nanococoons (Figure 5-1-9), indicating the same electrochemical reactions involved, as expected. These results suggest the important role of hollow structure in improving performance in reversible lithium ion storage. The superior electrochemical performance could be attributed to the hollow interior and porous shell structure of the nanococoon with building subunit aggregation. The unique structures can accommodate the volume change during the charge/discharge process and provide shorter distance for transportation of Li^+ ions. Furthermore, a high coulombic efficiency of 99% was achieved from 2nd cycle to 120th cycle.

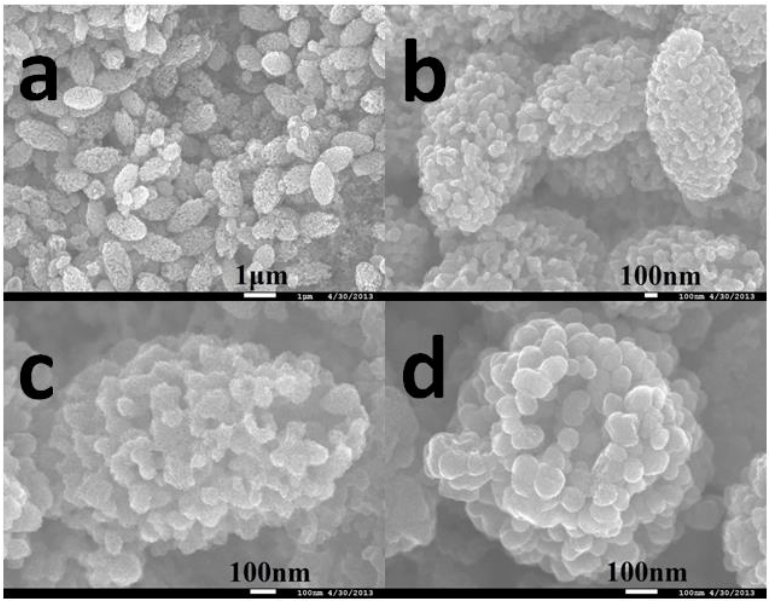

Fig.5-1-10. FESEM images for sample collected after the 120 cycles of test reveal the well maintained overall morphology of cocoon-like structure with high porosity, hollow nature, and constructed by building units.

The rate performance of the hollow nanococoons was evaluated by charging/discharging the cells at different current density from C/10, C/5, C/2, C, 1.5C, and back to C/10 for 20 cycles interval each (Figure 5-1-8 c,d). The charge-discharge profiles of the 2nd, 22nd, 42nd, 62nd, and 82nd cycles tested at C/10, C/5, C/2, C, and 1.5C, respectively, were plotted in Figure 5-1-8c. Specific capacities of 1013, 791, 534, 290, and 149 mA h g^{-1} were achieved at the corresponding current rates. It is particularly interesting to note that the capacity jumps back to 563 from 149 mA h g^{-1} when the current rate is reassumed to 100 mA g^{-1} from 1500 mA g^{-1} (Figure 5-1-8d, hollow). The results suggest that the electrode materials can sustain the extensive cycling at high rates, which is desirable. In fact, overall morphology of the nanocoons was well preserved after 120 cycles as revealed by FESEM images of the electrode disassembled after the cycling test (Figure 5-1-10 a−d). The high magnification images (Figure 5-1-10 c,d) clearly show that the size of the building units increased to about 100 nm, and the nanoporous nature is maintained. Furthermore, hollow structure is also preserved as observed from those broken nanococoons, and the hollow

core part is shrunk due to the enlarged building subunits (Figure 5-1-10). The unusual structural stability of the α-Fe_2O_3 nanococoons after 120 cycles, which is rarely observed for transition metal oxides of particle aggregates upon extensive cycling, will guarantee further investigation.

In conclusion, a novel facile template-free one-pot synthesis procedure for the preparation of hollow nanococoons α-Fe_2O_3 assembled by aggregation of subunits of nanoparticles was developed. The formation mechanism was revealed by ex situ analysis of the samples prepared from different times of reaction. Improved electrochemical performance in terms of cyclability, specific capacity, and high rate was achieved. Structure stability was exhibited by the analysis of the samples after 120 cycles. Experimental evidence clearly shows that hollow nanococoons are superior over solid nanococoons in reversible lithium ion storage.

5.2 α-Fe_2O_3 chevron microbeads

Microstructured materials of nanoparticle aggregates offer a number of notable advantages compared to random nanoparticles, generally: (1) microstructures have higher tap density, (2) microstructures have reduced inter-particle resistance, (3) microstructures have reduced surface induced side reactions, (4) microstructures have lower electrode–electrolyte contact area or less irreversible capacity loss associated with SEI formation. Meanwhile, the gaps or pores between nanoscale building units will facilitate electrolyte and ion transfer. For example, the microsized ensemble of Si@void@carbon nanoparticles demonstrated superior cyclability of 97% capacity retention after 1000 cycles due to the hierarchical arrangement of nanoparticles.[156] Micronano hierarchical structured $LiFePO_4$/C composites showed both excellent rate performance and high tap density as the positive electrode for LIBs.[157] Multishelled TiO_2 hollow microspheres have achieved superior cyclability at 10 C for 1200 cycles.[158] Microstructured Fe_2O_3 with improved electrochemical performance compared to random nanoparticles has been demonstrated to address

the issue of low volumetric energy density of Fe_2O_3 nanoparticles.[45] $Li_4Ti_5O_{12}$ microspheres with a size of ~10–20 μm formed by aggregated carbon-coated nanoparticles demonstrated improved rate performance due to enhanced conductivity and improved intercalation kinetics from its unique structure. Meanwhile, the microsized spheres also have an impressive high tap density of 0.82 g cm^{-3}.[159]

Microstructured materials can find important applications, including energy storage,[88,159-161] catalyst,[86,162,163] sensor,[164,165] carriers in medical application,[166] etc. For example, multishelled hollow microspheres of α-Fe_2O_3 ,Co_3O_4, and SnO_2 microbox have been used as negative electrode materials for LIBs achieving superior performances.[88,161] Au@TiO_2 core-shell hollow spheres,[167] multishelled ZnO hollow microspheres,[168] quintuple-shelled SnO_2 hollow microspheres,[169] have been reported for high performance dye-sensitized solar cells. Multi-shelled Mn_2O_3 hollow microspheres were prepared as high-performance supercapacitor electrodes.[170] Multi-shell Au/CeO_2 has demonstrated improved catalytic performance in the reduction of p-nitrophenolas.[171] Microspheres of $(ZnS)_x(CuInS_2)_{1-x}$, as photocatalysts with tunable band gap, have demonstrated excellent performances in water splitting.[162] Microspheres of ZnO have demonstrated impressive sensitivity in gas sensor application.[165] Hollow microspheres of polymers have been applied as injectable cell carriers for knee repair.[166] Both template-free and template-assisted approaches have been explored to create holes or hollow voids in microstructures.[82] Template-assisted synthesis is based on the use of sacrificed soft and hard templates.[29,172] Template-free synthesis is developed based various mechanisms of formation, such as Kirkendall effect,[114] Ostwald ripening process,[120,173] etching treatment,[86,88,89], and self-template fabrication.[174,175] Template-free synthesis is highly desirable in many cases where suitable templates are not easily available. However, template-free synthesis is not as predictable as those by template-assisted synthesis.

Therefore, it will be interesting to carve holes in microparticles from non-hollow microparticles to preserve the predictable microscale morphologies and achieve the advantages of hollow structures.

Here, we demonstrate that it is possible to carve tunnel-like holes in hematite microparticles forming a chevron bead-like morphology for high volumetric capacity negative electrodes in LIBs. The plausible formation mechanisms involved were revealed by extensive characterization. Experimentally evidenced, both the Ostwald ripening mechanism and the ionic etching process are involved in carving the unique tunnel-like holes in microparticles. The chevron bead-like structure can provide a higher surface to volume ratio, shorter transport lengths, and higher permeability, compared to solid microparticles. At the same time, the unique structure could have a relatively higher bulk density than that of highly hollow structures, which is favorable in many fields of applications, such as energy storage devices where the tap density matters. In LIBs, the electrolyte or lithium ions can easily reach the core part of the microstructures via the tunnels/holes and the diffusion distance of the electrolyte and the migration length of lithium ions in the microstructures with tunnel-like holes decreased to r/2, compared to a long diffusion distance of r in similar solid microparticles. The schematic of the comparison of solid microstructures and microstructures with tunnel-like holes in LIB application is illustrated in Fig. 5-2-1. The tunnels can theoretically increase the contact area between solid active materials and the liquid electrolyte and the length of electrolyte transfer from outside to the deepest part in microstructures is greatly decreased. Additionally, the tunnel-like holes can effectively accommodate the stress caused by the volume variation during the repeating lithium insertion/extraction processes. In other words, the microparticles with tunnel-like holes could offer the advantages of both high volumetric density and cyclability. The chevron bead-like hematite microstructures have a high tap density of 0.94 g cm^{-3}, which is significantly higher than that of commercial P25 TiO_2 nanoparticles at 0.13 g cm^{-3}

only, or more than a sevenfold increase. When tested as the electrode material for LIBs, the chevron bead like microparticles demonstrated improved electrochemical performances in terms of specific capacity, volumetric capacity, Coulombic efficiency, and cyclability compared to that of solid beads.

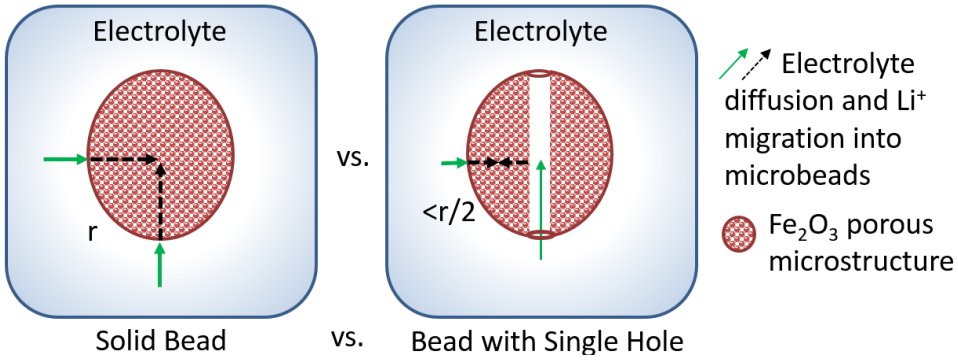

Fig. 5-2-1. Schematic to illustrate the shorter distance of electrolyte diffusion/Li^+ migration in a microstructure with tunnel-like holes (right) compared to that of a solid microstructure (left).

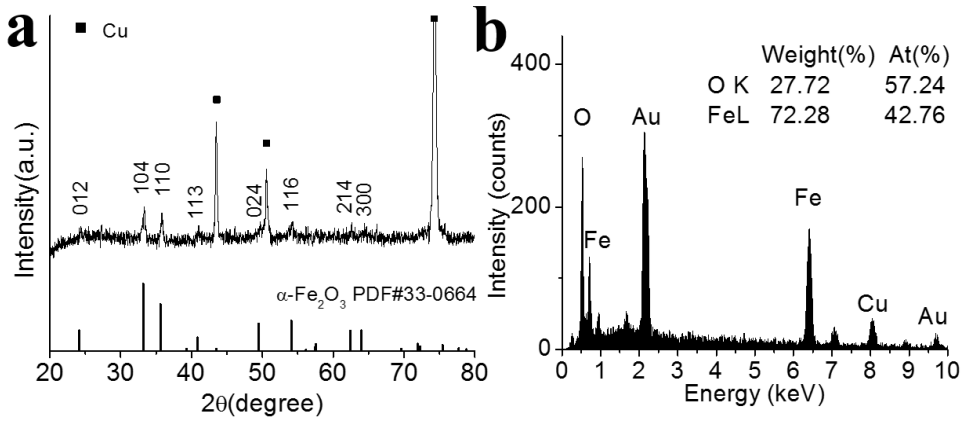

Fig. 5-2-2. (a) XRD pattern of the as-prepared α-Fe_2O_3 chevron microbeads. Peaks of Cu come from the Cu disc substrate. (b) EDS of the as-prepared α- Fe_2O_3 chevron microbeads showing the atomic ratio of Fe to O at ~2 : 3. Peaks of Au come from sputter coating of Au and Cu peaks are from the substrate.

The chemical composition of the as-prepared material was characterized by XRD and EDS (Fig. 5-2-2). All the XRD peaks can be assigned to α-Fe_2O_3 (Fig. 5-2-2a). The dominant copper peaks are from the sample holder. The peaks located at ~24°, 33°, 36°, 41°, 49°, 54°, 62°, and 63° are typical diffractions from α-Fe_2O_3 (JCPDS card no. 33-0664). The XRD analysis indicates that

the pure α phase of Fe_2O_3 was synthesized via the solvothermal method. The crystalline size calculated based on the Scherrer equation from the strongest (104) peak of α-Fe_2O_3 is 19 nm. The chemical composition of the as-prepared α-Fe_2O_3 was double-confirmed from the EDS spectrum (Fig. 5-2-2b). The atomic ratio of Fe : O is ~2 : 3, which is consistent with Fe_2O_3.

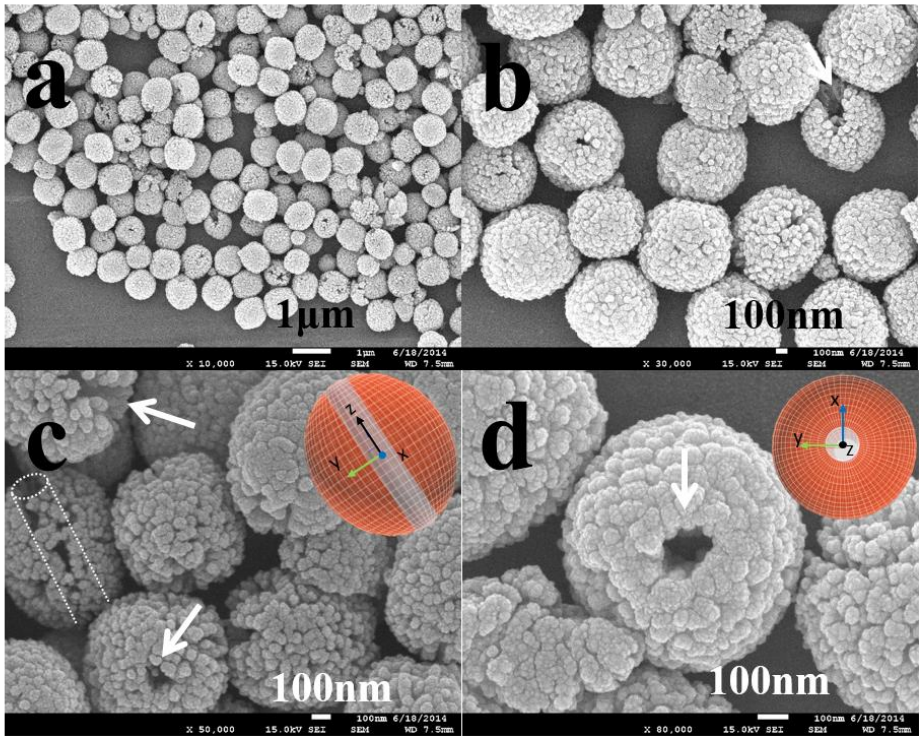

Fig. 5-2-3. FESEM images for typical α-Fe_2O_3 chevron microbeads with tunnel-like holes each at different magnifications: (a) overview of α-Fe_2O_3 microscale hole beads; (b) high magnification view of a few representative hole beads; the white arrow highlights the microbead with one end of the tunnel broken; and (c) one microbead with a broken shell suggests that the hole penetrates the core of the microbead forming a tunnel (marked by a dashed line); and (d) top view of a single hole bead clearly showing the rough surface inside and outside; insets of (c) and (d) are the 3D illustrations of the hole bead to easily interpret the direction of views of those corresponding FESEM images of microsized hole beads.

The morphology of α-Fe_2O_3 microbeads was revealed by FESEM (Fig. 5-2-3). The low-magnification FESEM image (Fig. 5-2-3a) shows the overall size distribution of the α-Fe_2O_3 microbeads and each bead is about 700 nm in length and 600 nm in width, all in chevron bead-like shape. Fig. 5-2-3b clearly shows the open endings/holes on the microbead, highlighted by the white

arrow. The holes are on the two ends of the long axis. A FESEM image with higher magnification (Fig. 5-2-3c) shows the tunnel-like holes in the microbeads (indicated by white arrows). A side-view of a microbead with the shell partially broken (highlighted by a dashed line) indicates that the tunnel connects the two ends through the microbead. A high-magnification FESEM image of the top view of a single chevron microbead is shown in Fig. 5-2-3d. The rough surface inside and outside of the microbeads suggests that the microbeads were constructed by aggregation of nanoparticles/grains as the basic building units. The size of the building units is around 20–30 nm, which is consistent with the size calculated by using the Scherrer equation based on XRD. To better interpret the morphology observed by FESEM, the 3D model of this microstructure was drawn. The insets in Fig. 5-2-3c and d show the 3D models of the corresponding microbeads which could help in visualizing the chevron microbeads viewed from different perspectives.

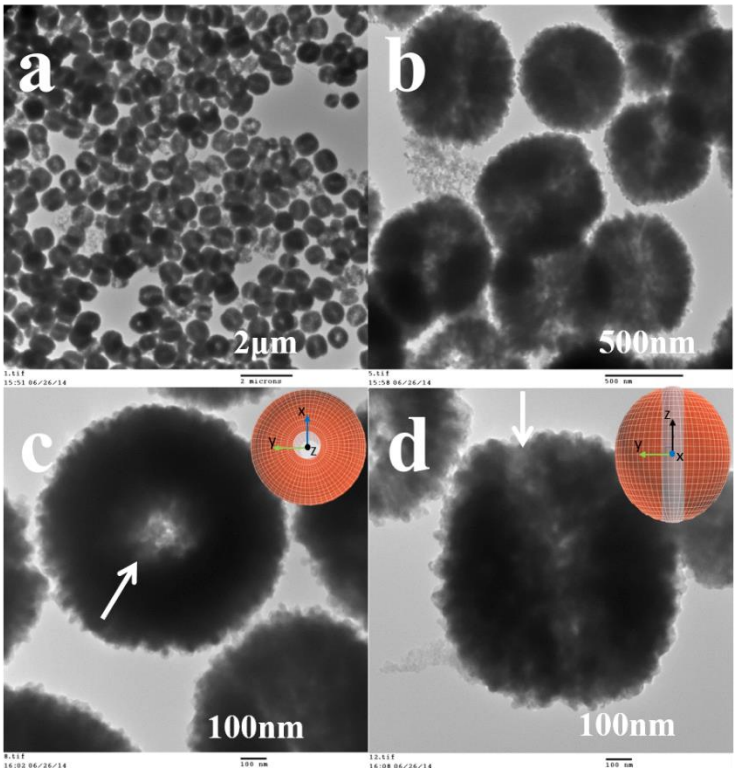

Fig. 5-2-4. TEM images of α-Fe2O3 chevron microbeads: (a) low-magnification view and (b) high-magnification view; (c) top view and (d) side view of the representative microbeads to clearly

reveal the tunnel-like holes. The tunnel-like holes are marked by white arrows. Insets show the corresponding 3D models to better interpret those TEM images.

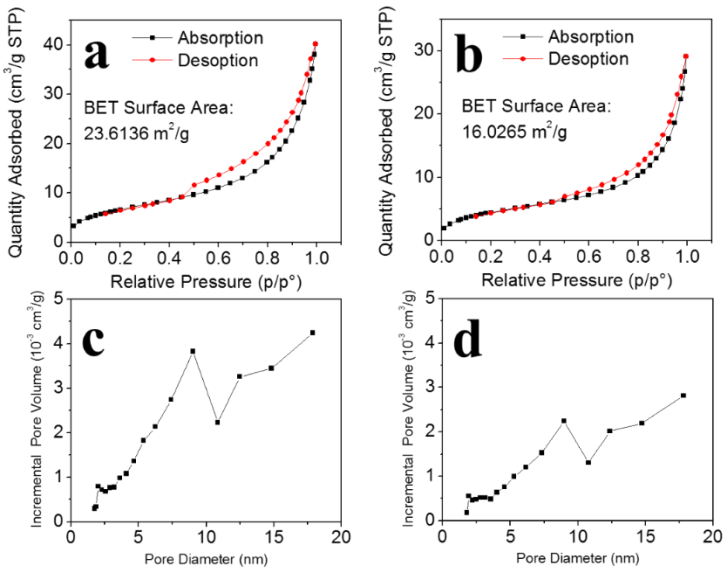

Fig. 5-2-5. BET analysis by N_2 gas adsorption-desorption isotherm of α-Fe_2O_3 (a) solid beads and (b) beads with tunnel-like hole; pore size distribution of α-Fe_2O_3 (c) solid beads and (d) beads with tunnel-like hole.

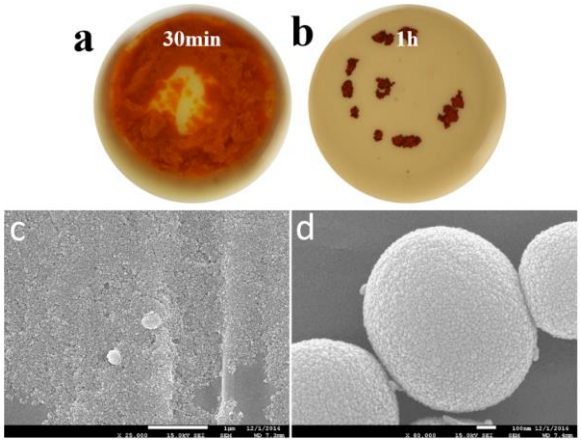

Fig. 5-2-6. The optical images show that (a) cloudy solid in orange color formed after 30 min of reaction and the solid is the precursor of Fe_2O_3, and (b) the Fe_2O_3 aggregates in typical red color formed after a reaction time of 1 h. The clear transparent solvent in reactor after 1 h, which was different from the dark yellow of $FeCl_3$ solution before reaction, indicates conversion of dissolved Fe^{3+} ions in solution to precipitate Fe_2O_3. The color of solid product did not further change with longer reaction time, possibly, due to the formation of solid Fe_2O_3. (c) and (d) Additional SEM characterization of the sample in (a) and (b), respectively.

The unique chevron bead-like structure was further revealed by TEM (Fig. 5-2-4). The overall view of the microbeads with a light contrast line in each bead reveals the tunnel-like holes in all microbeads (Fig. 5-2-4a). The high-magnification TEM image of a few representative hole beads more clearly shows the tunnels alight along the longest axis of the microbeads (Fig. 5-2-4b). The top view and the side view of the representative single microscale chevron bead are shown in Fig. 5-2-4 c and d, respectively. The observation of the ring-like TEM color contrast with a tiny hole in Fig. 5-2-4c suggests that the projection is along the tunnel or top view. The observation of a light contrast line inside the microbead more clearly shows the tunnel and the projection is perpendicular to the tunnel or side view (Fig. 5-2-4d). The 3D models are provided as the insets of Fig. 5-2-4 c and d to illustrate the corresponding microbeads viewed from different perspectives under a TEM. The surface area and pore size distribution of solid beads and beads with a tunnel obtained were investigated by BET analysis based on N_2 adsorption–desorption at 77 K (Fig. 5-2-5). The BET surface areas of solid and hole-beads were 23.6 $m^2\ g^{-1}$ and 16.0 $m^2\ g^{-1}$, respectively. It is interesting to note that the solid beads have a higher surface area than that of hole beads. This observation could be rationalized. Both beads were formed by aggregation of nanoparticles as building units. The beads with tunnel-like holes were formed after 3 h of reaction where the nanoparticle building units have a size of ∼20–30 nm. In contrast, the solid beads were formed after 1 h of reaction where the building units have a significantly small size of ∼5–10 nm (Fig. 5-2-6 c, d). Although tunnel-like holes were formed after 3 h, the total surface area actually decreased due to the fact that the holes generated were not enough to compensate for the area decreased due to crystalline growth. The pore size distributions obtained by the BJH method of both samples are similar: the pore size mainly centered around 9 nm. The pore diameter of 9 nm may be attributed to the void space between nanoparticle building unit aggregates.

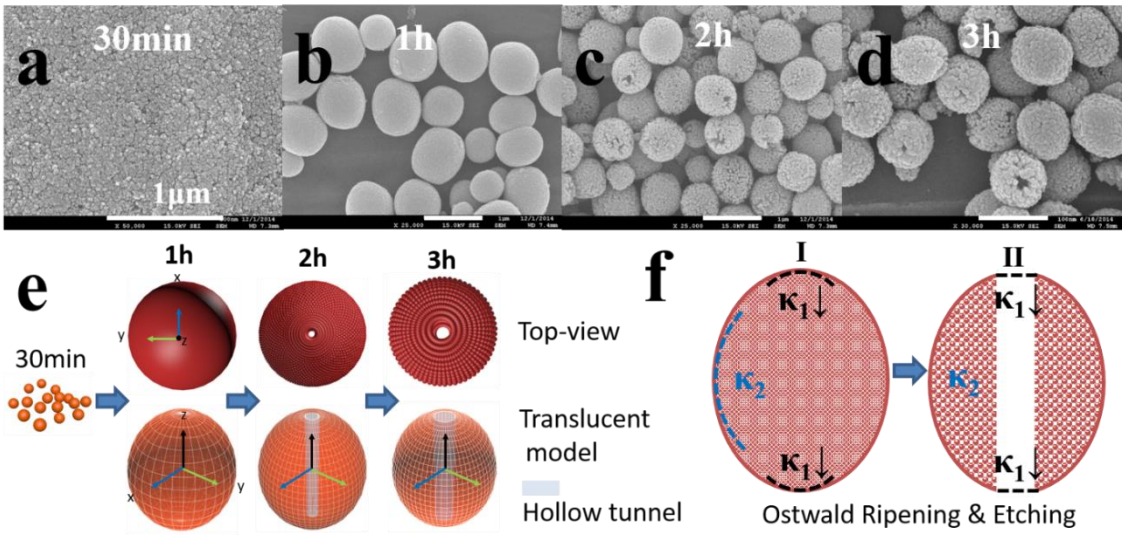

Fig. 5-2-7. (a–d) *Ex* situ FESEM characterization of particles obtained after different times of reaction to show the structural evolution: (a) 30 min; (b) 1 h; (c) 2 h; (d) 3 h. The scale bars of all FESEM images are 1 μm. (e) Illustrations of steps of structural evolution involved in the formation of micro chevron beads from time-course experiments of (a–d). (f) Illustration of the formation of tunnels through the Ostwald ripening process and the ion assisted etching process at locations of high curvature (κ1), leading to a fast dissolving process at those locations and formation of tunnel-like holes.

To understand the mechanism of the formation of the unique chevron microbeads, a set of time-course experiments, from 30 min to 3 h, were carried out. The structural evolution was revealed by ex situ FESEM characterization (Fig. 5-2-7a–d). At the early stage of the reaction after 30 min, nanoparticles were formed by nucleation and precipitation (Fig. 5-2-7a). The as-formed nanoparticles were brown in color (optical image, Fig. 5-2-6a), indicating intermediates or the precursors formed at this stage. At the second stage after 1 h, nanoparticles aggregated and formed solid microbeads of ellipsoid shape with a smooth surface (Fig. 5-2-7b). The aggregation and growth may be ascribed to the oxalate ions released by dimethyl oxalate which could guide the oriented attachment due to the ability of oxalate anions, as binary ligands, to bind with two metallic cations.[120] The optical image (Fig. 5-2-6b) shows the change of color from brown to red when the reaction time was increased from 30 min to 1 h, indicating the conversion of the nanoparticle

intermediate to α-Fe_2O_3 with typical red color. At the third stage after 2 h, the overall chevron bead-like microstructure started to form (Fig. 5-2-7c). The locations with higher surface energy or smaller building units are more vulnerable to be etched and dissolved. At the same time, the location with less surface energy or larger building units, continues to grow. The microbeads become porous due to the aggregation of larger building units. At the final stage after 3 h, the final α-Fe_2O_3 product with a distinguishable tunnel was formed. The plausible mechanism for the formation of tunnel-like holes is proposed based on our experimental observation and illustrated in Fig. 5-2-7f. Based on the Ostwald ripening mechanism, small nanoparticle building units, distributed mainly at locations with a large curvature or higher surface energy, are easily dissolved and re-precipitate onto big nanoparticles, to minimize energy.[176,177] Additionally, the Cl^- assisted H^+ etching may also contribute to the formation of tunnel-like holes. The anion-assisted etching of metal oxides like Cl^-, $[SO_4]^{2-}$ and $[VO_4]^{3-}$ assisted, or $[H_2PO_4]^-$ assisted etching of Fe_2O_3, and F^- assisted etching of TiO_2 have been reported where the etching only occurred at selective locations to create unique structures.[86,115,178,179]

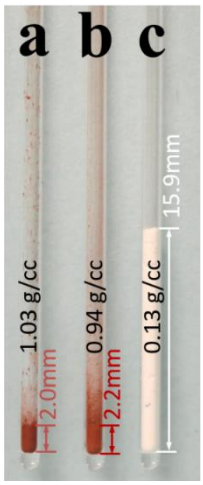

Fig. 5-2-8. Optical images to show different tap densities of (a) solid microbeads and (b) chevron microbeads of α-Fe_2O_3 with tunnels, (c) commercial TiO_2 nanoparticles (AEROXIDE, P25), in glass tubes with a height of 2.0 mm, 2.2 mm and 15.9 mm, respectively. The tap densities are

estimated to be 1.03 g cm^{-3}, 0.94 g cm^{-3} and 0.13 g cm^{-3} for solid microbeads, chevron microbeads with tunnels and TiO_2 nanoparticles, respectively.

In order to evaluate the volumetric capacity (mA h cm^{-3}), in addition to that of the specific capacity (gravimetric capacity mA h g^{-1}) dominantly used in battery research, the tap densities of the as-prepared beads with and without tunnels were measured. The tap densities of the as-prepared α-Fe_2O_3 solid microbeads and chevron microbeads with tunnels are much higher than that of a common commercial nanomaterial, TiO_2 nanoparticles (AEROXIDE TiO_2 P25) (Fig. 5-2-8). The solid microbeads were obtained following the same typical synthesis procedure outlined in the Experimental section, but with only 1 h reaction instead of 3 h (Fig. 5-2-7b). All the materials with the same weight were put into glass tubes with one end open and their heights were measured. The tap densities of micro solid beads and micro chevron beads were estimated to be 1.03 g cm^{-3} and 0.94 g cm^{-3}, respectively, using the tap density of commercial P25 at 0.13 g cm^{-3} as the reference.[89] We used P25 TiO_2 nanoparticles here as commercial α-Fe_2O_3 with the known tap density was not easily accessible to us. On the other hand, P25 TiO_2 has the known tap density and is widely used as a control in various studies. The much higher tap densities of both solid beads and beads with tunnels compared to that of TiO_2 nanoparticles can be attributed to their microscale structures. Compared to the solid microbeads, chevron microbeads with tunnels have slightly lower tap density due to the presence of nanotunnels in beads. The high tap density enables the application of α-Fe_2O_3 microbeads as promising high volumetric capacity negative electrode materials.

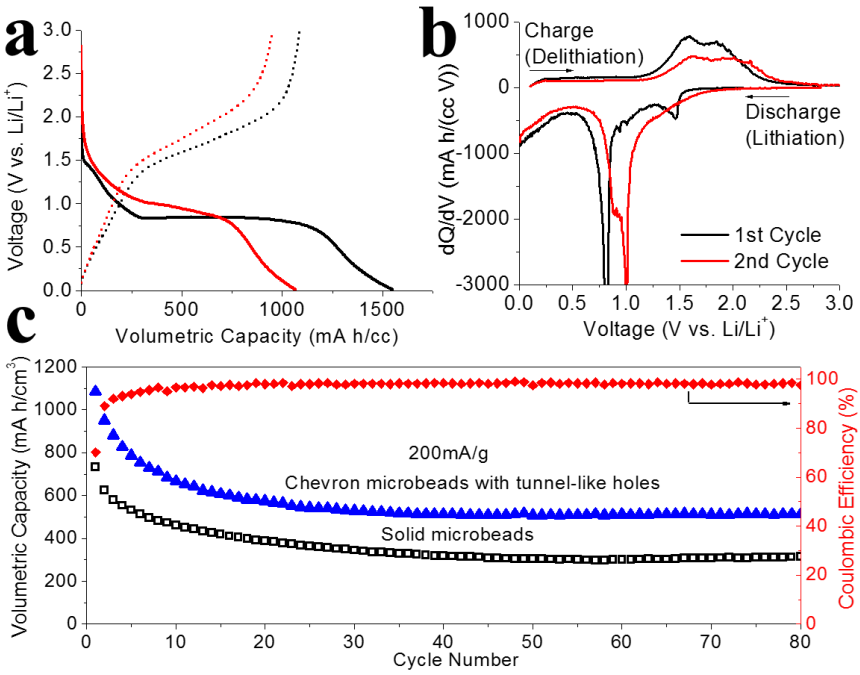

Fig. 5-2-9. Electrochemical performance of α-Fe_2O_3 micro chevron beads with tunnel-like holes: (a) charge–discharge profiles of the first two cycles; (b) dQ/dV vs. V plot for the first two cycles; and (c) cycling performance of the microbeads with tunnels (blue triangles) compared to solid microbeads for 80 cycles (black squares) in terms of volumetric capacity (mA h cm^{-3})

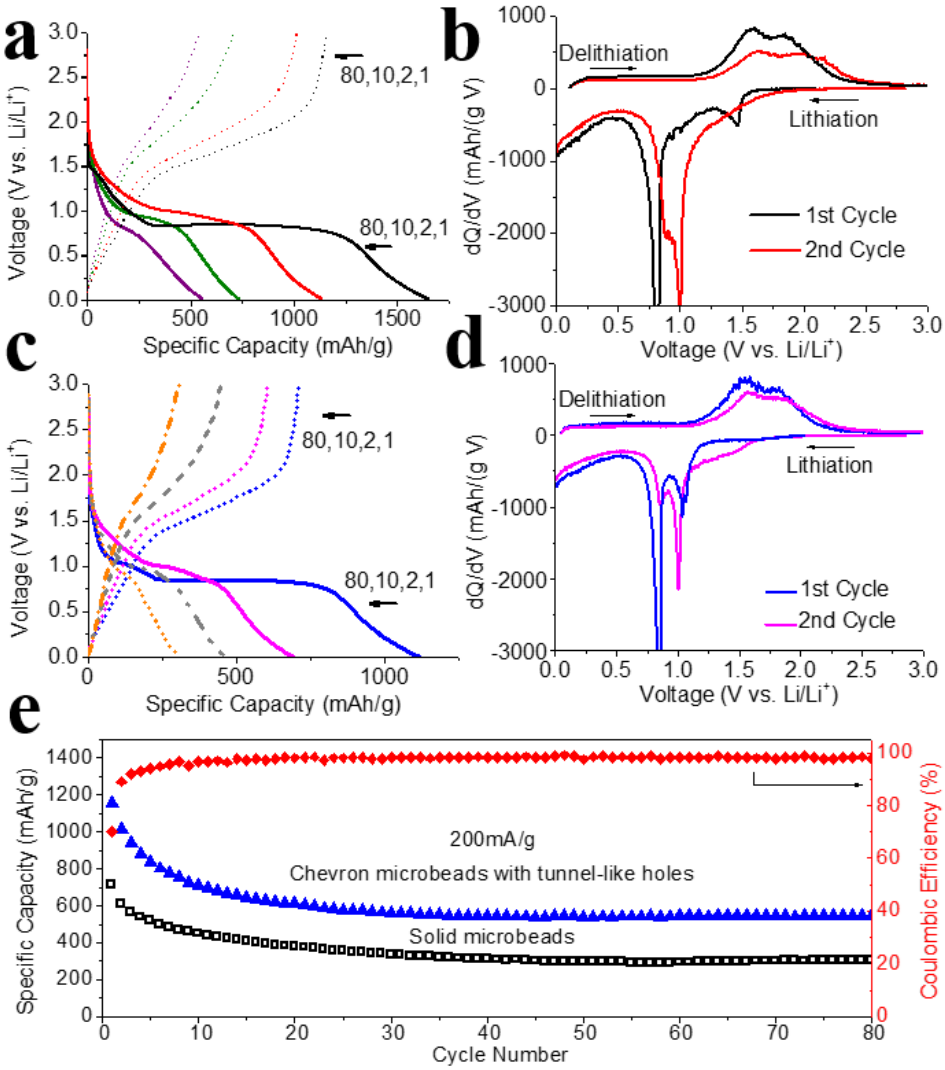

Fig. 5-2-10. Electrochemical performance of α-Fe_2O_3 micro chevron beads with tunnel-like holes and α-Fe_2O_3 solid microbeads in terms of specific capacity: (a) charge-discharge profiles for the 1st, 2nd, 10th and 80th cycles and (b) dQ/dV vs. V plot for the first two cycles of chevron microbeads; (c) charge-discharge profiles for the 1st, 2nd, 10th and 80th cycles and (d) dQ/dV vs. V plot for the first two cycles of solid microbeads for comparison. (e)cycling performance of α-Fe_2O_3 chevron microbeads and the corresponding solid microbeads for 80 cycles. The conventional unit of mA h/g is used here.

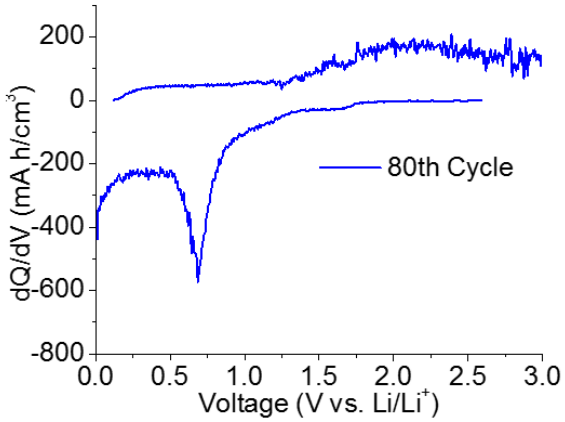

Fig. 5-2-11. dQ/dV vs V. plot of 80th cycle for the microbeads with tunnels.

The as-prepared α-Fe_2O_3 micro chevron beads with tunnellike holes and α-Fe_2O_3 solid microbeads were preliminarily tested as negative electrode materials for LIBs (Fig. 5-2-9). We would like to highlight that we used the volumetric capacity (mA h cm^{-3}) in our plots. The volumetric capacity was converted from the specific capacity (Fig. 5-2-10) based on the tap density established (Fig. 5-2-8). The charge–discharge profiles and the differential capacity (dQ/dV) vs. voltage plots for the first two cycles are shown in Fig. 5-2-9a and b, respectively. The first cycle discharge capacity is 1549 mA h cm^{-3} (1648 mA h g^{-1}). The volumetric energy storage density estimated is ~1400 Wh L^{-1}, based on pure anode materials in the Li-metal testing cell. A small slope starts at around 1.5 V and ends at around 0.8 V followed by a plateau at around 0.8 V (Fig. 5-2-9a). It can be attributed to the lithium intercalation into Fe_2O_3 and then the reduction of Fe^{3+} to Fe_0 and the formation of a solidelectrolyte interface (SEI), respectively.[82] The much higher specific capacity of the first cycle than the theoretical value (1007 mA h g^{-1}) and the first cycle irreversible capacity loss of ~479 mA h cm^{-3} (510 mA h g^{-1}, 31%) may be attributed to the formation of SEI and decomposition of the electrolyte in the first cycle.[30,161] To better interpret the electrochemical reactions involved, the dQ/dV vs. V plot was analyzed (Fig. 5-2-9b). A weak peak at ~1.5 V and a strong peak at ~0.8 V are observed in the first discharge profile, which can be assigned to the

intercalation of Li^+ and the reduction of the iron ion to metallic iron and the formation of SEI, respectively.[82,120,161,180] In the 2nd cycle, only one discharge peak can be observed and it shifted to ~1.0 V.[30,161] This shift of the peak is associated with drastic, lithium-driven, structural or textural modifications.[130,131] This peak gradually and slightly shifted from 1.0 back to 0.7 V from the 2nd cycle to the last cycle (80th cycle, dQ/dV in Fig. 5-2-11). In the charging process, a broad peak between 1.5 and 2.0 V can be observed, which can be attributed to delithiation reaction, corresponding to the oxidation of Fe^0 back to Fe^{3+}.[181] The cycling performance in terms of the volumetric capacity of chevron microbeads is shown in Fig. 5-2-9c. The sample was tested at a current of 200 mA g^{-1} for 80 cycles. The capacity fades in the first twenty cycles, and remains at around 514 mA h cm^{-3} for 60 more cycles.

The experimental results also confirmed that electrochemical performances can be enhanced by carving holes/tunnels in microscale particles from solid microparticles. The comparison of charge–discharge curves and dQ/dV plots indicates that the same electrochemical reactions were involved for both samples from the 1st cycle to the last cycle (Fig. 5-2-10 a–d). The cycling performance of the solid microbeads for 80 cycles was analyzed (Fig. 5-2-9c and 5-2-10e), compared to the chevron microbeads with tunnel-like holes. The chevron microbeads with tunnels possess higher discharge capacity in terms of both the specific capacity and volumetric capacity than that of solid microbeads. Although the tap density of solid beads is slightly higher than that of beads with tunnels, the much higher specific capacity of the latter still warrants that the volumetric density of beads with tunnels is higher than that of solid beads. The surface area of chevron microbeads with tunnel-like holes is less than that of solid microbeads, and both samples have similar pore size distribution. So the improved electrochemical performance can be attributed to the advantages provided by the carved holes in microparticles: (1) decreased distance for

electrolyte diffusion and Li-ion migration from the outside to the inside of the microbead structure; (2) alleviated stress caused by the volume variation during the repeating lithium insertion/extraction processes. There are many different parameters that could affect the electrochemical performances of the materials, including conductivity, morphology and size. Our results show that the void space may positively impact the electrochemical performance, even though the crystalline size increased. However, further studies are still required to gain better understanding. The charge–discharge curves and dQ/dV plots of α-Fe_2O_3 solid microbeads compared to those of α-Fe_2O_3 chevron microbeads are shown in Fig. 5-2-10. The positions of all the discharge/charge peaks of solid microbeads are almost identical to those of chevron microbeads with holes, indicating the same electrochemical reactions involved.[182,183] The practical specific capacity (by mass) of the as-prepared α-Fe_2O_3 microbeads (545 mA h g^{-1}) is in the same order of scale as commercial P25 TiO_2 (168 mA g^{-1}). However, the volumetric capacity density of the as-prepared α-Fe_2O_3 micro chevron beads is 514 mA h cm^{-3}, 50% higher than 345 mA h cm^{-1} of α-Fe_2O_3 solid microbeads, due to the much higher specific capacity compared to those of solid microbeads. And it has a volumetric capacity 23 times higher than 22 mA h cm^{-3} of P25 TiO_2. Therefore, the chevron microbeads could be promising as high tap density electrode materials for compact LIBs.

In summary, we have successfully prepared α-Fe_2O_3 micro chevron beads with tunnel-like holes by a facile and fast procedure. The formation mechanism was proposed based on experimental observations. When applied as the negative electrode materials for LIBs, the unique micro chevron beads with tunnel-like holes exhibited a reasonably stable volumetric capacity of ~514 mA h cm^{-3} for at least 80 cycles, which is superior to the solid microbeads. As a result, the

chevron bead-like hematite microstructures with high tap density and volumetric capacity will be promising negative electrode materials for high-energy density LIBs.

5.3 Olive-like α-Fe_3O_4/carbon composite

Rechargeable lithium-ion batteries (LIBs) have been attracting much attention in the past few decades. LIBs with high power and energy density are highly desirable in order to meet the increasing demand for energy storage, in particular, electric vehicles.[3,6,184,185] Currently, LIBs exclusively use carbon as negativeelectrode materials for its good cycling performance based on the intercalation/deintercalation mechanism of Li storage. However, the theoretical capacity of graphite at 372 mA h g^{-1} (based on LiC_6) has almost been achieved. On the other hand, the intercalation of lithium into graphite mainly occurs at low potential close to zero V (vs. Li/Li^+). Accidental overcharge at high currents may lead to the possible formation of lithium dendrites that short circuit anode and cathode and cause thermal runaway or even a fire. Recently, much attention has been devoted to the development of carbon-alternative negativeelectrode materials, which must have higher specific capacity and better safety performance than the widely adopted carbon anode.[3,6,143,185,186]

Various metal oxides have been extensively explored as carbon-alternatives, in particular, magnetite Fe_3O_4. [5,6,115,141,143] Fe_3O_4 has a theoretical capacity of 927 mA h g^{-1} and its potential of lithium insertion based on the conversion-type mechanism is significantly higher compared to that of carbon. Other advantages are low cost, abundance, environmental friendliness, and especially the high electrical conductivity at room temperature of about 2.5×10^2 S cm^{-1}.[187] High electrical conductivity is rarely observed in other metal oxides investigated for application in LIBs (e.g. α-Fe_2O_3 has an electrical conductivity of ~10^4 S cm^{-1}, which is six orders of magnitude or 10^{-6} lower than magnetite). High conductivity is highly desirable for electrodes in LIBs to facilitate charge

transfer.[188,189] However, as one of the conversion-type negative-electrode materials, the volume expansion (200%) of magnetite[190] is much larger than that of insertion-type negative-electrode materials (e.g., graphite) upon lithium insertion. This huge volume variation or pulverization could cause disintegration of the electrode and lead to poor cycling performance. This poor cyclability becomes one of the obstacles to commercialize Fe_3O_4 as negative-electrode materials in LIBs. On the other hand, based on the conversion-type lithium storage mechanism, Fe^0 nanograins will be generated through electrochemical reduction.[189] Fe^0 nanograins are highly reactive toward the organic electrolyte. The irreversible reactions on the surface of Fe^0 nanograins with the electrolyte could also cause poor cycling performance.[188] To address the poor cycling performance of Fe_3O_4, one strategy is to adopt nanoscale materials to buffer the volume variation during the charge–discharge process.[57,188-193] The other strategy is to add or coat with carbon to minimize the exposure between Fe^0 nanograins and organic electrolyte as well as to increase the electrical conductivity. For example, Fe_3O_4@C composites have been demonstrated to achieve a certain level of success in terms of electrochemical performances.[61,194-198] The composites include Fe_3O_4@C nanospindles,[57] Fe_3O_4@C nanorings,[198] and C-encapsulated Fe_3O_4 nanoparticles homogeneously embedded in porous graphitic carbon nanosheets.[199] Lou et al. reported a series of nanostructured iron oxide based anode materials for LIBs,[62] such as carbon coated Fe_2O_3 nanorods,[200] nanocubes,[72] microboxes,[74,175] nanotubes,[71] nanodiscs,[21] nanospheres,[29] hollow microspheres of Fe_3O_4,[91] nanohorns on CNTs,[82] and Fe_3O_4 nanospheres with carbon matrix.[201] Therefore, Fe_3O_4 could find promising application as negative electrodes in LIBs.

Herein, we reported a procedure to prepare porous olive-like carbon decorated Fe_3O_4 based additive-free electrodes with improved electrochemical performances. The porous Fe_2O_3/C precursor with olive-like particles obtained via ultrafast (75 min) one-pot synthesis was

constructed by aggregation of short nanorods with a length of 18 nm and a width of 8 nm. It is particularly interesting to highlight that a novel centrifugation-assisted deposition (CAD) method was developed to prepare additive-free carbon decorated Fe_3O_4 where active materials were directly prepared on the current collector. In other words, once the synthesis of active materials finished, the electrodes were ready. No binder, conductivity enhancer or solvent was employed. The electrodes could be directly assembled into cells without any post-synthesis processing. In contrast, traditional electrode preparation involves multiple steps of slurry preparation, coating, drying in a vacuum oven and additives (e.g., PVDF binder, carbon black conductivity enhancer and NMP solvent) are employed in the process, in addition to the conventional procedures to prepare the active electrode materials. The as-prepared additive-free porous carbon decorated Fe_3O_4 based electrodes exhibited superior electrochemical performances in LIBs. A specific capacity of 800 mA h g^{-1} could be maintained for at least 235 cycles with minimum capacity fading. Moreover, it exhibited excellent rate performance: specific capacities of 761, 752, and 727 mA h g^{-1} were achieved at high currents of 500, 1000 and 1500 mA g^{-1}, respectively. The results suggest that the binder-free carbon decorated Fe_3O_4 based electrode obtained by CAP could be potentially used in high-rate LIBs.

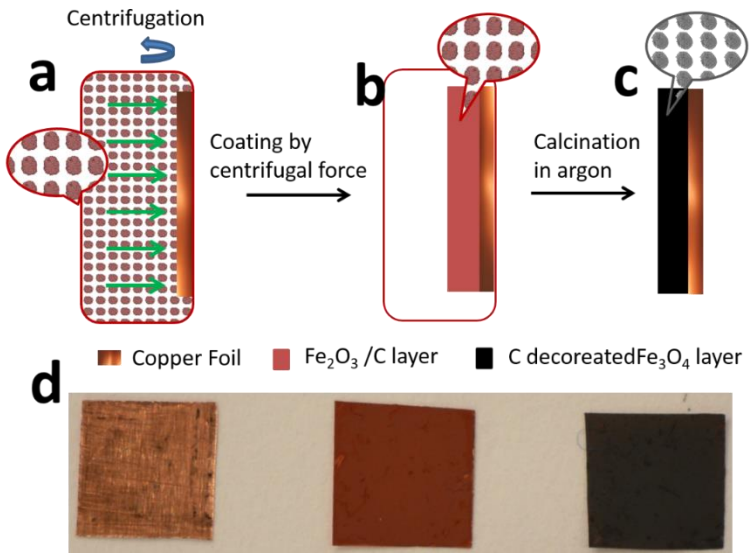

Scheme 5-3-1. Schematic of the CAP we developed to make additive-free electrode of olive-like carbon decorated Fe_3O_4: a) Fe_2O_3/C nanoparticle precursor dispersed in ethanol is coated on a Cu disc under centrifugation; (b) a layer of Fe_2O_3/C nanoparticles coated on only one side of the Cu disc; (c) a layer of carbon decorated Fe_3O_4 nanoparticles coated the Cu disc obtained by heating (b) in argon; (d) the corresponding optical images of the Cu discs at each step of treatment: from the left to the right, bare / Fe_2O_3/C layer coated / carbon decorated Fe_3O_4 layer coated Cu discs. Note: the other sides of those coated Cu discs were not coated by our method due to one-side deposition by centrifugation, Fig. 5-3-S2 in Supporting Information.

Preparation of additive-free ready electrode of olive-like carbon decorated Fe_3O_4.

Typically, the calculated amount of olive-like Fe_2O_3/C powders was dispersed into 5 ml of ethanol in a 50 ml centrifuge tube under ultrasonication to achieve a highly homogeneous suspension. A piece of clean copper disc typically used as a current collector was placed into the centrifuge tube and was centrifuged together with the mixture solution at 6000 rpm for 5 min. The olive-like Fe_2O_3/C nanoparticles were deposited by centrifugal force and coated firmly on only one side of the copper disc (Fig. 5-3-S1 in Supporting Information). The olive-like Fe_2O_3/C coated copper disc was dried in a vacuum oven at 80 ^oC overnight. To prepare an olive-like carbon decorated Fe_3O_4 based electrode, the coated copper disc was sintered in a tube furnace at a heating rate of 6 $^oC\ min^{-1}$ to 600 ^oC and maintained at the set temperature for 2 h under argon. The overall process and changes in compositions are illustrated in Scheme 5-3-1.

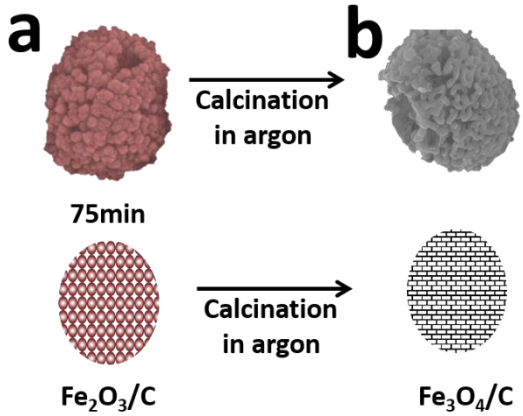

Fig. 5-3-1. Schematic illustration of the change in composition from Fe_2O_3/C to carbon decorated Fe_3O_4: (a) porous olive-like Fe_2O_3/C obtained through a solvothermal process after reaction time of 75 min. (b) Porous olive-like carbon decorated Fe_3O_4 from partial carbothermic reduction of Fe_2O_3 by carbon under calcination in argon.

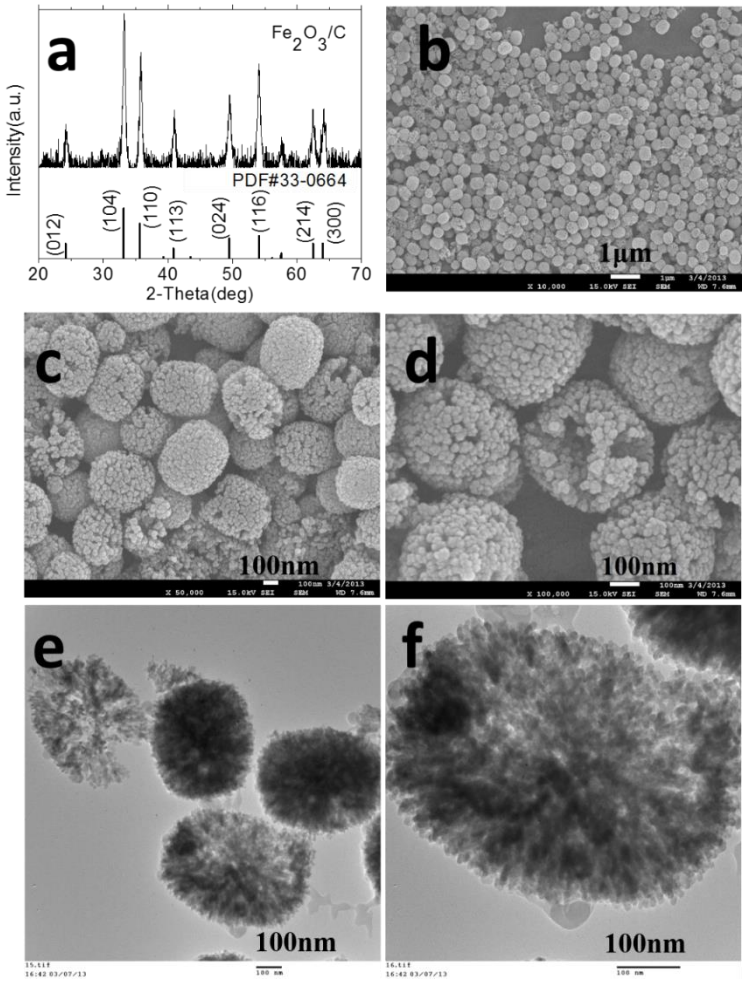

Fig. 5-3-2. Characterization of the olive-like porous Fe_2O_3/C precursor: (a) XRD pattern; (b) low-magnification FESEM image overall view; (c) high-magnification view of few typical olive-like porous Fe_2O_3/C nanoparticles; (d) zoom-in view showing a broken particle with the internal structure of nanorod aggregates revealed; (e) TEM images of few typical olive-like Fe_2O_3/C nanoparticles; and (f) zoom-in view showing the building units of nanorods.

Structure of porous olive-like Fe_2O_3/C

Porous olive-like Fe_2O_3/C nanoparticles, the precursor for making carbon decorated Fe_3O_4, were prepared through a fast solvothermal reaction with a reaction time of only 75 min and characterized by XRD, FESEM and TEM (Fig. 5-3-2). The XRD pattern of the as-prepared precursor can be indexed to a-Fe_2O_3 with rhombohedral structure (JCPDS card no. 33-0664) and no impurities are detected in the pattern (Fig. 5-3-2a). The crystalline size calculated from the Scherrer equation based on (110) peaks is 18 nm, which is in accordance with the size of building subunits observed under FESEM and TEM (Fig. 5-3-2d and f). The absence of carbon peaks suggests that the carbon from hydrothermally carbonized glucose is mainly amorphous.[202] The EDS (Fig. S5-3-3a in Supporting Information) exhibits that the as-prepared particles contain the elements of carbon, iron and oxygen as expected. Carbon was produced through the carbonization of glucose during the solvothermal process above 160 ^oC, which is well documented[57,198,202,203] The typical morphology and structure of the olive-like Fe_2O_3/C nanoparticles are clearly revealed by the FESEM images (Fig. 5-3-2b–d). The overall morphology and size distribution of the olive-like Fe_2O_3/C nanoparticles are revealed by the low-magnification FESEM image (Fig. 5-3-2b). The aspect ratio of the olive-like structure is around 3: 2, as shown in the high-magnification image (Fig. 5-3-2c). The olive-like a-Fe_2O_3/C nanoparticles are about 300–600 nm in length and 200–400 nm in diameter. More details of the internal structure of the nanoparticle are shown in the zoom-in view FESEM image (Fig. 5-3-2d): the olive-like nanoparticle is formed by aggregation of ordered small nanorods with a length of 18 nm and a width of 8 nm (which was further confirmed

by TEM). A broken olive-like structure at the center of the high-magnification FESEM image shows that the whole structure is highly porous, from the core to the surface. The structure of the a-Fe_2O_3/C composite is further revealed by the TEM characterization (Fig. 5-3-2e and f).

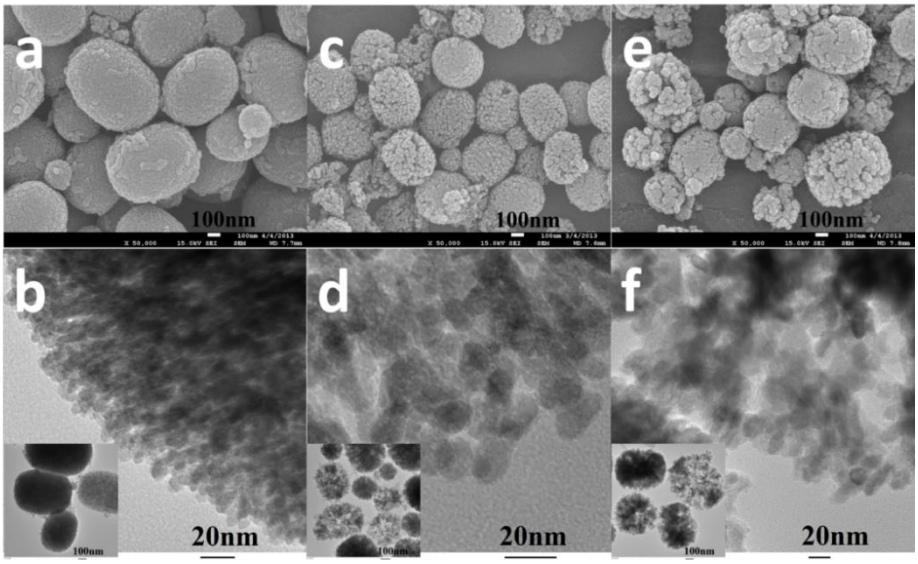

Fig. 5-3-3. Effect of reaction time: FESEM images (top row) and TEM images (bottom row) of olive-like Fe_2O_3/C nanoparticles prepared with different reaction times of (a and b) 45 min, (c and d) 75 min and (e and f) 3 h. Insets of (b, d and f) are the corresponding low-magnification TEM images.

Effect of experimental parameters on olive-like Fe_2O_3/C nanoparticles

A set of experiments were carried out to study the effect of reaction times on the structure of the olive-like Fe_2O_3/C precursors. Those nanoparticles obtained at different reaction times were characterized by FESEM and TEM (Fig. 5-3-3). When the reaction time was 45 min, less porous olive-like nanoparticles were formed (Fig. 5-3-3a and b and the inset of 3b). The nanorod subunits, with the length and width of around 18 and 8 nm, respectively, were aggregated to form the olive-like structure and closely packed (Fig. 5-3-3b). All the subunits of nanorods are well aligned in the same way, radiating from the core to the outside, as shown in Fig. 5-3-3b. As the reaction time increased from 45 min to 75 min, the olive-like structure became more porous, as evidenced by the more distinguishable gaps between fat nanorod subunits in Fig. 5-3-3c and d. The inset of Fig.

5-3-3d reveals that the whole olive-like structure is porous, which is consistent with the broken olive-like structure observed in the high magnification FESEM image (Fig. 5-3-2d). As the reaction time further increased to 3 h, the porous nature was preserved, as shown in Fig. 5-3-3e and the inset of Fig. 5-3-3f. However, with a longer reaction time, the length and diameter of the nanorod subunits increase to 23 and 10 nm, respectively. Also, the orientations of the subunits are more random, as compared to the samples prepared with shorter reaction times of 45 and 75 min. Besides the reaction time, the porosity and the shape of the as-prepared olive-like structure can be affected by the amount of glucose (Fig. 5-3-S4 in Supporting Information). With 0.4 mmol (Fig. 5-3-S4a and b in Supporting Information) or 0.2 mmol (Fig. 5-3-S4c and d in Supporting Information), the olive-like structures are highly porous with the nanorods as the basic building units. Occasionally, by-products of hollow nanoparticles were also observed (Fig. 5-3-S4c in Supporting Information). For comparison, with only 0.1 mmol glucose (Fig. 5-3-S4e and f in Supporting Information), the porosity of the olive-like structure is less than those obtained with 0.4 mmol or 0.2 mmol of glucose. A tunnel which connects the two ends of the olivelike structure and two open ends, instead of the highly porous structure was observed. We observed that the aspect ratio of the as prepared olive-like nanoparticles could be tuned through the control of the amount of glucose. The aspect ratio increases from 3: 2 to 2: 1 when the amount of glucose added is decreased from 0.4 mmol to 0.1 mmol. Without any glucose, a cocoon-like hollow structure with an aspect ratio of 2.5: 1 could be achieved.[9] We proposed that the amount of glucose could affect the aggregation of subunits leading to different structures of the aggregates. However, the fundamental explanation is still not clear at this time.

Based on the experimental observation, a plausible formation mechanism is proposed. The formation of porous olive-like nanoparticles starts from the hydrolysis of Fe^{3+} ions and nucleation

in solution and the subsequent formation of nanorods.[115] The nanorods as building units aggregate to form an olive-like structure and the nanorods are densely packed initially (Fig. 5-3-3a). The highly porous olive-like aggregates form with a longer reaction time (Fig. 5-3-3b). The small nanorod subunits, which possess higher surface energy in solution, tend to be dissolved more easily to minimize the total surface energy. Thus, the big nanorods grow with the continuous dissolving of small subunits and re-deposition on large subunits. With the decrease of the number of small nanorods and the increase of the size of the large nanorods, void spaces are generated and the particles become porous. Meanwhile, the aspect ratio and the porosity can be tuned through the control of glucose. It might be because the glucose or the deposited carbon may influence the surface property of the nanorod subunits and their aggregation. Thus, the orientated alignment of the subunits could be different from those in the system without glucose.[115] Our current ongoing effort is to systematically study the effects of experimental parameters and further understand the formation mechanism.

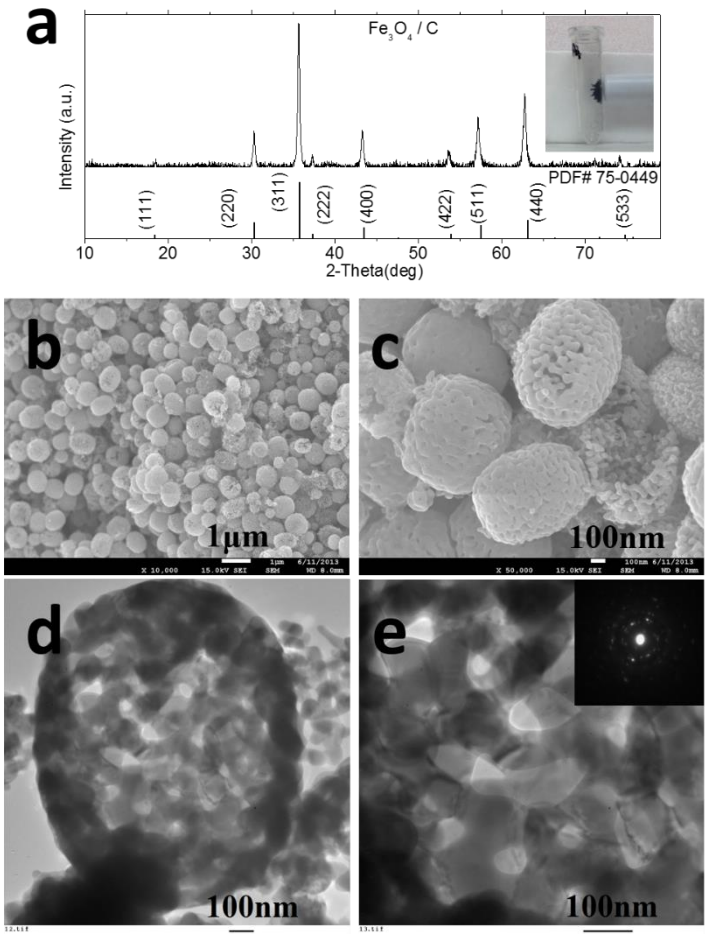

Fig. 5-3-4. Characterization of the olive-like carbon decorated Fe_3O_4 obtained by in situ carbothermic conversion from Fe_2O_3/C: (a) XRD pattern; (b) optical image shows the black colored carbon decorated Fe_3O_4 and its magnetic property; FESEM images at (c) low-magnification overall view, and (d) high-magnification view of few typical particles; TEM images of (e) a typical carbon decorated Fe_3O_4 olive-like nanoparticle, and (f) zoom-in view of a section of (e) showing the building subunits. Inset of (f) is the typical SAED pattern of crystalline Fe_3O_4.

Structure of the olive-like carbon decorated Fe_3O_4

The as-prepared olive-like Fe_2O_3/C could be converted to carbon decorated Fe_3O_4 preserving the overall morphology well. The successful partial reduction of Fe_2O_3 was proved by the evidence that Fe_3O_4 was produced as revealed by XRD (Fig. 5-3-4a). All the peaks of the XRD pattern can be assigned to Fe_3O_4 (JCPDS card no.75-0449), and no peak of a-Fe_2O_3 is observed, suggesting that carbothermic conversion of Fe_2O_3 into Fe_3O_4 was successful and complete. The crystalline sizes of

as prepared Fe_3O_4 are 45nm, calculated based on the (220) peak, which is significantly larger than the crystallite size of the Fe_2O_3 precursor at around 20 nm. The typical black color of Fe_3O_4,[57,204] rather than the typical red color of Fe_2O_3, was obtained and all the black power of olive-like carbon decorated Fe_3O_4 attracted by a magnetic bar (Fig. 5-3-4b) demonstrate that Fe_2O_3 was successfully converted to Fe_3O_4. Note that the powder of carbon decorated Fe_3O_4 was obtained without being coated on the copper disc by CAP in this case and the precursor powder was heat treated similarly under argon in a crucible. The conversion from Fe_2O_3 to Fe_3O_4 under inert gas also proves the existence of carbon produced by the solvothermal carbonization of glucose, which acts as the only reducing agent to convert Fe_2O_3 to Fe_3O_4.The morphology of as-synthesized olive-like carbon decorated Fe_3O_4 was revealed by FESEM and TEM images in Fig. 5-3-4c–f. After the calcination at 600 ^oC under Ar, the olive-like structure was maintained (Fig. 5-3-4c and d). The porosity of the olivelike carbon decorated Fe_3O_4 is also preserved, revealed by the broken olive-like structure in Fig. 5-3-4d. The size of subunits of carbon decorated Fe_3O_4 increased to around 50 nm from 18 nm subunits in the Fe_2O_3/C precursor (Fig. 5-3-4e and f), which is consistent with the sizes estimated from the XRD. The increase in size of subunits can be attributed to the high temperature annealing induced crystalline growth. As compared to the Fe_2O_3/C aggregates assembled by aligned nanorods, carbon decorated Fe_3O_4 was constructed by joined subunits. The connection of building subunits may be attributed to the annealing process where subunits are joined by grain boundary diffusions which was also observed in the study of other metal oxide nanomaterials.[120] It may also be attributed to the consumption of carbon in Fe_2O_3 through the carbothermic reduction process which eliminates the impurities between grain boundaries. The SAED pattern (the inset of Fig. 5-3-4e) demonstrates that the olive-like carbon decorated Fe_3O_4 is crystalline with all the diffraction spots assigned to Fe_3O_4.

The carbon content in the as-prepared Fe_3O_4/C materials is quantitatively determined by the TGA analysis (Fig. 5-3-S5 in Supporting Information). The small weight loss below 150 ^oC was due to the evaporation of the adsorbed moisture or gaseous molecules. The combustion of carbon begins at around 300 ^oC.[201,203] Fe_3O_4 can be oxidized to Fe_2O_3 when heated in air,[201,203] and the theoretical weight increase is 3.45%, based on the chemical reaction $4\ Fe_3O_4 + O_2 \rightarrow 6\ Fe_2O_3$. From TGA analysis, the carbon content of the carbon decorated Fe_3O_4 nanoparticle was estimated to be 0.43%.

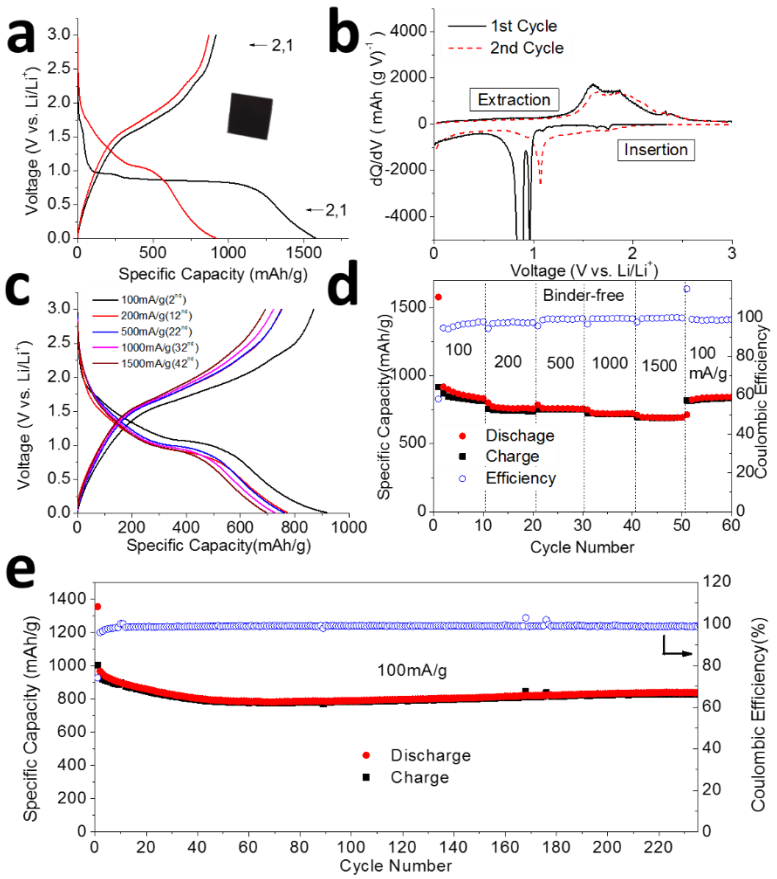

Fig. 5-3-5. Electrochemical measurement of additive-free carbon decorated Fe_3O_4 fabricated directly on a copper current collector: (a) first two cycle charge–discharge profiles; the inset of (a) shows the optical image of black additive-free Fe_3O_4 on a copper disc as a ready electrode; (b) differential capacity profiles for first two cycles; (c) charge–discharge voltage profiles and (d) rate performances and Coulombic efficiency at different currents from 100 to 1500 mA g^{-1}; (e) cycling performance at 100 mA g^{-1}.

Electrochemical performance of olive-like carbon decorated Fe_3O_4 in lithium storage

The as-prepared olive-like carbon decorated Fe_3O_4 nanoparticle fabricated directly on a copper disc was used as an additive-free ready electrode and assembled into a coin-type cell directly and evaluated. The electrochemical properties of the as-prepared additive-free Fe_3O_4/C electrode are shown in Fig. 5-3-5. An optical image of the additive-free carbon decorated Fe_3O_4 as a ready electrode for cell assembly is shown in the inset of Fig. 5-3-5a. The charge–discharge profiles of the first two cycles at the current of 100 mA g_1 with a cutoff voltage window of 0.01–3.0 V are shown in Fig. 5a. In the first discharge curve, two potential plateaus at about 0.9 and 0.8 V are observed, which can be ascribed to the formation of a Li–Fe–O compound, the conversion reaction of the Li–Fe–O compound to Fe_0 and the formation of the Li_2O matrix.[14-15,195,205] This profile is different from the first cycle discharge profile of Fe_2O_3 negative-electrode materials,[205] which has two potential plateaus at around 1.6 and 0.8 V versus Li^+/Li (Fig. 5-3-S6a in Supporting Information). For the Fe_2O_3/C precursor, the potential plateau at around 1.6 V can be ascribed to the intercalation of Li_+ into a-Fe_2O_3, and the other potential plateau at around 0.8 V is due to the formation of $Li_2(Fe_2O_3)$ and the reduction of Fe ions to Fe^0.[57,205,18] The difference between the first cycle discharge profile of carbon decorated Fe_3O_4 (Fig. 5-3-5a) and the Fe_2O_3/C precursor materials (Fig. 5-3-S7a in Supporting Information) illustrates the different electrochemical reactions involved during the first cycle of Li insertion, which also indirectly proves the successful conversion from Fe_2O_3 to Fe_3O_4 by in situ partial carbothermic reduction. The voltage drop from below 0.8 to 0.01 V could be attributed to the formation of a solid electrolyte interphase (SEI) due to the decomposition of the solvent in the electrolyte.[59,188,195,198,205,206]

In the first cycle charge profile, the plateau around 1.7 V is attributed to the oxidation of Fe^0 to Fe^{2+} and Fe^{3+}.[206] The first cycle discharge and charge capacities are 1579 and 917 mA h g^{-1},

respectively. The irreversible capacity loss of around 42% could be attributed to the electrochemical reduction of Fe_3O_4, the decomposition of the electrolyte and formation of solid electrolyte interphase (SEI).[195] To better interpret the electrochemical reactions involved, the dQ/dV vs. V plots for the first two cycles are shown in Figure 5-3-5b, which matches well with plateaus discussed above. Additionally, the absence of the typical reduction peak at around 1.6 V widely observed for Fe_2O_3 proves that the electrode is based on Fe_3O_4.[29,61,109,193,205] In the 2nd cycle, both reduction and oxidation peaks are positively shifted as compared to the 1st cycle.

The charge–discharge voltage profiles at different currents of 100, 200, 500, 1000 and 1500mAg^{-1} are shown in Figure 5-3-5c, which are at the 2nd, 12th, 22nd, 32nd, and 42nd cycle, respectively. The charge–discharge voltage profiles at different currents almost overlap, which demonstrates the same reversible electrochemical reactions involved. The specific discharge capacities are 919, 772, 761, 752, and 727 mA h g^{-1} at currents of 100, 200, 500, 1000 and 1500 mA g^{-1}, respectively. As we can see, the capacity fades slowly at the currents from 200 to 1500 mA g^{-1}, which has rarely observed for metal oxides tested in LIBs. And even at a high current of 1500 mA g^{-1}, the specific discharge capacities can still be maintained at 727 mA h g^{-1}, which shows improved rate performance as-compared to most reported Fe_3O_4 nanomaterial based anodes.[57,195,197]

The rate performances of the binder-free Fe_3O_4/C electrode was evaluated by charge-discharge the battery cells at different current densities for 10 cycles interval (Figure 5d). The average Coulombic efficiency from the 2nd is as high as 98.92%, which indicates the excellent electrochemical reversibility. The capacities are very stable and no distinguishable capacity drop can be observed at each current. It is interesting to highlight that no significant capacity drop observed when current was doubled, which suggests the electrodes could be used in fast charge LIBs. It is interesting to observe the specific capacity was recovered to 835.5mA h g^{-1} after 60

cycles, when the current was changed back to 100mA g^{-1}. More interestingly, we observe an increase of capacity after the current is recovered to 100mAg^{-1} from 1500mAg^{-1}. This could be explained by continuous activating process of the electrode.[59,141,207] Excellent cycling performance was achieved with a specific capacity at ~800 mA h g^{-1} for at least 235 cycles (Figure 5-3-5e). The superior electrochemical performances could be attributed to its porous structure induced good accessibility of Li^+ ions and improved strain accommodation and the way electrode prepared. In contrast, the conventional electrode prepared from the same C-doped Fe_3O_4 demonstrated poor cycling performances (Figure 5-3-S6 in Supporting Information), which indicates the critical role of electrode preparation. The olive-like shape could still be observed from the sample of C-doped Fe_3O_4 nanoparticles after cycling, indicating relatively structural stability (Figure 5-3-S8 in Supporting Information). As a comparison, the additive-free Fe_2O_3/C electrode shows very poor electrochemical performance (Figure 5-3-S7 in Supporting Information).

In summary, porous olive-like carbon decorated Fe_3O_4 was successfully prepared from porous olive-like Fe_2O_3/C precursor nanoparticles. The precursor was obtained by a fast one-pot solvothermal method. A novel CAP method to prepare an additive-free electrode was developed for the first time. The active materials were synthesized on a current collector by CAD directly without any binder, conductivity enhancer or solvent employed. When tested as negative-electrode materials for LIBs, the additive-free olive-like Fe_3O_4/C electrodes exhibited excellent electrochemical performances for lithium storage demonstrating their promising potential to be carbon alternatives for SIBs.

Supporting Information (Supporting Figures)

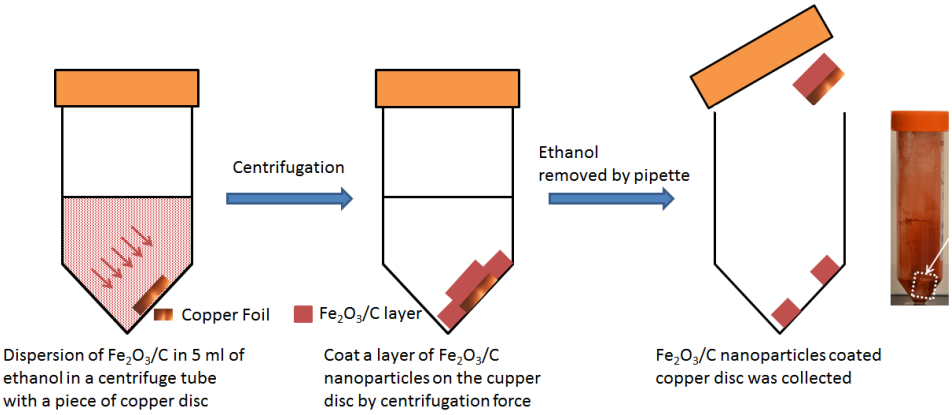

Fig. 5-3-S1. Schematic of the process of centrifugation-assisted preparation of additive-free electrode of olive-like Fe_2O_3/C coated directly on copper current collector. Optical image of the centrifuge tube after coating and the dash square highlighted the location of olive-like Fe_2O_3/C coated on copper current collector collected.

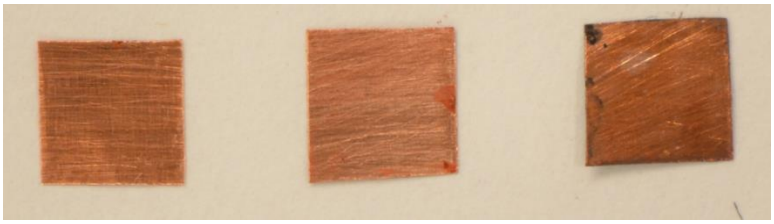

Fig. 5-3-S2. The corresponding optical image of the other side of Cu discs at each step of treatment showing that no Fe_2O_3/C layer or Fe_3O_4/C layer coated on the other side of copper discs: from the left to the right, back view of bare → Fe_2O_3/C layer coated → Fe_3O_4/C layer coated Cu discs.

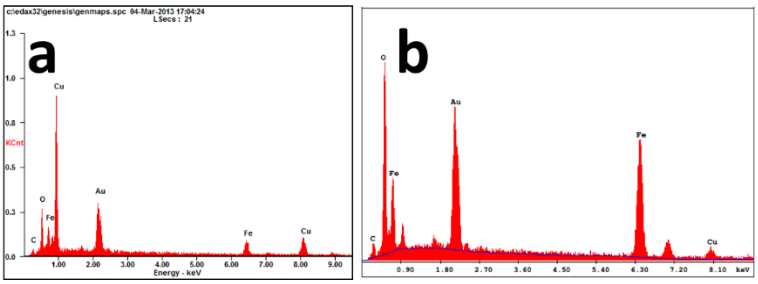

Fig. 5-3-S3. EDS analysis of (a) precursor of olive-like Fe_2O_3/C, and (b) carbon decorated Fe_3O_4 obtained by in-situ carbothermic partial reduction of the precursor. Au and Cu peaks are from sample coating and sample holder respectively.

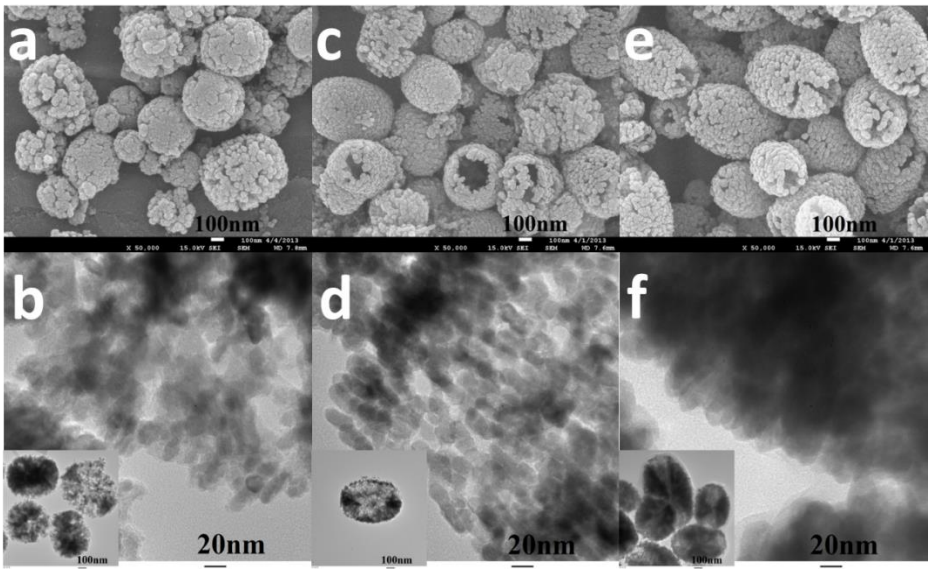

Fig. 5-3-S4. Effect of amount of glucose: FESEM images (top row) and TEM images (bottom row) of Fe_2O_3/C nanoparticles prepared with (a, b) 0.4, (c, d) 0.2 and (e, f) 0.1 mmol of glucose. Insets of (b,d,f) are low magnification TEM images with scale bar of 100 nm. The reaction time was 3 h instead of 75 min.

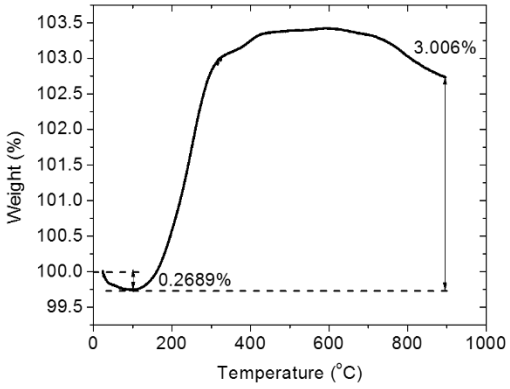

Fig. 5-3-S5. TGA profile of the carbon decorated Fe_3O_4 nanoparticles analyzed in air.

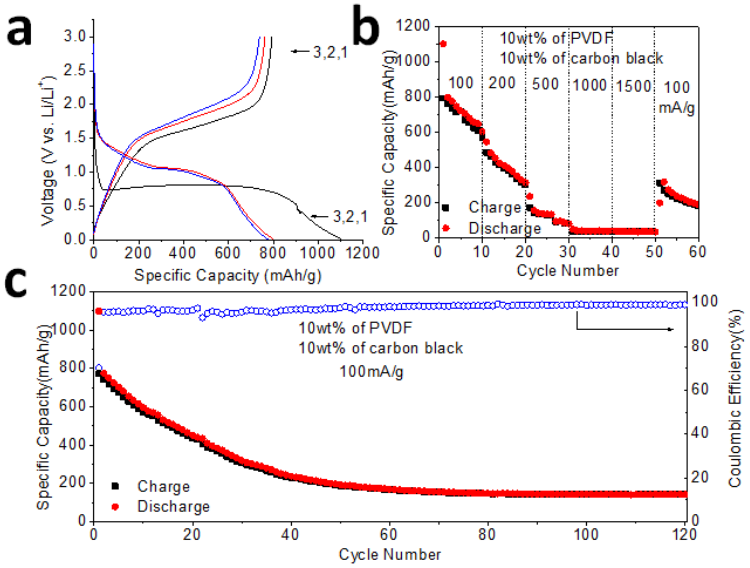

Fig. 5-3-S6. Electrochemical measurement of electrode prepared by conventional method* (slurry, coating and drying, with 10% binder and 10% carbon black) from the same olive-like Fe_3O_4/C: (a) Charge–discharge voltage profile for the initial three cycles at rate of 100 mA/g, (b) rate performance at current of 100, 200, 500, 1000 and 1500 mA/g at interval of 10 cycles each, and (c) cycling performance at current of 100 mA/g. *Note: the active materials of C-doped Fe_3O_4 was mixed 10 wt% PVPF binder, 10 wt% carbon black conductivity enhancer in a NMP solvent to make a slurry by stirring overnight. The slurry was then coated on to a copper current collector. The coated current collector was dried in a vacuum oven overnight.

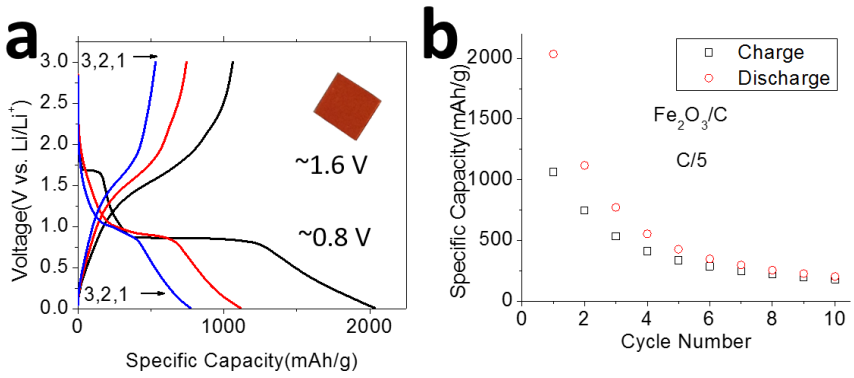

Fig. 5-3-S7. Electrochemical performance of olive-like α-Fe_2O_3/C deposited on current collector without any additives by CAP: (a) First 3 cycles of charge-discharge profiles, and (b) capacity vs. cycle number plots at current rate of C/5. Inset of (a) shows the optical image of red colored additive-free Fe_2O_3/C deposited on a copper disc current collector as a ready electrode.

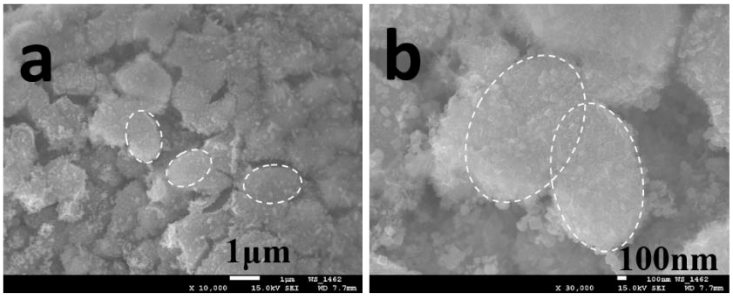

Fig. 5-3-S8. The morphology of the porous olive-like carbon decorated Fe_3O_4 based additive-free electrode after 120 cycles of electrochemical test was investigated by FESEM: (a) low-magnification overall view and (b) high-magnification view two typical olive-like nanoparticles. The olive-like shape can still be observed from the sample after the electrochemical test, indicating the relatively structural stability.

CHAPTER 6. CONCLUSION

Table 6-1 Comparison of reversible capacities of all iron oxides materials

Structure	Specific Capacity (mA h g^{-1})	Current	Cycles
Solid microparticle*	550	C/5	120
Microframe	700	C/5	220
Chevron beads	545 (514 mA h cm^{-3})	C/5	80
Solid beads	335 (345 mA h cm^{-3})	C/5	80
Hollow Cocoon	437	C/5	120
Solid Cocoon	100	C/5	120
Porous Fe_3O_4/C	800	C/10	235

Note: * This solid microparticle sample was prepared at 150°C.

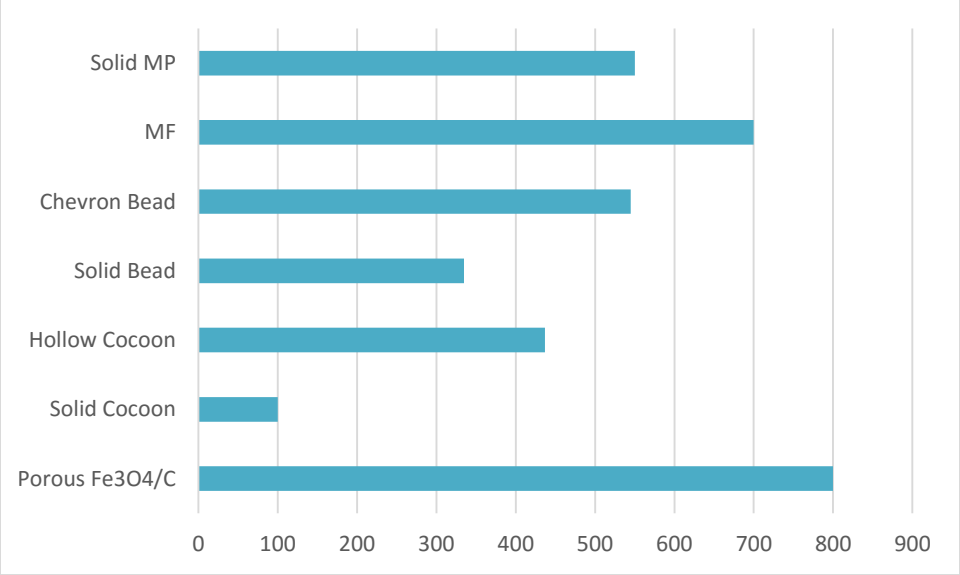

Fig. 6-1. Comparison of reversible capacities of all iron oxides materials

In summary, we have developed a facile template-free one-pot solvothermal method to prepare α-Fe_2O_3 active materials with controlled size and morphology in alcohol-water system. Iron oxides anode materials with different sizes and shapes have been synthesized, including microparticles

such as single crystalline Fe_2O_3 solid microparticle, and hollow single crystalline Fe_2O_3 microframes; and nanoparticle ensembles such as Fe_2O_3 hollow nanococoons (and solid nanococoons as comparison), Fe_2O_3 chevron beads (and solid beads as comparison) and porous olive-like Fe_3O_4/C composite. The performances of as-obtained iron oxides as anode materials was summarized in Table 6-1 and Figure 6-1. From the table we can conclude that: (1) create void space inside the structure can effectively improve the reversible capacity (like void@frames as compared to solid microparticles, chevron beads as compared to solid beads, hollow cocoons as compared to solid cocoons); (2) single-crystalline particle may facilitate the Li^+ and have improved performance as there is no significant grain boundary or defects to hinder the Li^+ to across[208] (by comparing single-crystalline solid microparticles and single-crystalline void@frames to those nanoparticle-ensembles); (3) the conductivity of as-obtained electrode and the electrode preparation technic also determines the performance of the active materials or electrode as the Fe_3O_4/C composite and the additive-free electrode of Fe_3O_4/C prepared via centrifugation-assisted preparation (CAP) exhibited superior specific capacity and cycling performance. It is obvious that engineering the size, shape, structure of active materials is of great importance to optimize the performance of as-prepared materials. Both nano- or micro-sized structure are potentially the ideal size for active materials and can exhibit excellent cyclability, reversible specific capacity or volumetric capacity. The control of the shape of the structure, such as create tunnel of void space inside the structure can effectively facilitate the diffusion of ion and electrolyte to improve the electrochemical performance. Also, the hieratical structures with secondary structure assembled by primary nanoparticles or active materials-carbon composites are proved to possess excellent performance. Besides the optimization of the structure of active materials, our effort to prepare additive-free electrode via new method without sacrifice of the battery performance is achieved,

and superior battery performance was obtained while the use of polymer binder, conductivity enhancer, and toxic NMP solvent was eliminated.

CHAPTER 7. FUTURE OUTLOOK

The improvement of performance of Li-ion batteries can be achieved via various routes. Improving the performance of anode materials by preparing nano-/micro- structures is only one of the effective routes. My research so far mainly focused on iron oxide materials in nano- or micro-structures, but there are still other routes that can be exploited to improve the energy storage. Therefore, the future research activities are suggested based on my research and briefly discussed here.

7.1 Iron oxides/ carbon composites

My research that has been done so far on iron oxides materials focuses more on fundamental morphology-property relationship. Pure iron oxides materials were used as active materials in most of the published work in order to prevent the difference caused by materials other than iron oxides. However, due to the limitation of intrinsic property of iron oxides (such as volume variation during recharging and low electric conductivity), the iron oxides materials may not reach its theoretical performance or capacity. To optimize the electrochemical performance, combining high-capacity iron oxides materials with soft, highly conductive carbon materials would be an effective route. Carbon nanoparticle decoration, carbon protective and buffer coating layer, metal oxides nanoparticle loaded on carbon, or metal oxides & graphene composite have all been proved to be effective method to further improve the performance of metal oxides materials. Thus, if the goal is to optimize the battery performance, further work could be carried out by combining the as-obtained iron oxides materials with carbon.

7.2 Other high capacity anode materials

Iron oxides have been selected in our work, as promising carbon-alternative anode materials for LIBs because of its high specific capacity, low cost, abundance, high stability, environmental

benignity and ease of fabrication. Iron oxides store Li^+ via conversion type reaction, meanwhile, other materials which store Li^+ via alloy-type reaction also exhibit promising specific capacity or energy density, such as Si and Sn. For example, Amprius and Nexeon have used silicon (carbon is still the dominant composition) as anode for high energy Li-ion batteries and Sony's Nexelion Li-ion battery anode powder consists of alloy of tin and cobalt (carbon 36 wt%, tin 27wt%, cobalt 16wt%). Similar to conversion-type materials, the huge volume variation during charging-discharging process and the resulting poor cyclability have to be addressed. Thus, the shape, size, hierarchical structure or active materials-carbon composites also have to be carefully designed in order to improve the performance of those materials. I have done some preliminary work on Si[209] and Co-Sn alloy[210] anode materials.

7.3 Cathode materials and other battery system

Besides anode materials, battery performance can also be improved from cathode (positive electrode). For iron based materials, convention type iron oxyfluoride (FeOF) was a promising high capacity cathode materials (885 mA h g^{-1} theoretically) for both Li-ion and Na-ion batteries.

Due to limiting Li sources and the concern of cost of Li sources, efforts have also been made to develop other electrochemical battery system other than lithium ion batteries. Sodium ion batteries are promising candidates owing to the abundance and low cost of sodium. However, it is more difficult to find appropriate electrode materials for SIBs than LIBs, due to the larger size of the Na^+. Our preliminary work has demonstrated the high capacity of FeOF as cathode materials for Na-ion batteries.[211]

REFERENCES

(1) C. Liu; F. Li; L.-P. Ma; H.-M. Cheng *Adv. Mater.* **2010**, *22*, E28.

(2) T. B. Reddy *Linden's Handbook of Batteries*; McGraw-Hill, 2011; Vol. 4.

(3) J.-M. Tarascon; M. Armand *Nature* **2001**, *414*, 359.

(4) B. Dunn; H. Kamath; J.-M. Tarascon *Science* **2011**, *334*, 928.

(5) F. Liu; S. Song; D. Xue; H. Zhang *Nanoscale Res. Lett.* **2012**, *7*, 149.

(6) L. Ji; Z. Lin; M. Alcoutlabi; X. Zhang *Energy Environ. Sci.* **2011**, *4*, 2682.

(7) J. Wolfenstine; J. L. Allen; J. Read; D. Foster *Chemistry and Structure of Sony's Nexelion Li-ion Electrode Materials*, DTIC Document, 2006.

(8) Y. Miyaki; Google Patents: 2006.

(9) Y. Miyaki; Google Patents: 2005.

(10) L. M. Bronstein; X. Huang; J. Retrum; A. Schmucker; M. Pink; B. D. Stein; B. Dragnea *Chem. Mater.* **2007**, *19*, 3624.

(11) Y. Xiong; Z. Li; X. Li; B. Hu; Y. Xie *Inorg. Chem.* **2004**, *43*, 6540.

(12) X. Wen; S. Wang; Y. Ding; Z. L. Wang; S. Yang *J. Phys. Chem. B* **2005**, *109*, 215.

(13) Y. Ling; G. Wang; D. A. Wheeler; J. Z. Zhang; Y. Li *Nano Lett.* **2011**, *11*, 2119.

(14) L. Yuan; Q. Jiang; J. Wang; G. Zhou *J. Mater. Res.* **2012**, *27*, 1014.

(15) W. Zhou; K. Tang; S. Zeng; Y. Qi *Nanotechnology* **2008**, *19*, 065602.

(16) A. K. Ganguli; T. Ahmad *J. Nanosci. Nanotechnol.* **2007**, *7*, 2029.

(17) W. Cho; S. Park; M. Oh *Chem. Commun.* **2011**, *47*, 4138.

(18) J. Chen; L. Xu; W. Li; X. Gou *Adv. Mater.* **2005**, *17*, 582.

(19) N. Kang; J. H. Park; J. Choi; J. Jin; J. Chun; I. G. Jung; J. Jeong; J.-G. Park; S. M. Lee; H. J. Kim; S. U. Son *Angew. Chem. Int. Ed.* **2012**, *51*, 6626.

(20) M. Reddy; T. Yu; C. H. Sow; Z. X. Shen; C. T. Lim; G. Subba Rao; B. Chowdari *Adv. Funct. Mater.* **2007**, *17*, 2792.

(21) J. S. Chen; T. Zhu; X. H. Yang; H. G. Yang; X. W. Lou *J. Am. Chem. Soc.* **2010**, *132*, 13162.

(22) X. Hu; J. C. Yu; J. Gong; Q. Li; G. Li *Adv. Mater.* **2007**, *19*, 2324.

(23) S. Xiong; J. Xu; D. Chen; R. Wang; X. Hu; G. Shen; Z. L. Wang *CrystEngComm* **2011**, *13*, 7114.

(24) X. Liang; X. Wang; J. Zhuang; Y. Chen; D. Wang; Y. Li *Adv. Funct. Mater.* **2006**, *16*, 1805.

(25) H. Cao; G. Wang; J. H. Warner; A. A. Watt *Applied Physics Letters* **2008**, *92*, 013110.

(26) S. Zeng; K. Tang; T. Li; Z. Liang; D. Wang; Y. Wang; W. Zhou *J. Phys. Chem. C* **2007**, *111*, 10217.

(27) X. H. Jia; H. J. Song *J. Nanopart. Res.* **2012**, *14*, 1.

(28) S.-W. Cao; Y.-J. Zhu *J. Phys. Chem. C* **2008**, *112*, 6253.

(29) B. Wang; J. S. Chen; H. B. Wu; Z. Wang; X. W. Lou *J. Am. Chem. Soc.* **2011**, *133*, 17146.

(30) X. Xu; R. Cao; S. Jeong; J. Cho *Nano Letters* **2012**, *12*, 4988.

(31) D. Du; M. Cao *J. Phys. Chem. C* **2008**, *112*, 10754.

(32) S. Zeng; K. Tang; T. Li; Z. Liang; D. Wang; Y. Wang; Y. Qi; W. Zhou *J. Phys. Chem. C* **2008**, *112*, 4836.

(33) Z. Wu; K. Yu; S. Zhang; Y. Xie *J. Phys. Chem. C* **2008**, *112*, 11307.

(34) H.-J. Kim; K.-I. Choi; A. Pan; I.-D. Kim; H.-R. Kim; K.-M. Kim; C. W. Na; G. Cao; J.-H. Lee *J. Mater. Chem.* **2011**, *21*, 6549.

(35) H.-J. Song; N. Li; X.-Q. Shen *Appl. Phys. A: Mater. Sci. Process.* **2011**, *102*, 559.

(36) C.-Y. Hu; Y.-J. Xu; S.-W. Duo; W.-K. Li; J.-H. Xiang; M.-S. Li; R.-F. Zhang *J. Chin. Chem. Soc.* **2010**, *57*, 1091.

(37) J. Liu; Y. Li; H. Fan; Z. Zhu; J. Jiang; R. Ding; Y. Hu; X. Huang *Chem. Mater.* **2009**, *22*, 212.

(38) Y. NuLi; P. Zhang; Z. Guo; H. Liu *J. Electrochem. Soc.* **2008**, *155*, A196.

(39) G. Sha; T. Wang; J. Xiao; C. Liang *Mater. Res. Bull.* **2004**, *39*, 1917.

(40) Z. G. An; J. J. Zhang; S. L. Pan; G. Z. Song *Powder Technol.* **2012**, *217*, 274.

(41) W. Zhu; X. Cui; L. Wang; T. Liu; Q. Zhang *Mater. Lett.* **2011**, *65*, 1003.

(42) C. Z. Wu; P. Yin; X. Zhu; C. Z. OuYang; Y. Xie *J. Phys. Chem. B* **2006**, *110*, 17806.

(43) J. Cai; S. Chen; M. Ji; J. Hu; Y. Ma; L. Qi *CrystEngComm* **2014**, *16*, 1553.

(44) T. Liu; Y. Ling; Y. Yang; L. Finn; E. Collazo; T. Zhai; Y. Tong; Y. Li *Nano Energy* **2015**, *12*, 169.

(45) J. Zhang; Y. Sun; Y. Yao; T. Huang; A. Yu *J. Power Sources* **2013**, *222*, 59.

(46) S. Xu; C. M. Hessel; H. Ren; R. Yu; Q. Jin; M. Yang; H. Zhao; D. Wang *Energy Environ. Sci.* **2014**, *7*, 632.

(47) X. Liu; H. Wang; C. Su; P. Zhang; J. Bai *J. Colloid Interface Sci.* **2010**, *351*, 427.

(48) T. Yang; Z. Huang; Y. Liu; M. Fang; X. Ouyang; M. Hu *Ceram. Int.* **2014**, *40*, 11975.

(49) S. Xuan; L. Hao; W. Jiang; L. Song; Y. Hu; Z. Chen; L. Fei; T. Li *Cryst. Growth Des.* **2007**, *7*, 430.

(50) T.-W. Sun; Y.-J. Zhu; C. Qi; G.-J. Ding; F. Chen; J. Wu *J. Colloid Interface Sci.* **2016**, *463*, 107.

(51) J.-S. Xu; Y.-J. Zhu *J. Colloid Interface Sci.* **2012**, *385*, 58.

(52) J.-S. Xu; Y.-J. Zhu *ACS Appl. Mater. Interfaces* **2012**, *4*, 4752.

(53) Y. Chen; K. Zhang; Y. Min; Y. Zhang; R. Zhang *Materials Chemistry and Physics* **2010**, *123*, 378.

(54) X. Liang; B. Xi; S. Xiong; Y. Zhu; F. Xue; Y. Qian *Mater. Res. Bull.* **2009**, *44*, 2233.

(55) L. S. Zhong; J. S. Hu; H. P. Liang; A. M. Cao; W. G. Song; L. J. Wan *Adv. Mater.* **2006**, *18*, 2426.

(56) Z. Wang; D. Luan; S. Madhavi; Y. Hu; X. W. Lou *Energy Environ. Sci.* **2012**, *5*, 5252.

(57) W. M. Zhang; X. L. Wu; J. S. Hu; Y. G. Guo; L. J. Wan *Adv. Funct. Mater.* **2008**, *18*, 3941.

(58) Z. Yang; J. Shen; L. A. Archer *J. Mater. Chem.* **2011**, *21*, 11092.

(59) L. Wang; J. Liang; Y. Zhu; T. Mei; X. Zhang; Q. Yang; Y. Qian *Nanoscale* **2013**, *5*, 3627.

(60) Y.-G. Zhu; J. Xie; G. Cao; T. Zhu; X. B. Zhao *RSC Advances* **2013**.

(61) S. Jin; H. Deng; D. Long; X. Liu; L. Zhan; X. Liang; W. Qiao; L. Ling *J. Power Sources* **2011**, *196*, 3887.

(62) L. Zhang; H. B. Wu; X. W. Lou *Adv. Energy Mater.* **2014**, *4*, 1300958.

(63) H. G. Yang; C. H. Sun; S. Z. Qiao; J. Zou; G. Liu; S. C. Smith; H. M. Cheng; G. Q. Lu *Nature* **2008**, *453*, 638.

(64) X. Han; M. Jin; S. Xie; Q. Kuang; Z. Jiang; Y. Jiang; Z. Xie; L. Zheng *Angew. Chem.* **2009**, *121*, 9344.

(65) X. Zhou; Q. Xu; W. Lei; T. Zhang; X. Qi; G. Liu; K. Deng; J. Yu *Small* **2013**, n/a.

(66) L. Liu; H. Guo; M. Zhou; Q. Wei; Z. Yang; H. Shu; X. Yang; J. Tan; Z. Yan; X. Wang *J. Power Sources* **2013**, *238*, 501.

(67) J. Shi; G. Hu; R. Cong; H. Bu; N. Dai *New J. Chem.* **2013**, *37*, 1538.

(68) Y. Gao; M. Fan; Q. Fang; W. Han *New J. Chem.* **2013**, *37*, 670.

(69) H. Wang; X. Lang; J. Gao; W. Liu; D. Wu; Y. Wu; L. Guo; J. Li *Chem. Eur. J.* **2012**, *18*, 4620.

(70) H. Wang; L. He; L. Wang; P. Hu; L. Guo; X. Han; J. Li *Crystengcomm* **2012**, *14*, 8342.

(71) Z. Wang; D. Luan; S. Madhavi; C. Ming Li; X. Wen Lou *Chem. Commun.* **2011**, *47*, 8061.

(72) L. Zhang; H. B. Wu; R. Xu; X. W. Lou *CrystEngComm* **2013**, *15*, 9332.

(73) L. Zhou; H. Xu; H. Zhang; J. Yang; S. B. Hartono; K. Qian; J. Zou; C. Yu *Chem. Commun.* **2013**, *49*, 8695.

(74) L. Zhang; H. B. Wu; S. Madhavi; H. H. Hng; X. W. Lou *J. Am. Chem. Soc.* **2012**, *134*, 17388.

(75) M. Tadic; N. Citakovic; M. Panjan; Z. Stojanovic; D. Markovic; V. Spasojevic *J. Alloys Compd.* **2011**, *509*, 7639.

(76) H. Guo; A. S. Barnard *J. Colloid Interface Sci.* **2012**, *386*, 315.

(77) J. Lu; D. Chen; X. Jiao *J. Colloid Interface Sci.* **2006**, *303*, 437.

(78) J. S. Chen; T. Zhu; C. M. Li; X. W. Lou *Angew. Chem. Int. Ed.* **2011**, *50*, 650.

(79) M. Lin; H. R. Tan; J. P. Y. Tan; S. Bai *J. Phys. Chem. C* **2013**.

(80) Z. Liu; B. Lv; D. Wu; Y. Sun; Y. Xu *Particuology* **2013**.

(81) H. Xiao; Y. Xia; W. Zhang; H. Huang; Y. Gan; X. Tao *J. Mater. Chem. A* **2013**, *1*, 2307.

(82) X. Lai; J. E. Halpert; D. Wang *Energy Environ. Sci.* **2012**, *5*, 5604.

(83) X. Kang; D. Yang; P. a. Ma; Y. Dai; M. Shang; D. Geng; Z. Cheng; J. Lin *Langmuir* **2013**, *29*, 1286.

(84) X. Zhou; Y. Gan; J. Du; D. Tian; R. Zhang; C. Yang; Z. Dai *J. Power Sources* **2013**, *232*, 310.

(85) S. Wang; M. Zhang; W. Zhang *ACS Catalysis* **2011**, *1*, 207.

(86) J. H. Pan; X. Zhang; A. J. Du; D. D. Sun; J. O. Leckie *J. Am. Chem. Soc.* **2008**, *130*, 11256.

(87) B. Wang; H. Wu; L. Yu; R. Xu; T.-T. Lim; X. W. Lou *Adv. Mater.* **2012**, *24*, 1111.

(88) L. Zhang; H. B. Wu; B. Liu; X. W. Lou *Energy Environ. Sci.* **2014**, *7*, 1013.

(89) S. K. Addu; J. Zhu; K. Y. S. Ng; D. Deng *Chem. Mater.* **2014**, *26*, 4472.

(90) J. H. Pan; X. Z. Wang; Q. Huang; C. Shen; Z. Y. Koh; Q. Wang; A. Engel; D. W. Bahnemann *Adv. Funct. Mater.* **2014**, *24*, 95.

(91) B. Wang; H. B. Wu; L. Zhang; X. W. Lou *Angew. Chem. Int. Ed.* **2013**, *52*, 4165.

(92) Z. Wang; L. Zhou; X. W. Lou *Adv. Mater.* **2012**, *24*, 1903.

(93) K.-Y. Niu; J. Park; H. Zheng; A. P. Alivisatos *Nano Letters* **2013**, *13*, 5715.

(94) W. Wang; M. Dahl; Y. Yin *Chem. Mater.* **2012**, *25*, 1179.

(95) X. Xia; Y. Wang; A. Ruditskiy; Y. Xia *Adv. Mater.* **2013**, *25*, 6313.

(96) J. Wang; N. Yang; H. Tang; Z. Dong; Q. Jin; M. Yang; D. Kisailus; H. Zhao; Z. Tang; D. Wang *Angew. Chem.* **2013**, *125*, 6545.

(97) C.-H. Kuo; M. H. Huang *J. Am. Chem. Soc.* **2008**, *130*, 12815.

(98) X. Hong; D. Wang; S. Cai; H. Rong; Y. Li *J. Am. Chem. Soc.* **2012**, *134*, 18165.

(99) C. Chen; Y. Kang; Z. Huo; Z. Zhu; W. Huang; H. L. Xin; J. D. Snyder; D. Li; J. A. Herron; M. Mavrikakis; M. Chi; K. L. More; Y. Li; N. M. Markovic; G. A. Somorjai; P. Yang; V. R. Stamenkovic *Science* **2014**, *343*, 1339.

(100) A. Magasinski; P. Dixon; B. Hertzberg; A. Kvit; J. Ayala; G. Yushin *Nat. Mater.* **2010**, *9*, 353.

(101) Y. H. Kwon; S.-W. Woo; H.-R. Jung; H. K. Yu; K. Kim; B. H. Oh; S. Ahn; S.-Y. Lee; S.-W. Song; J. Cho; H.-C. Shin; J. Y. Kim *Adv. Mater.* **2012**, *24*, 5192.

(102) J. Hu; M. Chen; X. Fang; L. Wu *Chem. Soc. Rev.* **2011**, *40*, 5472.

(103) D. Kim; J. Park; K. An; N.-K. Yang; J.-G. Park; T. Hyeon *J. Am. Chem. Soc.* **2007**, *129*, 5812.

(104) M. A. Mahmoud; W. Qian; M. A. El-Sayed *Nano Letters* **2011**, *11*, 3285.

(105) Y. Sui; W. Fu; Y. Zeng; H. Yang; Y. Zhang; H. Chen; Y. Li; M. Li; G. Zou *Angew. Chem. Int. Ed.* **2010**, *49*, 4282.

(106) H.-J. Song; X.-H. Jia; H. Qi; X.-F. Yang; H. Tang; C.-Y. Min *J. Mater. Chem.* **2012**, *22*, 3508.

(107) H. Jun; B. Im; J. Y. Kim; Y.-O. Im; J.-W. Jang; E. S. Kim; J. Y. Kim; H. J. Kang; S. J. Hong; J. S. Lee *Energy Environ. Sci.* **2012**, *5*, 6375.

(108) P. Tartaj; M. P. Morales; T. Gonzalez-Carreño; S. Veintemillas-Verdaguer; C. J. Serna *Adv. Mater.* **2011**, *23*, 5243.

(109) X. Zhu; Y. Zhu; S. Murali; M. D. Stoller; R. S. Ruoff *ACS Nano* **2011**, *5*, 3333.

(110) Z.-g. Wu; Y.-j. Zhong; J. Liu; J.-h. Wu; X.-d. Guo; B.-h. Zhong; Z.-y. Zhang *J. Mater. Chem. A* **2015**, *3*, 10092.

(111) M. Valvo; F. Lindgren; U. Lafont; F. Björefors; K. Edström *J. Power Sources* **2014**, *245*, 967.

(112) B. Wang; J. S. Chen; X. W. Lou *J. Mater. Chem.* **2012**, *22*, 9466.

(113) J. Zhu; Z. Yin; D. Yang; T. Sun; H. Yu; H. E. Hoster; H. H. Hng; H. Zhang; Q. Yan *Energy Environ. Sci.* **2013**, *6*, 987.

(114) H. Cheng; B. Huang; Y. Liu; Z. Wang; X. Qin; X. Zhang; Y. Dai *Chem. Commun.* **2012**, *48*, 9729.

(115) J. Zhu; K. Y. S. Ng; D. Deng *ACS Appl. Mater. Interfaces* **2014**, *6*, 2996.

(116) J. Yu; X. Yu; B. Huang; X. Zhang; Y. Dai *Cryst. Growth Des.* **2009**, *9*, 1474.

(117) L. Wang; X. Lu; C. Han; R. Lu; S. Yang; X. Song *CrystEngComm* **2014**, *16*, 10618.

(118) J. Zhu; K. Y. S. Ng; D. Deng *Nanoscale* **2015**, DOI: 10.1039/c5nr03840e.

(119) J. Zhu; K. Y. S. Ng; D. Deng *J. Mater. Chem. A* **2014**, *2*, 16008.

(120) K. Charette; J. Zhu; S. O. Salley; K. Y. S. Ng; D. Deng *RSC Adv.* **2014**, *4*, 2557.

(121) X. Chen; J. P. Cheng; Q. L. Shou; F. Liu; X. B. Zhang *CrystEngComm* **2012**, *14*, 1271.

(122) J. B. Joo; Q. Zhang; M. Dahl; I. Lee; J. Goebl; F. Zaera; Y. Yin *Energy Environ. Sci.* **2012**, *5*, 6321.

(123) F. N. Sayed; V. Polshettiwar *Sci. Rep.* **2015**, *5*.

(124) T. Shiomi; T. Tsunoda; A. Kawai; F. Mizukami; K. Sakaguchi *Chem. Commun.* **2007**, 4404.

(125) L. Li; Z. Wu; S. Yuan; X.-B. Zhang *Energy Environ. Sci.* **2014**, *7*, 2101.

(126) D.-l. Ma; Z.-y. Cao; H.-g. Wang; X.-l. Huang; L.-m. Wang; X.-b. Zhang *Energy Environ. Sci.* **2012**, *5*, 8538.

(127) S. Yuan; X.-l. Huang; D.-l. Ma; H.-g. Wang; F.-z. Meng; X.-b. Zhang *Adv. Mater.* **2014**, *26*, 2273.

(128) Y. Li; C. Zhu; T. Lu; Z. Guo; D. Zhang; J. Ma; S. Zhu *Carbon* **2013**, *52*, 565.

(129) D. Deng; J. Y. Lee *ACS Appl. Mater. Interfaces* **2014**, *6*, 1173.

(130) P. Poizot; S. Laruelle; S. Grugeon; L. Dupont; J. M. Tarascon *Nature* **2000**, *407*, 496.

(131) X. Wang; X. Li; X. Sun; F. Li; Q. Liu; Q. Wang; D. He *J. Mater. Chem.* **2011**, *21*, 3571.

(132) D. Larcher; C. Masquelier; D. Bonnin; Y. Chabre; V. Masson; J.-B. Leriche; J.-M. Tarascon *J. Electrochem. Soc.* **2003**, *150*, A133.

(133) S. Komaba; T. Mikumo; N. Yabuuchi; A. Ogata; H. Yoshida; Y. Yamada *J. Electrochem. Soc.* **2010**, *157*, A60.

(134) X. Liu; T. Chen; H. Chu; L. Niu; Z. Sun; L. Pan; C. Q. Sun *Electrochim. Acta* **2015**, *166*, 12.

(135) H. Kang; Y. Liu; K. Cao; Y. Zhao; L. Jiao; Y. Wang; H. Yuan *J. Mater. Chem. A* **2015**.

(136) Y. Fu; Q. Wei; X. Wang; H. Shu; X. Yang; S. Sun *J. Mater. Chem. A* **2015**, *3*, 13807.

(137) Z. Jian; B. Zhao; P. Liu; F. Li; M. Zheng; M. Chen; Y. Shi; H. Zhou *Chem. Commun.* **2014**, *50*, 1215.

(138) R. Alcántara; J. M. Jiménez-Mateos; P. Lavela; J. L. Tirado *Electrochem. Commun.* **2001**, *3*, 639.

(139) S. J. Hollister *Nat. Mater.* **2005**, *4*, 518.

(140) Y. Ning; Y. Yang; C. Wang; T. Ngai; Z. Tong *Chem. Commun.* **2013**, *49*, 8761.

(141) P. Poizot; S. Laruelle; S. Grugeon; L. Dupont; J. Tarascon *Nature* **2000**, *407*, 496.

(142) A. S. Aricò; P. Bruce; B. Scrosati; J.-M. Tarascon; W. Van Schalkwijk *Nat. Mater.* **2005**, *4*, 366.

(143) P. G. Bruce; B. Scrosati; J. M. Tarascon *Angew. Chem. Int. Ed.* **2008**, *47*, 2930.

(144) X. W. D. Lou; L. A. Archer; Z. Yang *Adv. Mater.* **2008**, *20*, 3987.

(145) C. M. Ban; Z. C. Wu; D. T. Gillaspie; L. Chen; Y. F. Yan; J. L. Blackburn; A. C. Dillon *Adv. Mater.* **2010**, *22*, E145.

(146) J. Chen; L. N. Xu; W. Y. Li; X. L. Gou *Adv. Mater.* **2005**, *17*, 582.

(147) X. L. Hu; J. C. Yu; J. M. Gong; Q. Li; G. S. Li *Adv. Mater.* **2007**, *19*, 2324.

(148) M. V. Reddy; T. Yu; C. H. Sow; Z. X. Shen; C. T. Lim; G. V. S. Rao; B. V. R. Chowdari *Adv. Funct. Mater.* **2007**, *17*, 2792.

(149) X. J. Zhu; Y. W. Zhu; S. Murali; M. D. Stollers; R. S. Ruoff *Acs Nano* **2011**, *5*, 3333.

(150) X. Xu; R. Cao; S. Jeong; J. Cho *Nano Lett.* **2012**.

(151) W. A. Ang; N. Gupta; R. Prasanth; M. Srinivasan *ACS Appl. Mater. Interfaces* **2012**.

(152) Z. An; J. Zhang; S. Pan; G. Song *Powder Technol.* **2012**, *217*, 274.

(153) H. Katsuki; S. Komarneni *J. Am. Ceram. Soc.* **2003**, *86*, 183.

(154) D. Deng; S. T. Martin; S. Ramanathan *J. Mater. Res.* **2011**, *26*, 1545.

(155) D. Larcher; D. Bonnin; R. Cortes; I. Rivals; L. Personnaz; J.-M. Tarascon *J. Electrochem. Soc.* **2003**, *150*, A1643.

(156) N. Liu; Z. Lu; J. Zhao; M. T. McDowell; H.-W. Lee; W. Zhao; Y. Cui *Nat. Nano.* **2014**, *9*, 187.

(157) M. Wang; Y. Yang; Y. Zhang *Nanoscale* **2011**, *3*, 4434.

(158) H. Ren; R. Yu; J. Wang; Q. Jin; M. Yang; D. Mao; D. Kisailus; H. Zhao; D. Wang *Nano Lett.* **2014**, *14*, 6679.

(159) G.-N. Zhu; H.-J. Liu; J.-H. Zhuang; C.-X. Wang; Y.-G. Wang; Y.-Y. Xia *Energy Environ. Sci.* **2011**, *4*, 4016.

(160) S.-M. Oh; J.-Y. Hwang; C. S. Yoon; J. Lu; K. Amine; I. Belharouak; Y.-K. Sun *ACS Appl. Mater. Interfaces* **2014**, *6*, 11295.

(161) X. Xu; S. Chen; M. Shui; L. Xu; W. Zheng; J. Shu; L. Cheng; L. Feng; Y. Ren *Ionics* **2014**, *20*, 1285.

(162) Y. Lin; F. Zhang; D. Pan *J. Mater. Chem.* **2012**, *22*, 22619.

(163) F. Chen; J. Zai; M. Xu; X. Qian *J. Mater. Chem. A* **2013**, *1*, 4316.

(164) Z. Li; Y. Zhou; J. Song; T. Yu; J. Liu; Z. Zou *J. Mater. Chem. A* **2013**, *1*, 524.

(165) L. Wang; Z. Lou; T. Fei; T. Zhang *J. Mater. Chem.* **2011**, *21*, 19331.

(166) X. Liu; X. Jin; P. X. Ma *Nat. Mater.* **2011**, *10*, 398.

(167) J. Du; J. Qi; D. Wang; Z. Tang *Energy Environ. Sci.* **2012**, *5*, 6914.

(168) Z. Dong; X. Lai; J. E. Halpert; N. Yang; L. Yi; J. Zhai; D. Wang; Z. Tang; L. Jiang *Adv. Mater.* **2012**, *24*, 1046.

(169) Z. Dong; H. Ren; C. M. Hessel; J. Wang; R. Yu; Q. Jin; M. Yang; Z. Hu; Y. Chen; Z. Tang; H. Zhao; D. Wang *Adv. Mater.* **2014**, *26*, 905.

(170) J. Wang; H. Tang; H. Ren; R. Yu; J. Qi; D. Mao; H. Zhao; D. Wang *Advanced Science* **2014**, *1*, DOI: 10.1002/advs.201400011.

(171) P. Xu; R. Yu; H. Ren; L. Zong; J. Chen; X. Xing *Chemical Science* **2014**, *5*, 4221.

(172) Y. Wang; X. Su; S. Lu *J. Mater. Chem.* **2012**, *22*, 1969.

(173) L. Cao; D. Chen; R. A. Caruso *Angew. Chem. Int. Ed.* **2013**, *52*, 10986.

(174) J. Zhao; Y. Zou; X. Zou; T. Bai; Y. Liu; R. Gao; D. Wang; G.-D. Li *Nanoscale* **2014**, *6*, 7255.

(175) L. Zhang; H. B. Wu; X. W. Lou *J. Am. Chem. Soc.* **2013**, *135*, 10664.

(176) H. G. Yang; H. C. Zeng *J. Phys. Chem. B* **2004**, *108*, 3492.

(177) G.-Q. Xin; H.-P. Ding; Y.-G. Yang; S.-L. Shen; Z.-C. Xiong; X. Chen; J. Hao; H.-G. Liu *Cryst. Growth Des.* **2009**, *9*, 2008.

(178) X. Hu; J. C. Yu; J. Gong; Q. Li; G. Li *Adv. Mater.* **2007**, *19*, 2324.

(179) B. Tao; Q. Zhang; Z. Liu; B. Geng *Materials Chemistry and Physics* **2012**, *136*, 604.

(180) L. Zhou; H. Xu; H. Zhang; J. Yang; S. B. Hartono; K. Qian; J. Zou; C. Yu *Chem. Commun.* **2013**, *49*, 8695.

(181) Y. NuLi; R. Zeng; P. Zhang; Z. Guo; H. Liu *J. Power Sources* **2008**, *184*, 456.

(182) C. T. Cherian; J. Sundaramurthy; M. Kalaivani; P. Ragupathy; P. S. Kumar; V. Thavasi; M. V. Reddy; C. H. Sow; S. G. Mhaisalkar; S. Ramakrishna; B. V. R. Chowdari *J. Mater. Chem.* **2012**, *22*, 12198.

(183) M. V. Reddy; T. Yu; C. H. Sow; Z. X. Shen; C. T. Lim; G. V. Subba Rao; B. V. R. Chowdari *Adv. Funct. Mater.* **2007**, *17*, 2792.

(184) M. Armand; J.-M. Tarascon *Nature* **2008**, *451*, 652.

(185) A. S. Arico; P. Bruce; B. Scrosati; J. M. Tarascon; W. Van Schalkwijk *Nat. Mater.* **2005**, *4*, 366.

(186) F. Cheng; J. Liang; Z. Tao; J. Chen *Adv. Mater.* **2011**, *23*, 1695.

(187) N. Tsuda *Electronic conduction in oxides*; Springer, 2000; Vol. 94.

(188) S. M. Yuan; J. X. Li; L. T. Yang; L. W. Su; L. Liu; Z. Zhou *ACS Appl. Mater. Interfaces* **2011**, *3*, 705.

(189) Y. Chen; H. Xia; L. Lu; J. Xue *J. Mater. Chem.* **2012**, *22*, 5006.

(190) Q. Q. Xiong; J. P. Tu; Y. Lu; J. Chen; Y. X. Yu; Y. Q. Qiao; X. L. Wang; C. D. Gu *J. Phys. Chem. C* **2012**, *116*, 6495.

(191) P. L. Taberna; S. Mitra; P. Poizot; P. Simon; J. M. Tarascon *Nat Mater* **2006**, *5*, 567.

(192) T. Muraliganth; A. Vadivel Murugan; A. Manthiram *Chem. Commun.* **2009**, 7360.

(193) J.-K. Hwang; H.-S. Lim; Y.-K. Sun; K.-D. Suh *J. Power Sources* **2013**, *244*, 538.

(194) W. Wei; S. Yang; H. Zhou; I. Lieberwirth; X. Feng; K. Müllen *Adv. Mater.* **2013**, n/a.

(195) T. Yoon; C. Chae; Y.-K. Sun; X. Zhao; H. H. Kung; J. K. Lee *J. Mater. Chem.* **2011**, *21*, 17325.

(196) Y. Piao; H. S. Kim; Y.-E. Sung; T. Hyeon *Chem. Commun.* **2010**, *46*, 118.

(197) M. Zhang; D. Lei; X. Yin; L. Chen; Q. Li; Y. Wang; T. Wang *J. Mater. Chem.* **2010**, *20*, 5538.

(198) L. Wang; J. Liang; Y. Zhu; T. Mei; X. Zhang; Q. Yang; Y. Qian *Nanoscale* **2013**, *5*, 3627.

(199) C. He; S. Wu; N. Zhao; C. Shi; E. Liu; J. Li *ACS Nano* **2013**, *7*, 4459.

(200) G. Gao; L. Yu; H. B. Wu; X. W. Lou *Small* **2014**, *10*, 1741.

(201) J. S. Chen; Y. Zhang; X. W. Lou *ACS Appl. Mater. Interfaces* **2011**, *3*, 3276.

(202) D. Deng; J. Y. Lee *Chem. Mater.* **2008**, *20*, 1841.

(203) T. Zhu; J. S. Chen; X. W. Lou *J. Phys. Chem. C* **2011**, *115*, 9814.

(204) K. C. Chin; G. L. Chong; C. K. Poh; L. H. Van; C. H. Sow; J. Lin; A. T. S. Wee *J. Phys. Chem. C* **2007**, *111*, 9136.

(205) Z. Xiao; Y. Xia; Z. Ren; Z. Liu; G. Xu; C. Chao; X. Li; G. Shen; G. Han *J. Mater. Chem.* **2012**, *22*, 20566.

(206) S. H. Lee; S.-H. Yu; J. E. Lee; A. Jin; D. J. Lee; N. Lee; H. Jo; K. Shin; T.-Y. Ahn; Y.-W. Kim; H. Choe; Y.-E. Sung; T. Hyeon *Nano Letters* **2013**, *13*, 4249.

(207) L. Qie; W.-M. Chen; Z.-H. Wang; Q.-G. Shao; X. Li; L.-X. Yuan; X.-L. Hu; W.-X. Zhang; Y.-H. Huang *Adv. Mater.* **2012**, *24*, 2047.

(208) S. Yuan; Y.-B. Liu; D. Xu; D.-L. Ma; S. Wang; X.-H. Yang; Z.-Y. Cao; X.-B. Zhang *Advanced Science* **2015**, *2*, n/a.

(209) J. Zhu; D. Deng *RSC Adv.* **2015**, *5*, 67315.

(210) J. Zhu; D. Deng *J. Phys. Chem. C* **2015**, *119*, 21323.

(211) J. Zhu; D. Deng *Angew. Chem.* **2015**, *127*, 3122.

ABSTRACT

NOVEL DESIGN AND SYNTHESIS OF STRUCTURED IRON OXIDES FOR BATTERY APPLICATIONS

by

JIAN ZHU

December 2016

Advisor: Dr. Da Deng

Major: Chemical Engineering

Degree: Doctor of Philosophy

Lithium-ion batteries (LIBs) are currently the dominant powder source for personal computers and portable electronics. LIBs also play important roles in larger-scale applications, including electric drive vehicles (EVs, HEVs) and grid-energy storage. To meet the increasing demand for energy storage, it is very urgent and crucial to develop next-generation LIBs using alternative electrode materials. For example, carbon is still exclusively used as anode materials in current LIBs. However, the theoretical capacity of graphite (372 mA h g^{-1} based on LiC_6) has almost been achieved, and it becomes one of the bottlenecks to further increase the energy density of LIBs based on carbon. Therefore, there is an urgent need to develop carbon-alternative materials with higher capacity to meet the increasing demand for energy storage. Iron oxides, with a theoretical capacity of 1007 mA h g^{-1}, have been attracting much attention as a promising candidate to replace carbon. However, poor capacity retention and poor conductivity are the main issues. One strategy is to design and tailor structured iron oxides to address those issues. In addition, it is always practically interesting and intellectually challenging to develop facile methods to prepare iron oxides with desired structures. In our work, iron oxides with various sizes and structures have been designed and synthesized. The electrochemical performances of the as-synthesized iron oxides for

LIBs have been thoroughly evaluated. The fundamentals of structure-property relationships have been revealed. The impressive electrochemical performances achieved have demonstrated the promising application of those structured iron oxides for next-generation LIBs.

AUTOBIOGRAPHICAL STATEMENT

I was born in Hunan, China in 1988. I lived in Xiangtan, Hunan from birth to 2007, and lived in Changchun, Jilin from 2007 to 2011. I received my B.S. degree in Chemistry from Jinlin University, Changchun, Jinlin, China, in 2011. In August 2011, I enrolled in the Chemical Engineering (ChE) Graduate Program at Wayne State University. As a Ph.D candidate, I joined Dr. Deng's research group in 2012. My research mainly focused on novel nano-/ micro-structured materials for energy storage. I have published more than 10 peer-reviewed journal papers.

List Peer-Reviewed Journal Publications:

1. **J. Zhu**, D. Deng*. *RSC Advances*, **2016,** 6 (48), 42223-42228
2. **J. Zhu**, D. Deng*. *Chemical Engineering Science*, **2016,** DOI:10.1016/j.ces.2016.04.047
3. **J. Zhu**, D. Deng*. *Journal of Materials Chemistry A*, **2016**, 4 (12), 4425-4432.
4. **J. Zhu**, D. Deng*. *Angewandte Chemie*, **2015**, 127, 3122-3126.
5. **J. Zhu**, D. Deng*. *Advanced Functional Materials*, **2015**, 25 (39), 6250-6256.
6. **J. Zhu**, K. Y. S. Ng, D. Deng*. *Nanoscale*, **2015**, 7(34), 14368-14377.
7. **J. Zhu**, D. Deng*. *The Journal of Physical Chemistry C*, **2015**, 119 (37), 21323-21328.
8. **J. Zhu**, D. Deng*. *RSC Advances*, **2015**, 5 (82), 67315-67322.
9. S. K. Addu, **J. Zhu**, K. Y. S. Ng, D. Deng*. *Chemistry of Materials*, **2014**, 26 (15), 4472-4485. (S.A. Addu and J. Zhu contributed equally)
10. **J. Zhu**, K. Y. S. Ng, D. Deng*. *Journal of Materials Chemistry A*, **2014**, 2 (38), 16008-16014.
11. **J. Zhu**, K. Y. S. Ng, D. Deng*. *ACS Applied Materials & Interfaces*, **2014**, 6 (4), 2996-3001.
12. **J. Zhu**, K. Y. S. Ng, D. Deng*. *Crystal Growth & Design*, **2014**, 14 (6), 2811-2817.
13. K. Charette, **J. Zhu**, S. O. Salley, K. Y. S. Ng, D. Deng*. *RSC Advances*, **2014,** *4* (5), 2557-2562.